Protein delivery using mesoporous ceramic/polymer hybrid

Ng, Suxiu

2011

PROTEIN DELIVERY USING MESOPOROUS CERAMIC/ POLYMER HYBRID

NG SUXIU

SCHOOL OF MATERIALS SCIENCE AND ENGINEERING

2011

PROTEIN DELIVERY USING MESOPOROUS CERAMIC/ POLYMER HYBRID

NG SUXIU

School of Materials Science and Engineering

A thesis submitted to the Nanyang Technological University in partial fulfillment of the requirement for the degree of

Doctor of Philosophy

2011

ACKNOWLEDGEMENTS

ABSTRACT

Mesostructured materials of high specific surface area and pore volume were hypothesized to have the ability to encapsulate higher amount of proteins in the delivery systems. Hence, high surface area of mesostructured calcium phosphates (MCP) and mesoporous bioactive glasses (MBG) had been successfully synthesized for the protein adsorption study. The adsorption of Lysozyme (LSZ) and Bovine serum albumin (BSA) molecules onto MCP or MBG was governed by surface area of mesostructured materials, electrostatic interaction between proteins and mesostructured materials as well as the conformation stability of proteins. The initial *in vitro* protein release rate was affected by the amount of protein being loaded. The secondary structure of the proteins was preserved after release. MCP and MBG powders of different weight ratios were further being incorporated into the PLGA system to investigate the *in vitro* degradation and protein release behavior. The presence of MCP and MBG (> 10 wt%) increased the bulk hydrophilicity of the PLGA matrix and neutralized the acidic environment caused by the oligomers and monomers degraded from PLGA. As a result, the *in vitro* degradation of PLGA film was retarded without rapid increase of buffer absorption and mass loss. The mid phase degradation of the composite system was competed between the buffering effect of the inorganic bioceramics, leaching of the MCP or MBG and the dissolution of acidic degradation products. The composite release system exhibited multiphasic profile. The initial release rate of the composite film was controlled by the amount of protein adsorbed on the inorganic materials. The higher amount of inorganic samples (i.e. MCP or MBG) could lengthen the mid time phase diffusion process because the inorganic samples could neutralize the pH environment of the matrix and prevent rapid mass loss and buffer absorption to take place. The bioactivity of protein released from PLGA film

showed that there was a peak shift of the negative ellipticity (θ) from 208 nm to 216 nm which indicated a switch from α-helix to β-sheet conformation was induced. As a result, the bioactivity of protein BSA and LSZ released from PLGA film was affected. Several characterization techniques including XRD, FTIR, TGA, nitrogen adsorption analysis, FESEM and TEM were conducted on the surface area optimization of the mesostructured materials. The *in vitro* degradation and the protein adsorption studies were examined using GPC, UV-Vis spectrophotometer, nanosizer and CD spectropolarimeter.

Table of Contents

List of Figures

List of Tables

CHAPTER 1

1 INTRODUCTION

1.1 Background

With the rapid advancement of technology in recent years, people are increasingly pursuing things that are small yet compact and multifunctional. The same is true in the biomedical field. Nanoparticles, particularly, have been intensively studied for a wide range of applications. For instance, silver nanoparticles which served as anti-microbial agent, have been used for early healing for delayed diabetic wounds [1]. Nanoparticles have also been used in tissue engineering to deliver growth factors [2]. On the other hand, they can also serve as delivery transport for diagnostic and therapeutic purposes. For instance, radioisotopes or drugs have been successfully loaded into hydroxyapatite (HA) nanoparticles for systemic delivery and the biodistribution of these nanoparticles were examined non-invasively *in-vivo* [3]. Besides that, solid tumours targeting could also be achieved by using modified nuclear nanoparticles to first release anti-angiogenesis agent from the first layer of nanoparticles, followed by releasing a chemotherapy agent inside tumours [4].

There are many other reports on the study of particulate system as delivery vehicles for therapeutic purposes. Polymer nanoparticles have been used for drug [5, 6] and protein [7] delivery. Besides that, the studies have also extended to organic-based particles including micelles [8, 9] and liposomes [10]. Nevertheless, the delivery function has given a lot of opportunity for the study of inorganic particles for such applications. For example, particles such as iron oxide, gold, fullerenes, calcium phosphate and silica have been studied to serve

different drug and gene delivery purposes including targeted cellular delivery [11-14]. Hence, it is of great interest to further explore the protein delivery function of inorganic nanoparticles which served as carriers in order to enhance controlled delivery.

Still, an outstanding drug delivery system requires many considerations. One of the main worries has been the low drug/protein loading issue [15, 16]. A delivery system should possess high loading capacity to reduce the dosage of the nanoparticles required for administration. On top of that, it would be advantageous if the carrier could work as a protective agent for drugs or proteins against the robust environment inside the body besides serving as an external carrier.

An example of a robust system that has been reported is the use of silica-based materials for delivery of agents. These mesostructured materials of pore diameters between 2 and 50 nm have been reported as an excellent candidate in controlled drug delivery systems [17-19]. It was shown that the high surface area, high pore volume and ordered pore network of the mesostructured materials gave high loading efficiency and the drug loading and release kinetics can be manipulated. Besides that, these unique features of materials have been actively studied in many other fields such as separation, optics, catalysis, sensors [20] as well as in tissue engineering [21, 22].

1.2 Problem statement, hypothesis and novelty

The low loading efficiency of drugs or proteins has been one of the obstacles in particulate delivery system [15, 16]. The reasons could be due to the passive targeting delivery which

leads to leakage of proteins before reaching targeted site. From the perspective of materials science, it is of our interest to design and study a nanoparticle system with suitable matrix material as a delivery vehicle that loads proteins and releases them at a controlled rate. An ideal delivery system should possess high loading capacity to reduce the dosage of the nanoparticles required. Hence, mesostructured materials of higher surface area properties would be introduced to increase the protein adsorption.

Although silica-based mesoporous materials have been widely studied, the task of synthesizing a non-silica based mesostructured material is very challenging and fewer literatures had been reported. In general reported mesoporous non-silica materials such as calcium phosphate has a very low surface area of less than 100 m^2/g [23-26]. However, it was believed that the potential of non-silica compositions would be higher than that of the conventional silica mesoporous materials if the properties of the non-silica based materials can be explored and optimized. In addition, no literature has been found to report on the protein adsorption and release from mesoporous or mesostructured calcium phosphates and neither in a hybrid form. This might be due to the failure of optimizing the high surface area mesostructured calcium phosphates in the first place. Therefore, it brought to our attention to synthesize and optimize high surface area mesostructured non silica materials, particularly the non-reported calcium phosphates and followed by discussing their protein adsorption and release profile in a polymer-ceramic hybrid, which is the novelty part of the thesis.

Another issue is preserving the structure of the protein when loaded into particulate carriers. A system with high protein loading but does not retain the structure of the protein bioactivity

is therefore not an ideal delivery system. It has been reported that proteins tend to denature or undergo structural change before reaching the targeted site [17]. For example in protein delivery using polymeric nanoparticles, protein instability in polymer particles [27-29] was due to the harsh environment exposed to the proteins during synthesis and encapsulation process.

Hence, the hypothesis in this work is that mesostructured calcium phosphates would increase the protein loading efficiency consistent with preservation of the bioactivity. The loading of protein under the physiological conditions, which would be possible with the use of pre-synthesized mesoporous calcium phosphates, could help to retain the structure of proteins from deformation.

1.3 Objective and Approach

The objectives of the thesis were to:

(1) Investigate the potential of high surface area mesostructured calcium phosphate in achieving high protein loading

(2) Determine the protein structure after loading onto high surface area mesostructured calcium phosphate

(3) Study protein release and structure released from ceramic/polymer hybrid films

In order to accomplish the objectives, several approaches were defined along the exploitation.

(A) To synthesize and optimize high surface area mesostructured calcium phosphates (MCP) through a novel synthesis route

The synthesis of high surface area mesostructured calcium phosphates (MCP) for biomedical applications had been reported in recent years. Although there were different approaches studied by several groups of researchers, the outcomes of the non-silica material system were less promising (< 100 m^2/g). As a result, the synthesis mesostructured calcium phosphates (MCP) to achieve high surface area were challenging. In this work, the synthesis of MCP using triblock copolymers templating was carried out. Both commercial calcium phosphate (CP) and mesoporous bioactive glasses (MBG) would be used as the controls.

A total of five variants would be explored to achieve high surface area MCP: solvents for surfactant washing, type of non-ionic surfactants (triblock copolymers) for templating, solution pH during precipitation in aqueous solution, synthesis temperatures as well as surfactant concentrations and surfactant removal techniques. The optimized MCP would be used for the next phase of protein adsorption study.

(B) To study the protein loading and release from mesostructured calcium phosphates (MCP), in comparison to mesoporous bioactive glass (MBG) and nonporous calcium phosphate

In this investigation, bovine serum albumin (BSA, IEP = 4.7) and lysozyme from egg white (LSZ, IEP = 11.1) of different surface charge in physiological conditions were used as model proteins. Both protein loading and release measurements were inspected using UV-Vis spectrophotometer. TGA and FTIR were conducted for protein released from inorganic

particles to confirm the presence of protein. The structure stability of protein was examined using Circular Dichroism (CD) spectropolarimeter for protein after release.

(C) To study protein release profile and protein structure released from mesoporous hybrid films

The *in vitro* degradation of pure PLGA films as well as MCP or MBG/PLGA films were carried out in order to determine degradation kinetics of composite films and this would further help in explaining the protein release kinetics later. The protein release from pure PLGA films would be compared against the release of proteins which originally loaded within mesoporous materials in PLGA films. On top of that, the structure of protein released from the films was studied as well.

CHAPTER 2

2 LITERATURE SURVEY

2.1 Mesostructured materials

Porous materials of pore diameters range between 2 and 50 nm was classified as mesoporous materials, according to IUPAC (International Union of Pure and applied Chemistry). Typically, mesostructured materials were formed through surfactant templating, and the surfactant was removed by either high temperature treatment (calcination) [23, 26] or dissolution with the appropriate solvent [30]. Since the breakthrough of M41S family of molecular sieves [31], the mesostructured materials had gained interest in many fields due to their excellent surface area, pore volume and highly ordered pore network [17]. In the past decade, these systems have been promising in several areas such as catalysis, separation, sensors and optics [20].

The mesoporous materials MCM-41 had first reported by Vallet-Regí et al [19] as a drug delivery system in biomedical fields. Different kinds of bioceramics, especially the mesoporous silica materials, had been explored to improve their surface properties in tissue engineering and delivery system [32]. In fact, the outstanding textural properties of mesostructured materials had motivated the study of the adsorption of pharmaceutical drug, enzymes, proteins and biomolecules [17, 33-35]. Additionally, several reports had been demonstrated that proteins preserved their native structure and bioactivity upon adsorption on silica based mesostructured materials [34, 36, 37]. These findings allowed more research on

the protein loading into mesoporous materials. Prior to that, it was important to have an extensive research on the bioceramics, i.e. bioactive glasses and calcium phosphates, which were used in this study in order to understand and design their mesostructure properties for protein adsorption and release.

2.1.1 Bioceramics

Bioceramics have been progressively studied and evolved in the biomedical field from the very first bioinert ceramics to bioactive, bioresorbable and currently with regenerative function [38-40]. This advanced development has lead to an improvement in the tissue-materials response in tissue engineering. For example, calcium phosphates and bioactive glasses have been the suitable candidates in bone tissue engineering due to their osteoconductive properties. The main advantage of inorganic materials was their great biocompatibility. They however encountered problem such as low mechanical strength and high brittleness.

2.1.1.1 Bioactive glasses

Bioactive glasses are extensively used as bone substitute in the treatment of bone defect and osteoporosis [41]. When the glasses were implanted *in-vivo*, a hydroxycarbonate apatite (HCA) layer corresponding to the inorganic phase of bone was formed on the surface of the glass [42]. This HCA layer could then chemically bonded with living bone. The conventional glasses [43] were first discovered by Prof. Hench in 1969. The materials were produced by melt-processing with a main compositional feature of less than 60 mol% SiO_2 in order to

retain the bioactivity [44]. Therefore, bioactive glasses was subsequently made using sol-gel route, which is the synthesis of tertiary bioactive glasses (CaO-P_2O_5-SiO_2). This novel processing could result in a finer porous structure with a higher bioactivity (up to 100 % SiO_2) [45]. The fast surface reactions favoring a quick tissue bonding without the formation of scar tissue has made bioactive glasses promising in scaffold materials [46]. At the same time, drug loading of bioglasses was feasible using the sol-gel method. The release efficiencies however were quite low [47, 48].

To date, the mesoporous bioactive glasses (MBG), which are one of the silica system, have been highlighted in varying compositions [49, 50], calcination temperatures [50], type of non-ionic surfactants [49, 51] as well as drug release studies [52-54] to determine their bioactivity and textural properties for tissue engineering applications. Most of the MBG studied were produced by sol-gel route.

2.1.1.2   Calcium phosphates

Being the inorganic phase of bone, calcium phosphates have been widely studied in bone tissue engineering [55, 56] and drug delivery system [39]. Calcium phosphate ceramics covered a wide range of materials including hydroxyapatite (HA), beta-tricalcium phosphate (β-TCP), carbonated apatite (CA), etc. A list of abbreviations of the commonly studied calcium phosphates family with corresponding Ca/P ratio and pH stability range was given in Table 2.1 [57, 58].

Table 2.1 Abbreviations of calcium phosphate family with corresponding Ca/P-ratio and pH stability range [57, 58].

Abbreviation	Name	Ca/P ratio	pH stability range+
ACP	Amorphous calcium phosphate	$1.25 < x < 1.55$	*
CDHA	Calcium deficient hydroxyapatite	$1.50 < x < 1.67$	6.5-9.5
DCPA	Dicalcium phosphate anhydrate, Monetite	1.00	#
DCPD	Dicalcium phosphate dihydrate, Brushite	1.00	2.0-6.0
HA	Hydroxyapatite	1.67	9.5-12
OCP	Octacalcium phosphate	1.33	5.5-7.0
α-TCP	α-Tricalcium phosphate, Whitlockite	1.50	^
β-TCP	β-Tricalcium phosphate, Whitlockite	1.50	^

+ in aqueous solution at 25 ˚C; # Stable at temperatures > 100 ˚C;
^ No precipitation in aqueous solutions;
* Metastable, precipitation is dependent on the solution pH value and composition

Among the few calcium phosphate compounds, hydroxyapatite (HA) is the most stable compound at normal temperature and pH > 9.5 as shown in Table 2.1. It has been widely applied in hard tissue engineering and coating for implant due to its excellent biocompatibility. Moreover, HA or tricalcium phosphate (TCP) could be used to deliver antibiotics [59, 60], protein [61] and anticancer drugs [62]. Besides that, the polar surface characteristics [63] of HA has favored to use in catalysis, absorbent and separation. The porous structure of HA enhanced tissue growth, thus offering better drug loading capacity.

A number of efforts have been dedicated to extending the mesoporous family to non-silicate materials. The synthesis of mesostructured transition metal oxide had been reported by Huo et al. in1994 [64]. However, the mesopores could not be obtained due to the hardship in removing the template. Soler-Illia et al. [65] had reviewed that fast condensation kinetics and

crystallization processes of the non-silica systems could retard the development in this area. However, there were still a number of reviews covering the non-silica system such as mesoporous carbon, siliconitrides, metals and polymers [66]. Hence, it was believed that the potential of non-silica compositions would be higher than that of the conventional silica mesoporous materials if the problems were solved.

The mesoporous calcium phosphate (MCP), which is one of the interests in our study, had been demonstrated in several reports. However, due to the drawbacks of non-silica system as mentioned earlier, the textural properties including surface area has failed to achieve a similar result as the silica system. Wang et al [23], Prélot and Zemb [24], Yao et al [25] and Coelho et al. [67] had synthesized calcium phosphates through cationic surfactant templating and calcination to obtain different structures. However, the textural properties had either not been discussed or low surface area (< 40 m^2/g) was resulted. In addition, mesostructured calcium phosphates were produced by mixed-surfactant approach [68] as well. The high temperature calcinations had led to the disordering of mesostructure, with 90 m^2/g surface area was achieved. In addition, anionic surfactant templating [69] to form lamellar mesostructured calcium phosphates had been successfully synthesized. Yet, the textural properties had not been discussed in detail. Likewise, the mesostructured HA was synthesized using non-ionic surfactant templating [26] but the outcome was non-repeatable. It was deduced that calcination was not suitable in the synthesis of mesoporous calcium phosphates, since the BET surface area was relatively low compared to existing mesoporous silica-based materials [17, 70].

Besides surfactant templating, Guo et al. [71] had soaked calcium carbonate particles in phosphate buffer without using any structure directing agents and obtained a deposition layer of non ordered slit shaped mesopores on the surface. In this case, the stability of the structure was a problem. Besides that, Ikawa et al. [72] had successfully fabricated lamellar mesostructured calcium phosphates using ionic bonds in mixed solvent systems using *n*-alkylamines. However, it was important to make sure the use of this kind of alcohols would not lead to toxic problems.

2.1.2 Ceramic/biodegradable polymer composites

Poly(α-hydroxyester)s such as poly(lactic acid) (PLA), poly(glycolic acid) (PGA) and poly(lactic-co-glycolide) (PLGA) copolymers were the most extensively studied biodegradable polymer in biomedical applications.[73, 74] and had been approved by the US Food and Drug Administration (FDA) [75]. The chemical properties of these polymers allowed hydrolytic degradation through de-esterification. The oligomers and monomer products degraded from polymer were removed by natural pathways. However, the abrupt release of degradation products such as oligomers and monomers during bulk erosion could provoke inflammatory response [76, 77].

Combining the advantages of both polymers and ceramics, better mechanical and physiological demands of the composite system was attractive. The incorporation of polymers into ceramic phase could enhance the mechanical strength of the ceramics. At the same time, the presence of either calcium phosphates or bioactive glasses could neutralize the

acidic environment caused by the oligomers and monomers in polymer matrix [78-80]. Additionally, inorganic materials have been shown to increase the bulk hydrophilicity of the polymer matrix [78], thus changing the degradation profile of polymer.

Ceramic/ biodegradable polymer composites had been reviewed by several groups of researchers [57, 79, 81]. The composites have shown to exhibit excellent properties in tissue engineering and delivery system. However, the incorporation of mesoporous ceramics into biodegradable polymer matrix was still a new and exciting research to explore. Li et al. [82] reported that mesoporous bioactive glasses (MBG)/ /polycaprolactone (PCL) had an improved hydrophilicity and a denser and uniform apatite layer was formed as compared to nonporous bioactive glass (BG)/PCL composite. Besides that, Xue and Shi [83] examined the drug release properties by comparing poly(D,L-lactide-co-glycolide) (PLGA)/mesoporous silica hybrid structure to a single mesoporous silica structure. Results showed that the composites were able to release gentamicin for a longer period of time with a reduced initial burst release. Wu et al. [84] studied the effect of MBG on PLGA matrix. Comparing to BG/PLGA, the MBG/PLGA possessed superior mechanical properties, *in vitro* degradation, bioactivity as well as drug release properties.

2.2 Protein adsorption in mesostructured materials

The high surface area of mesostructured bioceramics allowed the adsorption onto mesopores and subsequent release of various types of biologically active species such as proteins, polypeptides or amino acids [33-35]. More importantly, findings had confirmed the retention

of the proteins native structure and bioactivity upon adsorption [34, 36, 37] on mesostructured materials.

2.2.1 Model proteins

The adsorption of protein molecules onto ordered mesostructured materials were greatly reviewed by Hartmann [85] for applications such as biosensors and biocatalysts. On the other hand, Kandori et al. [86-88] had published many papers on various protein adsorptions onto hydroxyapatites to explore different possibilities from the outcome. At the same time, Imamura et al. [89] had studied the adsorption characteristics of 18 proteins on titanium oxide surface. Through their evaluation, Bovine serum albumin (BSA) and Lysozyme (LSZ) of different surface charge and structural stability were employed as model proteins in our study.

2.2.1.1   Bovine serum albumin (BSA)

Bovine serum albumin (BSA) is a large (MW = 67.2 kDa) ellipsoidal ($4 \times 4 \times 14$ nm^3) protein. It is composed of a single-chain of 582 amino acids [90] and is predominantly alpha-helical (67 %) structure [91]. BSA is the main constituent in plasma proteins and contributes to colloid osmotic blood pressure [91] as well as the maintenance of blood pH [92]. As shown in Table 2.2, the isoelectric point (IEP, pI) of BSA is 4.7. The pI is the pH value in solution at which the sum of the charges on the protein is zero. Therefore, it is a negatively charged or acidic protein in normal pH 7.4 environment. BSA started to undergo

conformational change at around 58 °C [93] and the temperature of denaturation was 62°C [94].

The low structure stability of BSA allowed structural rearrangements upon adsorption by a large driving force. As a result, such "soft protein" was able to adsorb on and any surfaces under attractive and repulsive electrostatic conditions.

Table 2.2 Properties of protein.

Protein	IEP [86, 95]	MW (Da) [86]	Dimension (nm^3) [95]	Conformational Stability [96]
BSA	4.7	67200	4 x 4 x 14	Low (Soft)
LSZ	11.1	14600	3 x 3 x 4.5	High (Hard)

IEP, Isoelectric point; MW, molecular weight

2.2.1.2 Lysozyme (LSZ)

The protein hen egg white Lysozyme (LSZ) is a small (MW = 14.6 kDa) globular (3 × 3 × 4.5 nm^3) antimicrobial protein. This enzyme is composed of 129–131 amino acids [97]. LSZ has one side dimension of 3.0 × 4.5 nm^2 and another end of dimension 3.0 × 3.0 nm^2 [98]. LSZ has a lower content of α-helical conformation [99] as compared to BSA. As shown in Table 2.2, the isoelectric point (IEP, p*I*) of LSZ is 11.1. Hence, LSZ is a positively charged

or basic protein in normal pH 7.4 environment. LSZ undergoes denaturation at temperature around 60 - 76°C [100, 101].

It has been also reported that the conformation structure of LSZ is highly stabilized due to the four internal disulfide bonds help to retain its tertiary structure. Such "hard protein" do not undergo structural rearrangements during adsorption [102] within the pH range from 1.5 to 12 at physiological temperature. In addition, LSZ is known to favorably adsorb on all hydrophobic interfaces under all conditions but only on hydrophilic surfaces of oppositely charged.

2.2.2 Protein adsorption

A successful protein delivery system displays high loading efficiency in order to minimize the required carrier dose for administration Besides that, for protein adsorption on inorganic materials, it is important to preserve the bioactivity of enzyme under extreme conditions *in-vivo*.[103]. Hence, the effect of several parameters on the protein loading capacity would be discussed here in order to have a better understanding on the outcome of the protein studies.

2.2.2.1 Surface area

For protein loading in mesostructured materials, surface area would be one of the dominant factors because the adsorption process was primarily dependent on the surface properties of the materials. In general, a material with higher surface area would have higher protein

loading [17]. Xue et al. [104] had reported that the mesoporous calcium silicate (between 221 and 356 m^2/g) was able to load higher amount of Lysozyme (LSZ) and Bovine serum albumin (BSA) compared to the nonporous calcium silicates (65 m^2/g). Additionally, a sustained release of protein from mesoporous calcium silicate over a week was observed compared to the few hours burst release profile of nonporous calcium silicate.

In addition, Vallet-Regí et al. [105] synthesized two mesostructure materials of MCM-41 (1157 m^2/g) and SBA-15 (719 m^2/g) for alendronate loading. Under same conditions, the amount of drug adsorbed was higher in MCM-41 than SBA-15, indicating the importance of surface area factor.

2.2.2.2   Pore size

Katiyar et al. [37, 106] had stated that proteins would adsorb in pores that were larger than the hydraulic radius of the protein. Therefore for active adsorption which focused on pore diameters, mesostructured materials with pore sizes smaller than the proteins would be expected to have lower adsorption. However, such material gave higher equilibrium adsorption efficiency which was related to the external surface area of the mesostructured materials. Hence, sometimes protein adsorption would be a competing process between several parameters. In this case, the dominant factor would be between pore size and the external surface area.

2.2.2.3   Electrostatic interaction

It was reported that Cai et al. [107] increased the net negative charge of PLGA by blending with the negatively charged poly(styrene-co-4-styrene-sulfonate) (PSS) for the adsorption of the positively charged Lysozyme (LSZ). Studies showed that the loading efficiency of LSZ was improved due to the charge interaction. On the contrary, the negatively charged Bovine serum albumin (BSA) has the reverse effects in which low loading efficiency was achieved.

Nevertheless, Rezwan et al [108] coated silica particles with positively charged $AlOOH_2^+$ particles on the surface and compared the protein loading efficiency of different proteins. It was unexpectedly shown that the negatively charged BSA exhibited nearly 100 % of protein adsorption in the positively charged AlOOH-coated silica particles but lower amount of adsorption on the uncoated silica particles ($-SiO^-$) which was negatively charged. Likewise, positively charged LSZ adsorbed in higher amount on the negatively charged silica particles but not on the surface of AlOOH-coated silica particles. The importance of electrostatic interaction was thus demonstrated here.

In addition, Burns and Homberg [109] and Servagent-Noinville et al. [110] also agreed that by designing protein and material surface of oppositely charged, high loading capacity could be achieved.

2.2.2.4   Protein structure

The adsorption mechanism was reported to be dependent on the protein structural stability [96, 111, 112]. Proteins of structure which is highly stabilized by Gibbs free energy such as Lysozyme (LSZ) would act like a "hard protein". Such protein was known to satisfactorily adsorb on all hydrophobic interfaces under all conditions but only on hydrophilic surfaces of oppositely charged. Conversely, proteins having lower conformational stability such as BSA were driven by an extra force to undergo structural rearrangements upon adsorption. As a result, such "soft protein" was able to adsorb on any surfaces under hydrophobic and hydrophilic surfaces under attraction or repulsion.

Katiyar et al. [96] reported that the protein loading of SBA-15 was strongly dependent on protein structure. It was realized that exothermic events occurred for protein-surface interaction of oppositely charged. The enthalpy value dropped during adsorption of high surface coverage protein, indicating repulsion between protein and surface. Besides that, a secondary adsorption was observed for protein BSA which allowed structure arrangements during adsorption.

In the recent report, Kandori et al. [86] discovered that the adsorption coverage of LSZ values were much less than that of BSA on HA nanoparticles. This was due to the binding effects of calcium and phosphate ions dissolved in the solutions from calcium phosphates. The dissolved Ca^{2+} ions on the calcium phosphate surface had the tendency to bind to the

negatively charged BSA. In the case of positively charged LSZ molecules, it can be postulated that the dissolved PO_4^{3-} ions offer an adsorption site in an opposite way. Similar binding mechanism were represented by Becourt et al. [113] and Luong et al. [114].

On top of that, Kandori et al. [115] who investigated proteins by desorption method realized that the adsorption affinity of BSA was much stronger than LSZ in hydroxyapatites because the protein BSA exhibited highly irreversible adsorption. This was due to the weak affinity of LSZ to phosphate ions on the calcium phosphate surface as compared to that of BSA which was adsorbed by an electrostatic attractive force. On top of that, since BSA is a "soft protein", the low structural stability adsorb even under a repulsive surface through structural reorganization, resulting in a larger adsorption affinity [102, 111, 112].

2.2.2.5   pH and Isoelectric point (*pI*)

The adsorption would also be affected by the isoelectric point (*pI*) of the protein as well. When the solution pH value was closer to the protein's isoelectric point, a higher protein adsorption capacity were obtained. This is due to the minimization of the repulsive force. [106]. The is in good agreement with the result reported by Vegt et al. [116] where energy barriers to the protein adsorption was higher at pH value away from the isoelectric point. Additionally, the structural stability of a protein was lower at pH closer to isoelectric point, thus favoring structure rearrangements to adsorb more protein.

2.2.3 Protein release mechanisms and kinetics

2.2.3.1 Controlled drug release mechanisms

There are several types of controlled drug release system and some of the systems which might be related to our study will be briefly introduced here for a better insight on protein release profiles investigated.

(A) Diffusion controlled systems

In this system, the release is governed by a rate controlling inert water insoluble polymeric membrane. This system is designed either by encapsulating the drug molecules in a polymeric reservoir or by dispersing the protein in a polymer matrix.

1. Reservoir diffusion controlled systems

The core of drug is surrounded by a polymeric membrane as illustrated in Fig. 2.1. Usually, the dissolution fluid penetrates the shell, the core is then dissolved and drug will diffuse out through the interstitial channels or pores [117]. The release is dependent on the encapsulating material, the rate of the dissolution of drug and the diffusion rate of drug to the outer medium [118]. Some of the examples of the encapsulating material used are hydroxypropyl cellulose [119], ethyl cellulose [120] and polyvinyl acetate [119].
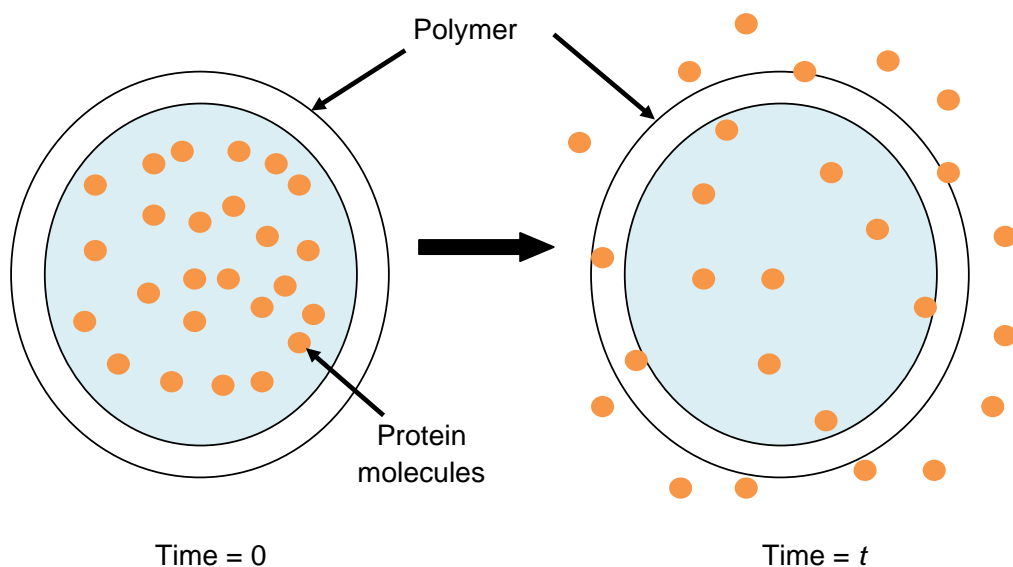
Figure 2.1 Schematic representation of reservoir diffusion controlled system.

2. Matrix diffusion controlled systems

Higuchi [121, 122] had described the release mechanism of drug dispersed in an inert matrix since 1961. The matrix diffusion involves dispersion of drug throughout a hydrophilic polymer matrix as shown in Fig. 2.2. One of the most common methods of preparation is to mix the drug with the matrix material followed by compression to obtain a tablet mixture [123]. Matrix diffusion depends on the solubility of the drug in the polymer [123, 124]. Highly soluble drug would dissolve in the polymer; otherwise, dispersion of drug would occur. The matrix material studied includes Hydroxypropylmethylcellulose [123, 124] and Carboxymethyl cellulose[124].

Protein molecules

Time = 0   Time = *t*
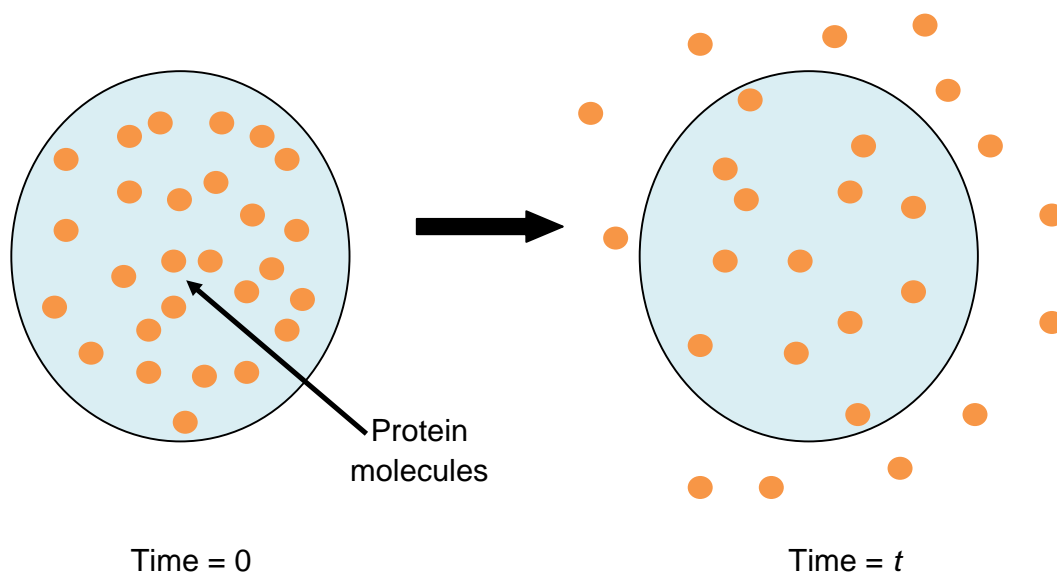
Figure 2.2 Schematic representation of matrix diffusion controlled system.

(B) Swelling controlled systems

In swelling controlled systems, the drug is dispersed in hydrophilic polymer. This system is initially in the glassy state before placing in body or other fluids. Once it gets hydrated, the polymer swells. Swelling further increases the solvent content and the polymer mesh size, resulting in the diffusion of drug from the entire swollen network out to the external surroundings. Hydrogels are the representative polymer used in this system [125].

(C) Erosion controlled systems

In this system (Fig. 2.3), drugs are dispersed in the entire network of the polymer and the rate of drug release is governed by the erosion rate of the polymer. Sometimes, diffusion may also occur in this system. The rate of erosion depends on the surface change of the matrix during erosion as a function of time. Poly(lactide-co-glycolic acid) (PLGA) is the most commonly

studied degradable polymer undergo bulk erosion with significant degradation products accumulated inside the matrix. On the other hand, surface erosion is desirable in this system as we are able to control the release which normally degrades only from the surface layer-by-layer with time. The release rate can be controlled by adjusting the surface thickness and the amount of drug loaded for surface erosion polymer. In general, hydrophobic polymers such as polyanhydrides exhibit surface erosion behavior.
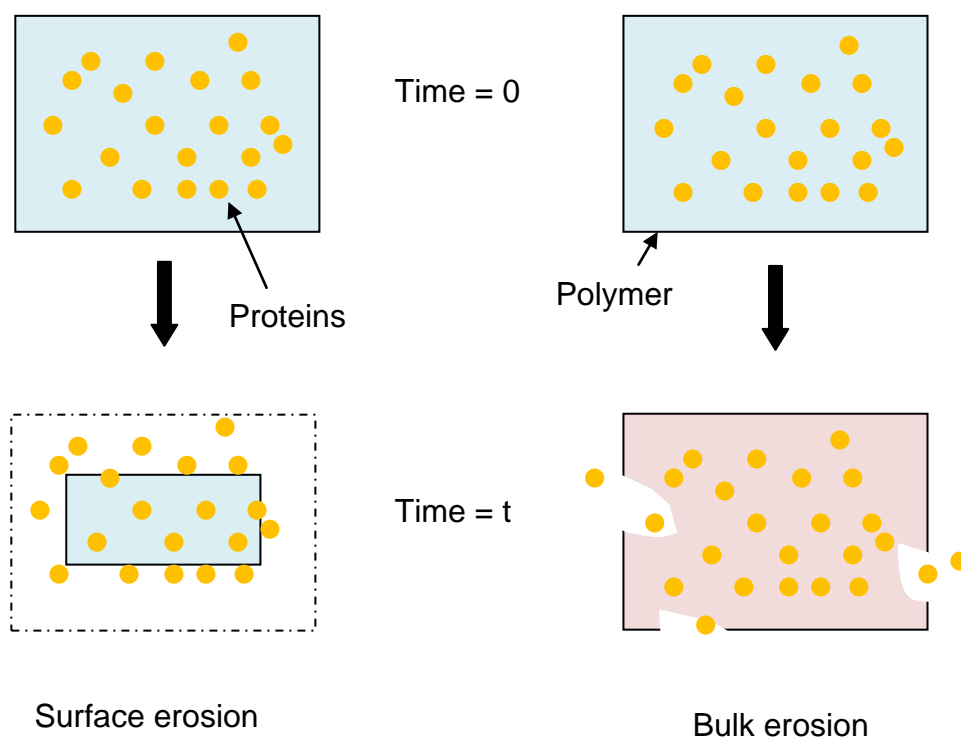
Figure 2.3 Schematic illustration of erosion controlled system.

2.2.3.2   Release kinetics

Different models are used to evaluate the drug release profile. The correlation coefficient (*R*) value calculated in various models decides which model best fits the release data [126-129].

(A) Zero order release

The equation for zero order release is

$$Q_t = Q_0 + K_0 t \tag{2.1}$$

where Q_0 is the initial amount of drug, Q_t is the cumulative amount of drug released at time t and K_0 is zero order release constant.

Zero order release is a model that shows the rate of drug release is independent of time and the concentration of drug loaded. Increasing the concentration of the drug will not speed up the release rate. Such mechanism allows substantial amount of drugs being released over time while maintaining the drug concentration remain within the therapeutic window with time. The graph plotted for a zero order release model will be a straight line of positive slope for cumulative percentage of drug release (y-axis) against time (x-axis).

(B) First order release

The equation for first order release is

$$Log\ Q_t = Log\ Q_0 + K t / 2.303 \tag{2.2}$$

where Q_0 is the initial amount of drug, Q_t is the cumulative amount of drug released at time t and K is first order release constant.

The drug release rate of this model depends on the concentration of the drug loaded. The graph plotted for a first order release model will be a straight line of negative slope for log cumulative percentage of drug remaining to be released (y-axis) against time (x-axis).

(C) Hixson-Crowell release

The equation for Hixson-Crowell release is

$$3\sqrt{Q_0} - 3\sqrt{Q_t} = K_{HC}t \tag{2.3}$$

where Q_0 is the initial amount of drug, Q_t is the cumulative amount of drug released at time t and K_{HC} is Hixson-crowell release constant.

In this model, the drug is released by dissolution and the release is influenced by surface area as well as particles or tablets size. A graph plotted for a Hixson-crowell release model will be a linear line of positive slope for the cube root of the initial concentration of drug minus the cube root of percent remaining $(3\sqrt{Q_0} - 3\sqrt{Q_t})$ (y-axis) against time (x-axis).

(D) Higuchi release

The equation for Higuchi release is

$$Q_t = K_H t^{1/2} \tag{2.4}$$

where Q_t is the cumulative amount of drug released at time t and K_H is Higuchi release constant.

The Higuchi equation suits well in drug release by diffusion. A graph plotted for a Higuchi release model will be a linear line of positive slope for the cumulative percentage of drug release (y-axis) against square root of time (x-axis).

CHAPTER 3

3   EXPERIMENT TECHNIQUES

3.1   Materials

Triblock copolymers Pluronic P123 ($EO_{20}PO_{70}EO_{20}$) was obtained from BASF. EO denotes ethylene oxide and PO denotes propylene oxide. Pluronic F127 ($EO_{100}PO_{65}EO_{100}$) and calcium nitrate tetrahydrate ($Ca(NO_3).4H_2O$, 99 % A.C.S. reagent) were purchased from Sigma-Aldrich. Calcium D-pantothenate monohydrate ($C_{18}H_{32}NO_{10}.Ca$, 98 %) was purchased from Lancaster. Reagent grade potassium hydrogen phosphate trihydrate ($K_2HPO_4.3H_2O$) was purchased from Alfa Aesar. 75/25 Poly(DL-lactide-glycolide) (IV=0.93 dl/g) were purchased from Purasorb. Sodium hydroxide (NaOH) was purchased from Merck. Hydrochloric acid solution (HCl, 1.0 N) was purchased from Sigma-Aldrich. Tetraethyl orthosilicate ($C_8H_{20}O_4Si$, TEOS, 98 %) was from Fluka and Triethyl phosphate ($C_6H_{15}O_4P$, TEP), 99 % was from Sigma-Aldrich. Acetone, ethanol and chloroform ($CHCl_3$, stabilized with 100-150ppm Amylene) were purchased from Tedia. All chemicals were used without further purification. Commercial hydroxyapatite powder was purchased from Fluka, for comparisons with the synthesized MCP. BSA (Albumin from bovine serum, min 98 % electrophoresis) was purchased from Sigma-Aldrich and lysozyme chloride, crystalline (from egg white), LSZ, was purchased from Tokyo TCI Kasei. Phosphate buffer (pH 7.4) was purchased from OHME Scientific.

3.2 Sample preparation

3.2.1 Synthesis of mesostructured calcium phosphates (MCP)

Varying amount of surfactant F127 (or P123) was first dissolved in 50 ml of aqueous solution with overnight stirring at room temperature. 4.945 g of $C_{18}H_{32}NO_{10}.Ca$ (0.01 mol) was next dissolved in 10 ml of water and added into the surfactant solution. After which, $F127/Ca^{2+}$ solution was adjusted to an acidic pH (pH = 1) using HCl and leave it stirring for 3 h. Next, 1.37 g of $K_2HPO_4.3H_2O$ (0.006 mol) was dissolved in 10 ml of water. K_2HPO_4 solution was then slowly added to the acidic $F127/Ca^{2+}$ solution with continuous stirring. This final solution was slowly adjusted to an alkaline pH (varying pH) using NaOH with further stirring for 24 hours. Finally, the mixture was centrifuged. The surfactant molecules were removed by either surfactant washing or calcination at 550 ˚C for 6 h. For samples undergone surfactant washing, the precipitates were further freeze dried for 48 h. The samples were then grounded in an agate mortar for further characterizations. Several synthesis parameters were studied to optimize the textural properties of mesostructured calcium phosphate. The parameters studied were surfactant washing, type of non-ionic surfactant, surfactant concentration, synthesis temperature, and pH.

3.2.2 Synthesis of Mesoporous bioactive glass (MBG)

In a typical synthesis, 5.0 g of F127, 1.4 g of $Ca(NO_3).4H_2O$, 6.7 g of TEOS, 0.73 g of TEP and 1.0 g of 0.5 M HCl were dissolved in 60 g of ethanol solution and stirred at room temperature for 24 hours. The weight ratio was F127/ethanol/0.5 M HCl = 5:60:1 and the molar ratio of $CaO/P_2O_5/SiO_2$ were 5:5:90 where the amount of P_2O_5 was fixed with varying composition. The resulting sol was pour onto petri dish to undergo an evaporation-induced

self-assembly (EISA) process for 24 hours and kept in 50 $^\circ$C oven for the following six days for drying. The dried gel were scrapped off and calcined at varying calcination temperature for different calcination dwell time before grinding into powder to get final product for further characterizations. The parameters examined to optimize the surface area of MBG included silica composition, calcination temperature, calcination dwell time and synthesis temperature.

3.3 Characterizations of MCP and MBG

3.3.1 X-ray diffraction

The phase and crystallographic structures of synthesized MCP were studied by powder X-ray diffraction (XRD), using a Shimadzu X-ray Diffractometer 6000 fitted with a graphite monochromator operating at 40 kV and 30 mA and Cu*Kα* radiation of wavelength 1.541874 Å. Reconnaissance data was recorded by scanning the powder loaded in the glass holders from 10° to 80° in 0.02° 2θ and dwell time of 2 s. The XRD pattern of MBG was collected using Cu*Kα* radiation by a Bruker D8-ADVANCE X-ray Diffractometer running at 40 kV and 40 mA. Data were accumulated with a step scan increment of 0.02º 2θ and dwell time of 1 s over the angular range of 10 to 70°.

3.3.2 Fourier transformed infrared spectroscopy

The chemical and structural composition of MCP and MBG were studied with Fourier transform infrared spectroscopy (FTIR) (Perkin-Elmer FTIR 1600 spectrometer) in the

frequency range of 400-4000 cm^{-1}. For each spectrum, a 32-scan interferogram was collected at a single beam mode with a 4 cm^{-1} resolution. Before characterization, the samples were mixed with potassium bromide (KBr) before compacting into transparent discs for measurements.

3.3.3 Thermogravimetric analysis

Thermogravimetric analysis (TGA Q500 V6.5 Build 196) was used to determine the decomposition temperature of pure surfactant as well as to confirm the absence of surfactant in the synthesized MCP and MBG powders after surfactant removal. Approximately 5 - 10 mg of the powders was placed on a platinum pan. Measurements were performed at 10 ˚C/min from room temperature up to 800 ˚C under the nitrogen flow of 40 ml/min.

3.3.4 Nitrogen adsorption analysis

Full nitrogen (N_2) adsorption-desorption isotherms of MCP and MBG were collected on a Micromeritics ASAP 2020 gas adsorption analyzer at 77 K after degassing the samples at 473 K for 240 minutes. The surface areas of sample powders were calculated according to the Barrett-Emmett-Teller (BET) equation. The relative pressure P/P_0 of the isotherm was studied between 0.01 and 1.0. The pore parameters (pore volume and pore diameter) were calculated from the adsorption branches of the isotherm from the Barrett-Joyner-Halanda (BJH) model. The types of isotherms were evaluated according to their shape and type of hysteresis loops between the adsorption–desorption modes [50, 130].

3.3.5 Field emission scanning electron microscope

Field emission secondary electron images (SEI) were collected at accelerating voltage of 5 kV to examine the particle morphology of the samples using a JEOL JSM-6340F field emission scanning electron microscope (FESEM). Samples were first platinum-coated before microscopy was conducted.

3.3.6 Transmission electron microscope

High resolution transmission electron microscopy (HRTEM) images were obtained from powders ultrasonically dispersed in ethanol for 10 minutes with a drop of suspension deposited on holey carbon-coated copper grids. Data were collected digitally using a JEOL 2010 microscope (C_s = 0.5 mm and C_o = 1.1 mm) operated at 200 kV and fitted with a low-background Gatan double tilt holder and a Si (Li) X-ray detector.

3.4 Protein loading of MCP and MBG

BSA and LSZ loading measurements were studied using UV-Vis spectrophotometer. 250 mg of MCP or MBG powders was added into 50 ml of protein (LSZ or BSA) solution (1 mg/ml) and stirred. The solution was withdrawn at selected time points and replaced with fresh water (2 ml) at each measurement. Protein loading efficiency was calculated as follows [107]:

$$\text{Loading efficiency (\%)} = \frac{\text{Total amount of protein} - \text{Free protein}}{\text{Total amount of protein}} \times 100\ \% \qquad (3.1)$$

For protein release measurements, 20 mg of MCP or MBG loaded protein powders were incubated in 4 ml of phosphate buffer pH 7.4 at 37˚C. The buffer solution was withdrawn at selected time points and replaced with fresh buffer (2 ml) at each measurement. The tests were carried out over a period of 240 h (10 days).

3.4.1 UV-Vis spectrophotometer

For protein studies, the absorbance value of BSA and LSZ were measured at a characteristic wavelength (λ = 280 nm), using UV Spectrophotometer (Shimadzu, model UV-1700). Calibration curve (correlation coefficient > 0.99) was plotted and determined by taking absorbance against protein concentration between 0.01 and 1 mg/ml as parameters. Data were collected at wavelengths between 200 and 300 nm at 0.5 nm intervals against a blank solution using a 1 cm quartz cuvette. Water and phosphate buffer were used as blank solution for protein loading and release studies respectively.

3.4.2 Zeta potential measurement

Zeta potential (ζ, mV) of the protein molecules and the inorganic materials including MCP, MBG and commercial HA were determined by the Zetasizer Nano ZS (Malvern Instruments, Malvern, UK) using Laser Doppler Electrophoresis (LDE) method. Prior to the measurement, the sample was diluted in deionized water. Then, about 1.5 mL of dispersion was injected into the capillary of the zeta cuvette. The cuvette was then place into the Zetasizer and measured at least 3 times with 30 runs each.

3.4.3 Bioactivity studies

In order to ascertain the secondary structure of the protein after being released was retained, bioactivity tests were carried out using Circular Dichroism (CD). The CD measurements were conducted on a JASCO J-810 spectropolarimeter. The far-UV spectra were recorded using a quartz cell of path length 1 mm, at 20 °C. The spectra were scanned between 190 and 260 nm with 0.2 nm resolution. 3 scans were accumulated with a scan rate of 50 nm/min and a response time of 4 s. Spectra were corrected by subtracting the buffer baseline.

3.4.4 Other measurements

Both TGA and FTIR tests were carried out to study the amount of protein loaded as well as the chemical composition of the protein loaded samples. Both measurements aimed to locate the success adsorption of proteins into MCP or MBG.

3.5 *In vitro* degradation studies of MCP/PLGA films

The degradation studies were carried out over a period of 56 days. Both MCP and MBG were incorporated into 75/25 poly (DL-lactide-co-glycolide) (PLGA) using solvent casting method at different weight ratios: 1:99, 5:95 and 10:90. The suspension was cast onto petri dish and left to dry in ambient environment for 2 - 3 weeks. The weight ratios of bioceramics were maintained at a lower percentage to prevent brittleness of the hybrid system. This will generate films with thickness of approximately 80- 120 μm. The films were cut into 1×1 cm and two of the 1 cm^2 films were weighed (W_0) before placing into a sample vial of 10 ml phosphate buffer (PBS), incubated at 37 ^{o}C. At certain time point, different samples would be

taken out for further characterization. The films were rinsed with deionized water and gently wiped dry to obtain wet weight (W_{wet}). The films will be kept in a desiccator for 48 h and weighed to take dry weight (W_{dry}) before subjecting to various characterizations. Meanwhile, phosphate buffer (PBS) was refreshed once every week. Pure PLGA films without incorporation of bioceramics were used as control in this study.

3.5.1 Buffer absorption absorption/uptake

Percentage of film's buffer absorption/uptake of each time point can be calculated from the following equation

$$\% \, Buffer \, absorption = \frac{W_{wet} - W_{dry}}{W_{wet}} \times 100 \, \%$$

(3.2)

3.5.2 Mass loss

Percentage of film's mass loss during film degradation was measured according to the following equation

$$\% \, Mass \, loss = \frac{W_0 - W_{dry}}{W_0} \times 100 \, \%$$

(3.3)

3.5.3 Molecular weight determination

Gel permeation chromatography (Agilent HPLC/GPC 1100 Series) equipped with a RID detector is a relative method to measure the average molecular weight of synthetic polymers. GPC contains column of finely porous particles. Small polymer molecules would then have a longer elution time because they enter the pores. A reflective index detector (RID) would be used to determine the average molecular weight [131]. The molecular weight of polymer was determined at 35 ^oC by GPC using chloroform as eluent. The flow rate of eluent was 1 ml/min while injection volume was set at 50 µL. In addition, calibration was done in accordance to polystyrene standards. The dried films were dissolved in chloroform overnight to obtain a concentration of 2 mg/ml and were filtered before analysis.

3.5.4 Scanning electron Microscopy (SEM)

Scanning electron images (SEI) were collected at accelerating voltage of 5 kV to study the morphology of the film after degradation using a JOEL JSM-6300 scanning electron microscope (SEM). Samples were subjected to 40 s of gold coating prior to the operation.

3.5.5 Other measurements

Thermogravimetric analysis (TGA) was carried out to determine the percentage of MBG or MCP remained inside the PLGA film after *in vitro* degradation.

3.6 Protein release from PLGA film

Lysozyme (LSZ) and bovine serum albumin (BSA) loaded MCP nanoparticles were incorporated into the PLGA phase during solvent casting at a weight ratio of 10:90. The suspension was cast onto petri dish and left to dry in ambient environment for 2 - 3 weeks. The films were cut into 1.5 cm diameter and each film was placed into a 2 ml phosphate buffer well in the 24-well plate, incubated at 37 ^{o}C. At certain time points, films were taken out from the well for UV-Vis and CD study. The release studies were carried out over 84 days (12 weeks) in phosphate buffer at 37 ^{o}C incubator.

3.6.1 Measurements

The absorbance value of BSA and LSZ after release was measured using UV-Vis spectrophotometer. Data were collected at wavelengths between 200 and 300 nm at 0.5 nm intervals against a blank solution using a 1 cm quartz cuvette. Besides that, the structure of the protein LSZ and BSA after release were examined using CD (Circular Dichroism) spectropolarimeter scanned between 190 and 260 nm.

3.7 Statistical Analysis

All experiments were carried out in triplicates. Quantitative data obtained was expressed as mean ± SD (mean ± standard deviation). Statistical analysis of the data was carried out using ANOVA, followed by Tukey's HSD post hoc test (equal variances). Differences were considered statistically significant when the P-value was less than 0.05.

CHAPTER 4

4 SYNTHESIS OF MESOSTRUCTURED CALCIUM PHOSPHATES (MCP)

Optimizing the synthesis procedures was critical in producing high surface area mesostructured materials. Therefore, the changing of synthesis parameters was studied to achieve high specific surface area of mesostructured materials. The variations including surfactant removal techniques, solvents for surfactant washing, type of non-ionic surfactants (triblock copolymers) for templating, solution pH during precipitation in aqueous solution, synthesis temperatures as well as surfactant concentrations were analyzed.

4.1 Surfactant removal techniques

Surfactants could be removed by either calcination [23, 26] or solvent washing [30] after synthesis. In this non-silica system, the effect of surfactant washing and calcination on the BET surface area was explored, as shown in Fig. 4.1 [synthesis condition: (1) solvent: surfactant F127 weight ratio = 1:0.8, (2) RT]. Nonporous commercial calcium phosphate (CP) was studied as the control. It was found that both the commercial (CP) as well as the calcined calcium phosphates displayed a low BET surface area (< 45 m^2/g). At elevated temperatures (i.e. calcination), the collapse of the mesostructure due to the growth of nanocrystals beyond the inorganic wall could be responsible for this decrease of BET specific surface area [24, 65]. Conversely, with surfactant washing using water, the surface area of mesoporous calcium phosphates (MCP) achieved an average of 263 ± 36 m^2/g, which was almost an 840 % increase with reference to the commercial product. The thermogravimetric

analysis (TGA) was also conducted on all the samples to verify that the surfactants were completely removed after synthesis [132].
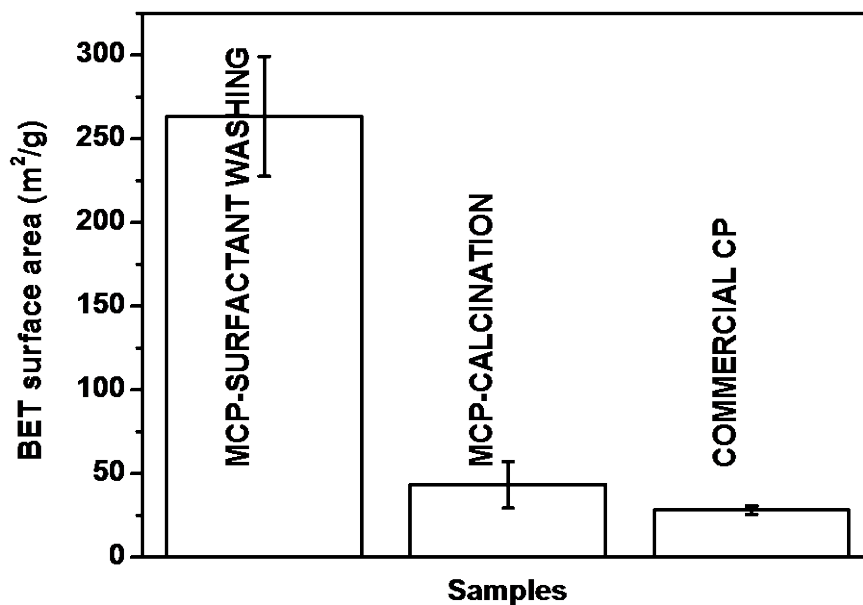
Figure 4.1 BET surface area comparison of synthesized MCP by surfactant washing, by calcination and commercial calcium phosphate (CP, control).

Fig. 4.2 plots the full nitrogen adsorption-desorption isotherms of the synthesized MCP by surfactant washing, by calcination and commercial CP samples. The isotherms of MCP by surfactant washing and calcination were of type IV and exhibited hysteresis loop of H1 type according to IUPAC classification [50, 130]. The isotherms with hysteresis loop at $P/P_0 \approx$ 0.65 for MCP by washing and $P/P_0 \approx 0.85$ for MCP by calcination revealed the mesoporous surfaces of these samples. On the other hand, commercial CP displayed a type III isotherm, which referred to a non-porous solid [50].
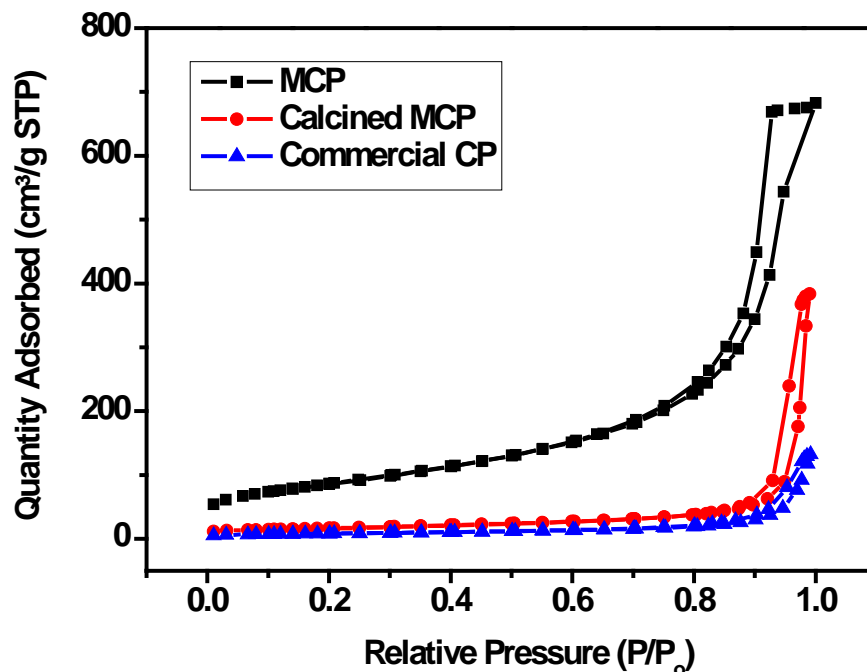
Figure 4.2 Nitrogen adsorption-desorption isotherms of synthesized MCP by surfactant washing, calcination and commercial calcium phosphate (CP, control).

As shown in Fig. 4.3a, the transmission electron (TEM) micrograph of the mesostructured calcium phosphate (MCP) synthesized at room temperature and underwent surfactant washing displayed particles sizes between 30 and 80 nm. The calcined MCP (Fig. 4.3b) exhibited a relatively large size between 100 and 150 nm. The particle sizes of commercial CP (Fig. 4.3c) were between 100 and 200 nm. Particle sizes of calcium phosphates increased at elevated temperature due to crystal growth. In addition, the high resolution TEM (HRTEM) images (Fig. 4.4) of MCP particles showed an ordered lattice structure and the diffraction pattern (inset) exhibited the characteristics of polycrystalline calcium phosphates.
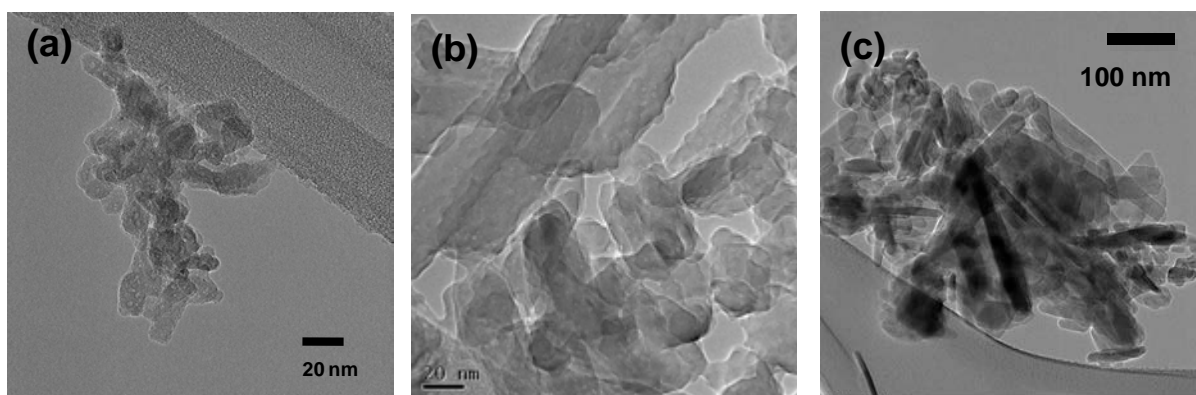
Figure 4.3 Transmission electron micrographs of (a) MCP synthesized using surfactant washing (mag = 20 nm), (b) calcination (mag = 20 nm) and (c) commercial CP (mag = 100 nm).
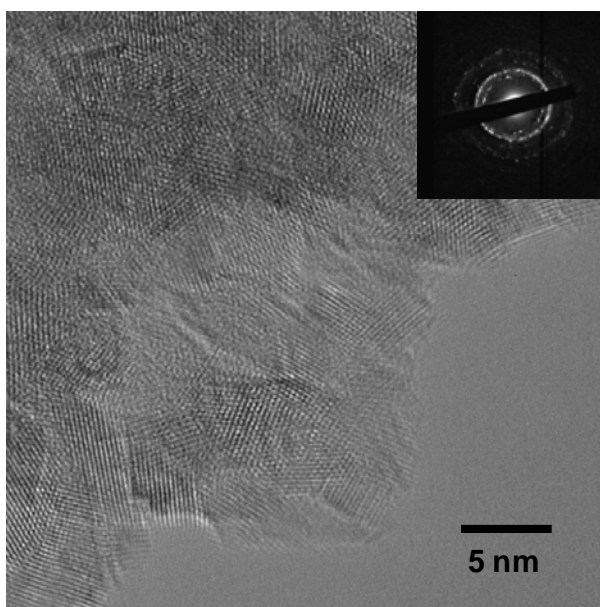
Figure 4.4 Lattices image of MCP synthesized using triblock copolymer F127 and its diffraction pattern (inset).

4.2 Solvents for surfactant washing

Surfactants which were not completely washed away could contaminate the biomaterials [71]. Therefore, an appropriate solvent to dissolve the block copolymers, leaving behind mesostructure template, was necessary to obtain high surface area calcium phosphates. In our

study, water and several solvents including ethanol, acetone and dichloromethane (DCM) were tested in surfactant washing. Fig. 4.5 shows the BET surface area of calcium phosphates [synthesis condition: (1) solvent: surfactant P123 weight ratio = 1:0.4, (2) 40 °C] which were surfactant-washed using water, ethanol, acetone and DCM, respectively. The results showed that DCM washing gave calcium phosphate of lowest BET surface area. On the contrary, samples washed using either water or ethanol showed relatively high surface area on the samples.
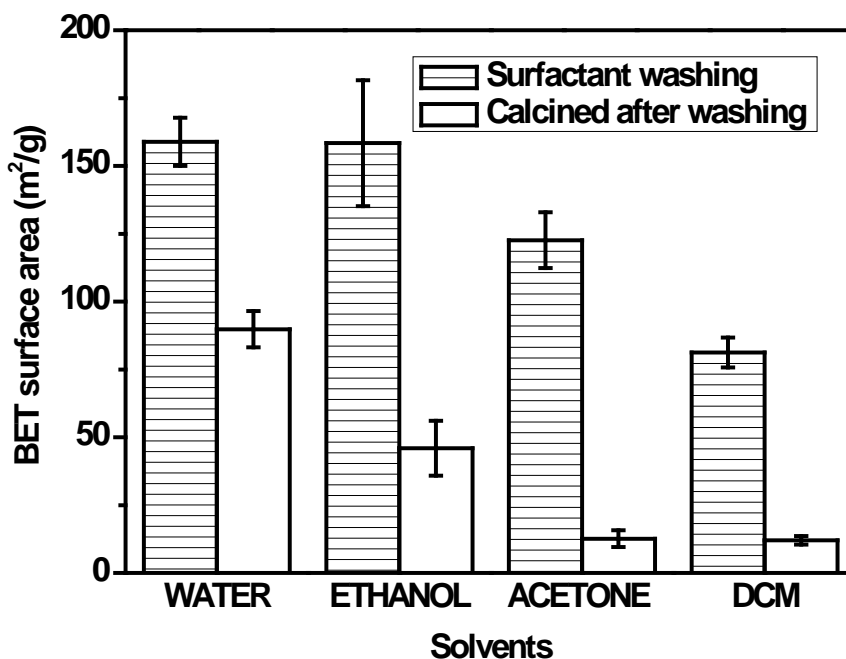
Figure 4.5 BET surface area comparison of MCP samples washed and calcined after washing by different solvents including water, ethanol, acetone and DCM.

The presence of surfactant after washing was determined by thermal analysis. For water and ethanol washing calcium phosphates (Fig. 4.6), around 8 - 10 % weight losses were found which was due to the loss of adsorbed solvent at the temperature range of 25-400 °C without an additional drop at temperature range closer to 300 °C (decomposition temperature of

F127). The MCP samples were stable up to 800 °C. Hence, it was confirmed that the surfactant was completely washed away from the template. Conversely, there were decreases in weight change at temperature of 30 – 80 °C (first drop), 150 – 250 °C (second drop) and 600 – 700 °C (third drop) as highlighted in thermograms of calcium phosphates which were washed by acetone and DCM, respectively. The first drop could be attributed to the vaporization of the relative solvents; while the second drop of weight could be due to the decomposition of organic substances (i.e. surfactant). This implied that there were surfactants left inside calcium phosphates even after repeated washing since the decomposition temperature of a pure Pluronic F127 were around 300 °C (inset). The third drop of weight change after 600 °C was possibly due to the early thermal decomposition of calcium phosphates.
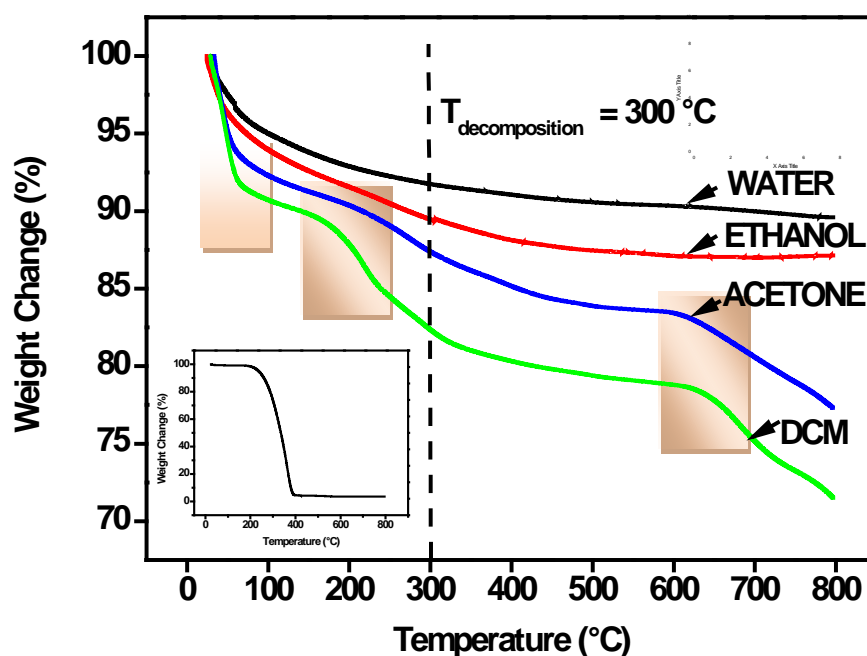
Figure 4.6 Thermograms comparison of MCP samples washed by different solvents: water, ethanol, acetone, DCM; and thermogram of the pure F127 surfactant (inset).

Among the four solvents explored, water (H_2O, $\varepsilon_r \sim 80$) and ethanol (C_2H_5OH, $\varepsilon_r \sim 24$) are solvents with high solvent polarities (dielectric constants, ε_r) while acetone (C_3H_6O, $\varepsilon_r \sim 21$) and DCM (CH_2Cl_2, $\varepsilon_r \sim 9$) are having intermediate solvent polarities [133-135]. Solvents of high polarity allowed better surfactant removal of these polar non-ionic surfactants, thus giving higher BET surface area. For subsequent washings, water which is an excellent polar solvent would be used since it is physiologically more biocompatible than ethanol.

At the same time, Fig. 4.5 provides a substantial result on the importance of using surfactant washing in the synthesis mechanism. It was shown that the surface area of calcium phosphates decreased 43 %, 71 %, 90 %, 85 %, after calcination in comparison to solvent washing using water, ethanol, acetone and DCM, respectively. The result demonstrated two phenomena. First, the removal of surfactant through high temperature treatment (calcination) resulted in samples of low BET surface area. This could be due to the growth of nanocrystals beyond the inorganic wall at high temperature which resulted in the collapse of the mesostructure [24, 65]. Second, samples that undergone complete surfactant washing prior to calcination tend to have comparatively higher surface area than purely calcined samples. These outcomes were supported by the work done by Soler-Illia et al. [30]. They proposed that selective washing before thermal treatment could protect the mesoporous framework from deterioration. Therefore, it was proven that the BET surface area of mesoporous calcium phosphate was strongly dependent on the surfactant removal techniques.

4.3 Type of non-ionic surfactants (Triblock copolymers) for templating

The effect of the type of non-ionic surfactants on surface area was studied in this section. Two types of triblock copolymers – Pluronic F127 ($EO_{100}PO_{65}EO_{100}$) and P123 ($EO_{20}PO_{70}EO_{20}$) were studied with varying surfactant concentrations and synthesis temperatures. Fig. 4.7 plots the BET specific surface area of MCP synthesized by triblock copolymers F127 and P123 at different surfactant concentrations at room temperature (RT). The MCP samples synthesized by both type of triblock copolymers showed a similar BET surface area of < 20 m^2/g difference in value. Besides that, MCP samples synthesized by F127 and P123 using 0.8: 1 of surfactant: water weight ratio were studied at varying synthesis temperatures (Fig. 4.8). The results showed that there was no significant discrepancy on the BET surface area for MCP synthesized using either surfactant P123 or F127. This could be due to a similar number of PPO chains in both triblock copolymers, where the PPO core size determines the aggregation number of micelles [136, 137]. The outcome was coherent to the work reported by Yan and co-workers [49] where the BET surface area of mesoporous bioactive glasses (70S25C) synthesized by F127 and P123 was of 20 m^2/g difference as well.
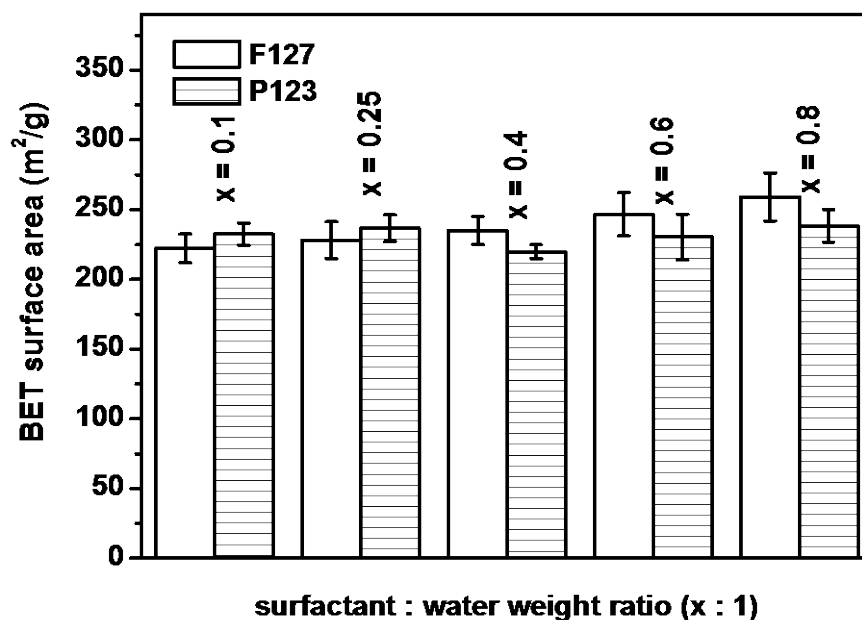
Figure 4.7 BET surface area comparison of MCP samples synthesized at different surfactant concentrations (x:1) for both triblock copolymer F127 and P123.
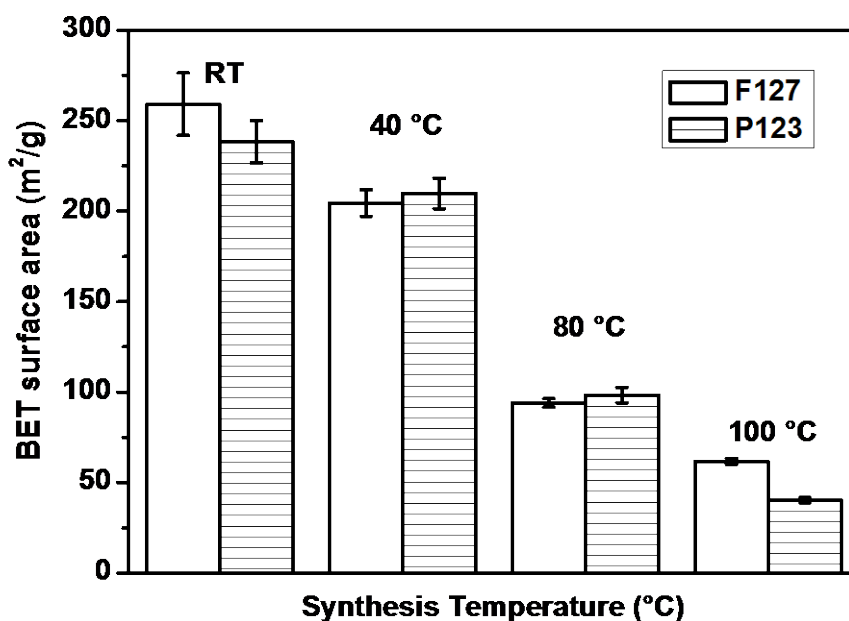
Figure 4.8 BET surface area comparison of MCP samples synthesized at different synthesis temperatures for both triblock copolymer F127 and P123.

Nevertheless, the calcium phosphates templated by either of these triblock copolymers at constant surfactant concentration and synthesis temperature showed similar particle morphologies (Fig 4.9). Calcium phosphates exhibited flake-like structures at low synthesis temperature (i.e. room temperature) and plate-like crystals at high synthesis temperatures (100 °C). Since the two triblock copolymers presented similar textural properties and morphologies at constant temperature and concentration, one of them would be chosen for all the following syntheses. Since there was no difference between either surfactant, so F127 was chosen.
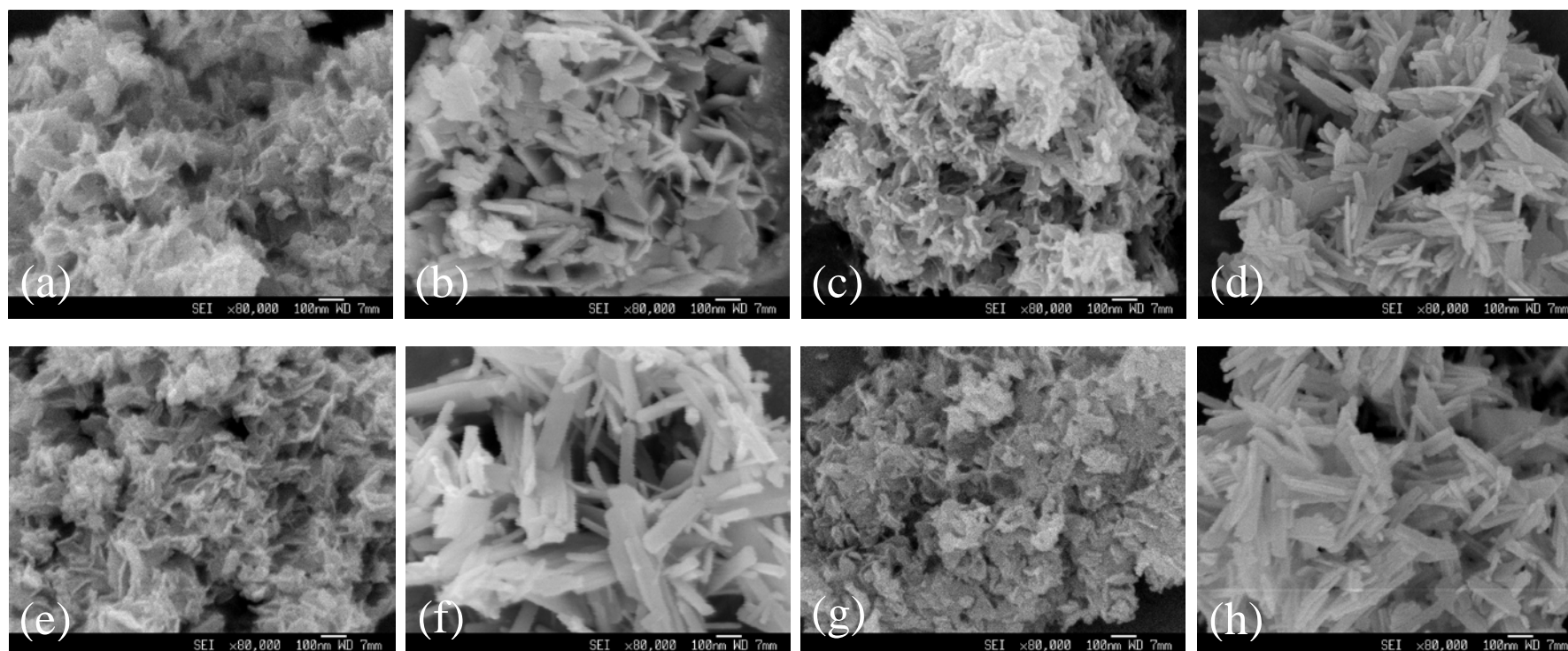
Figure 4.9 Field emission secondary electron images (SEI) of MCP synthesized using F127 (a) x = 0.25, RT; (b) x = 0.25, 100 °C; (c) x = 0.8, RT; (d) x = 0.8, 100 °C and P123 (e) x = 0.25, RT; (f) x = 0.25, 100 °C; (g) x = 0.8, RT; (h) x = 0.8, 100 °C and P123, where surfactant: water weight ratio = x:1, magnification = 80K.

4.4 Solution pH during precipitation in aqueous solution

Precipitation of nonporous calcium phosphate was generally initiated at pH > 4 [138]. The effect of pH on the surface area of MCP templated by F127 was explored. Three different solution pH (i.e. 6, 9 and 12) were analyzed (water: surfactant F127 wt. ratio = 1:0.4) on MCP at varying synthesis temperatures (Fig. 4.10). At higher synthesis temperature (80 °C), the BET surface area increased from 69 to 86 m^2/g, which was around 25 % increase from pH 6 to 12. The BET surface area of MCP stirred at room temperature (25 °C) improved 75 % when the solution pH increased from pH 6 to 12. At constant synthesis temperature, the BET surface area of calcium phosphate increased with increasing solution pH from 6 to 12.
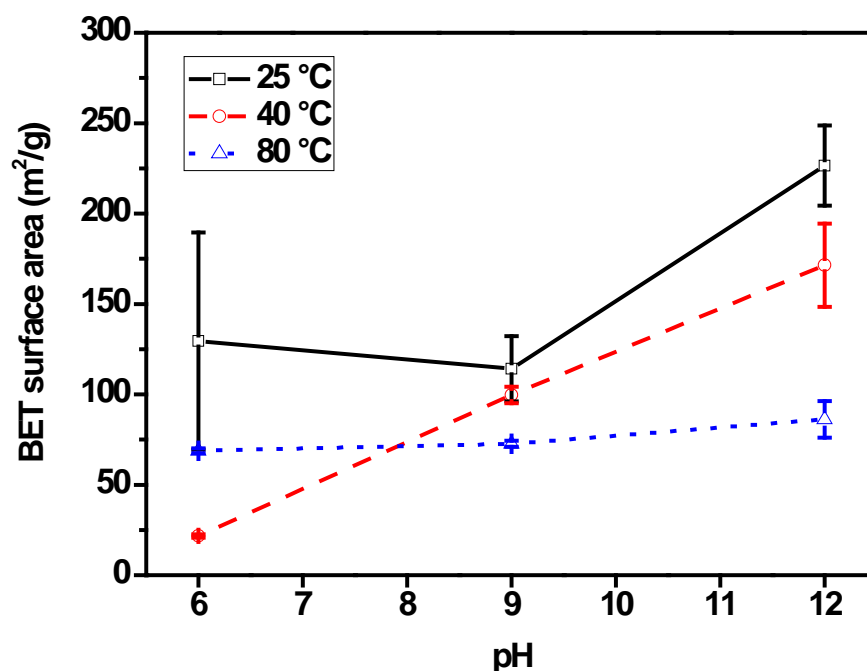
Figure 4.10 BET surface area comparison of pH between 6, 9 and 12 for MCP synthesized at 25 °C, 40 °C and 80 °C.

The nitrogen adsorption-desorption isotherm of MCP precipitated in solution pH 6 at room temperature is represented in Fig. 4.11. The curve exhibited Type IV isotherm with H3 hysteresis loop [130]. Type H3 loop belongs to slit-shaped pores originated from aggregates of plate-like particles as no limiting adsorption was found at high P/P_0. The BJH mean pore size of MCP was mainly distributed at 32.5 Å (inset). On the other hand, MCP prepared at pH 12 (Fig. 4.12) showed Type IV isotherm with H1 hysteresis loop. This curve represented mesostructured materials of cylindrical pores [50, 130]. The sample showed a wide BJH pore distribution at around 90 Å (inset).
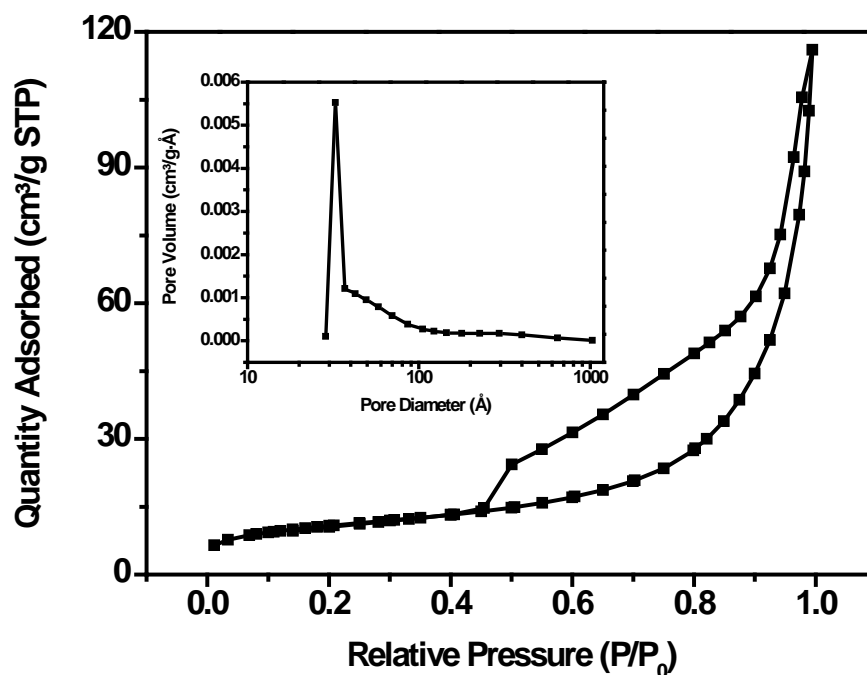
Figure 4.11 Nitrogen adsorption-desorption isotherm of MCP synthesized at pH 6 and its BJH pore size distribution (inset).
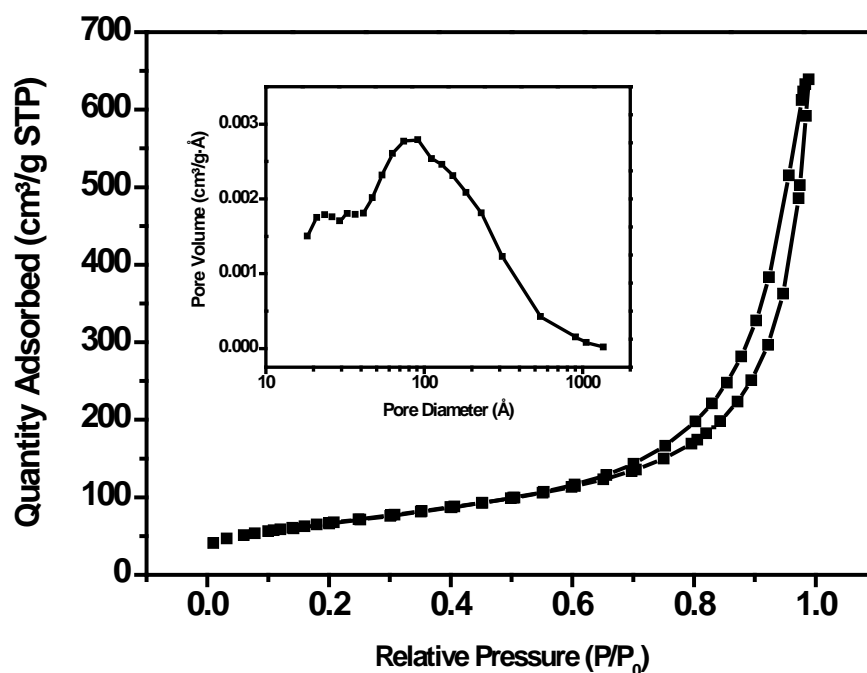
Figure 4.12 Nitrogen adsorption-desorption isotherm of MCP synthesized at pH 12 and its BJH pore size distribution (inset).

There were several phases of calcium phosphate compound prepared by precipitation from aqueous solutions at different pH values [138, 139]. Consequently, the samples were characterized to study the effect of precipitation pH on the phase and crystallographic structures of MCP. As shown in Fig. 4.13, the powder X-ray diffraction (XRD) pattern of MCP precipitated at alkaline medium (i.e. pH 9 and 12) showed the characteristics of single phase hydroxyapatite (HA) [140-142]. The XRD pattern corresponded to the structural model of hydroxyapatite (ICSD #16742) [143]. The broad peak between (211) and (202) represented the less crystalline hydroxyapatite. The diffraction peaks found are (002), (211), (202), (310), (222) and (213) between 25° and 50° 2θ. On the other hand, for MCP prepared at solution pH 6 (Fig 4.14), the XRD pattern studied matched with the main composition of

brushite or named as dicalcium phosphate dihydrate (DCPD, $CaHPO_4.2H_2O$) [144]. The structural model of brushite (ICSD #16738) [145] can be found in ICSD database.
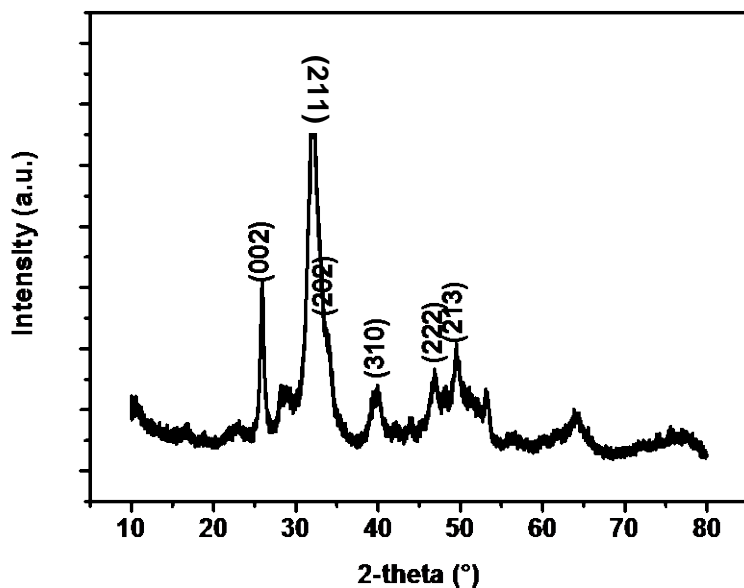
Figure 4.13 X-ray diffraction (XRD) pattern of MCP synthesized at pH 12.
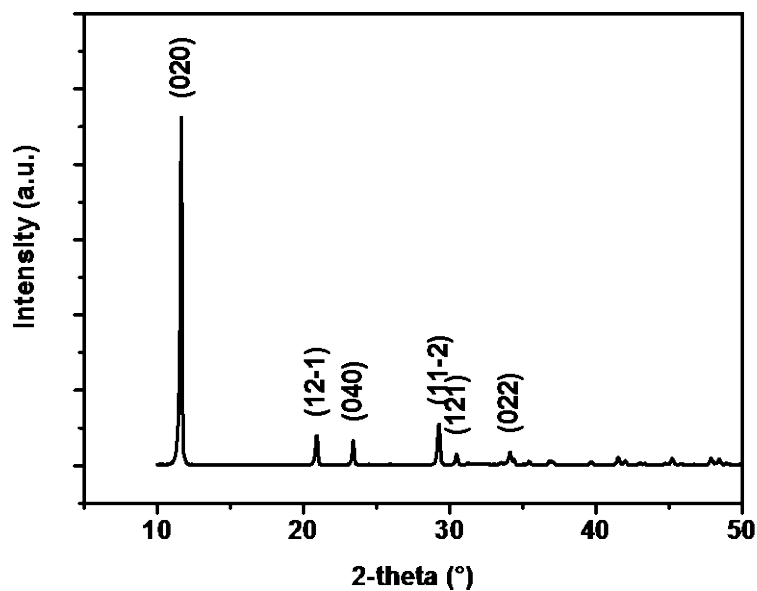
Figure 4.14 X-ray diffraction (XRD) pattern of MCP synthesized at pH 6.

In addition, FTIR analysis was also conducted on MCP precipitated at various solution pH. At pH 12 precipitation (Fig. 4.15), the band of MCP at 3448 cm^{-1} referred to the stretching of the OH group. The v_1 stretching and v_3 vibration of P-O bond of the PO$_4$ group related to the band at 962 cm^{-1} and 1032 cm^{-1}, respectively. The bands at 602 and 563 cm^{-1} showed the mode of v_4 bending of the O-P-O bond. This spectrum exhibited the characteristics of hydroxyapatite (HA) [146, 147]. Besides that, the v_2 and v_3 vibrational carbonate ion centered at 874 cm^{-1} and 1647, 1488, 1421 cm^{-1} indicated the presence of carbonate apatite due to the absorption of carbon dioxide from the atmosphere [148].
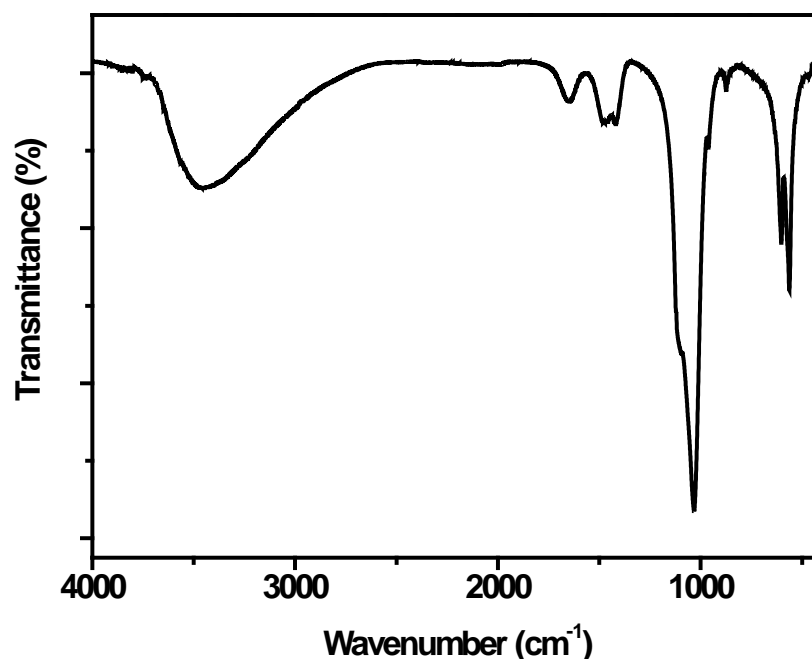
Figure 4.15 FTIR spectrum of MCP synthesized at pH 12.

In Fig 4.16, the FTIR spectrum of MCP precipitated at pH 6 were shown. The bands at 3544, 3491, 3291 and 3164 cm^{-1} referred to the weak H-O-H of the adsorbed water. The bending mode of H-O-H was shown at 1651 cm^{-1}. Besides that, the bands at 1223 and 1134 cm^{-1} was

due to the P=O associated stretching vibration. The bands at 2375, 1725, 576 and 525 cm^{-1} referred to the acid phosphates; while the band at 1059 cm^{-1} was due to the stretching vibration of P=O. The asymmetric stretching vibrations of P-O-P were at 986, 874 and 792 cm^{-1} and the band at 666 cm^{-1} was due to (H-O-) P=O. The FTIR spectrum studied was in good agreement to the reported brushite (CHPD) [149, 150].
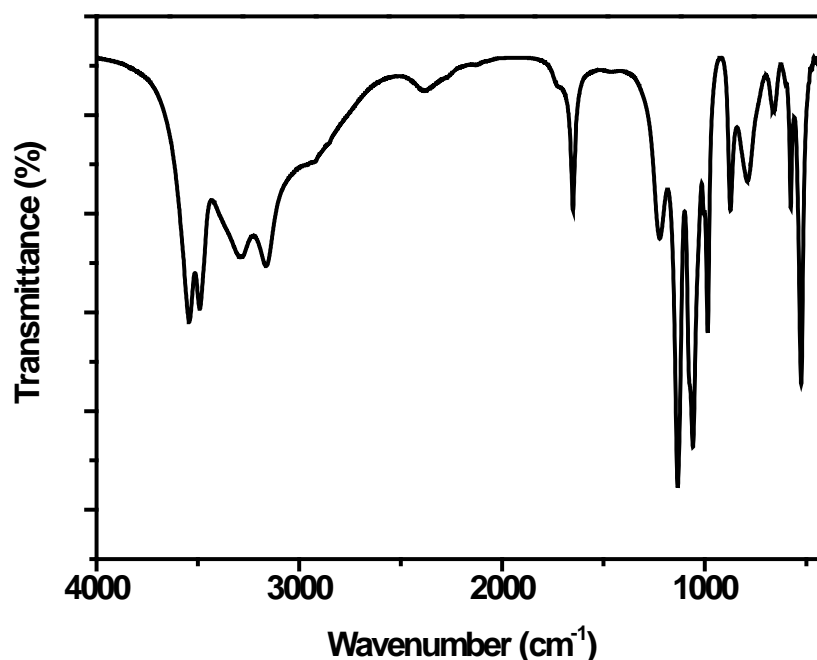
Figure 4.16 FTIR spectrum of MCP synthesized at pH 6.

Besides conducting X-ray diffraction and FTIR analysis, Fig 4.17 represents the thermogram of MCP precipitated at pH 6. The weight change pattern of MCP confirmed the samples as one of the calcium phosphate compound – brushite ($CaHPO_4.2H_2O$) [150]. By heating the powder samples from room temperature to 800 °C, the powder became anhydrous at 300 ˚C ($CaHPO_4$). It then turned into calcium pyrophosphate ($Ca_2P_2O_7$) at around 500˚C and was expected to remain stable up to 1200 ˚C which is the melting point of $Ca_2P_2O_7$ [150]. Similar analysis was performed on MCP precipitated at pH 12 (not shown) as well. No phase

transformation took place upon heating. Around 10 % weight loss which might be due to the loss of adsorbed water at the temperature range of 25-400 °C. There was no further weight loss on heating up to 800 °C, showing the stability of hydroxyapatite (HA).
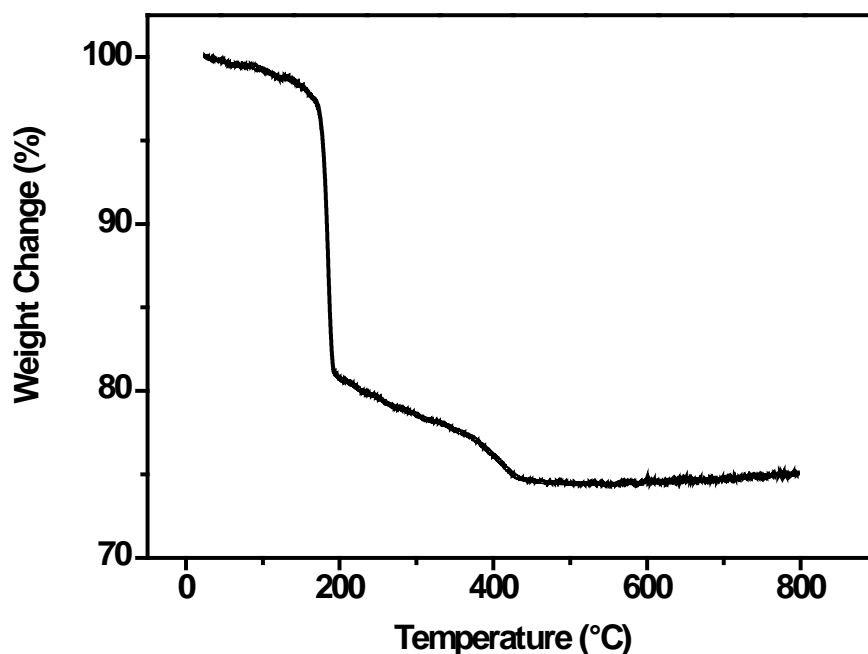
Figure 4.17 Thermogram of MCP synthesized at pH 6.

Overall, the MCP samples studied confirmed its composition as the family of calcium phosphate. Salahi et al. [138] and Kalita et al. [139] had reported that at room temperature, the formation of DCPD, DCP and hydrated calcium phosphate occur pH 4 – 8 while hydroxyapatite were formed at pH > 9.5. In addition, Rodriguez-Lorenzo and Vallet-Regí. [151] revealed that lower pH produced calcium phosphates of lower Ca/P ratios, which was consistent to our experiment result. Therefore, the effect of solution pH on MCP was at no different to those reported on nonporous calcium phosphates. In terms of BET surface area, MCP presented highest value at solution pH 12. Therefore, this synthesis condition would be adopted for the subsequent studies.

4.5 Surfactant concentration and Synthesis temperature

The formation of mesostructured materials took place when the surfactant was above critical micelle concentration (CMC) [152] and temperature (CMT). With increasing surfactant concentration, the CMT of surfactant in aqueous solutions would be lower [153]. In this study, the surfactant concentrations and synthesis temperatures studied were well above the CMC (5.42 wt%) [152] and CMT of F127 (i.e. 1 % w/v F127 block copolymer in water is 24 °C) [154, 155].

Fig. 4.18 plots the BET surface area of MCP synthesized at various surfactant concentrations and synthesis temperatures. The weight ratio of the triblock copolymer F127 to water studied was labeled as x: 1, where $x = 0.1$ (or 9 wt%), 0.25 (or 20 wt%), 0.4 (or 28.5 wt%), 0.6 (or 37.5 wt%) and 0.8 (or 44 wt%), respectively. Both Fig. 4.7 and 4.18 verify that the influence of the F127 concentration on MCP was more significant at room temperature (RT) synthesis. There was a gradual increase of 17 % in BET surface area of MCP, from $x = 0.1$ to $x = 0.8$, at RT synthesis. On the contrary, the impact was less pronounced at elevated synthesis temperatures (i.e. 80 and 100 °C). This was related to the "second CMC" behavior which was investigated by González-Pérez et al. [156]. They revealed that the sphere-to-rod transition of micelles could occur at a lower concentration when the temperature was low. This was because the surfactant concentration required to stimulate the transition at lower temperature was lesser than the aggregation number of the micelles at high temperature. Therefore, a higher surface area of samples could be achieved for MCP synthesized using high surfactant concentration at RT.
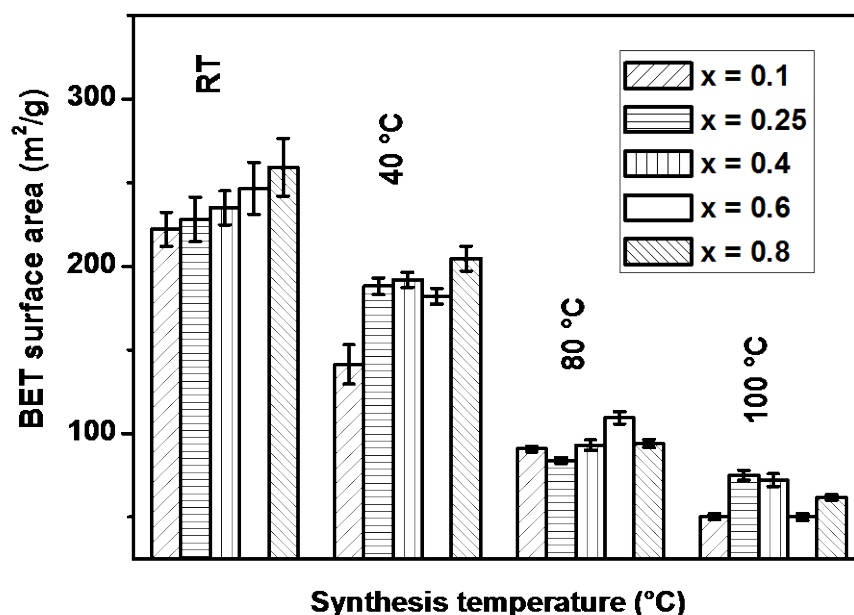
Figure 4.18 BET surface area comparison of MCP samples at different synthesis temperature and surfactant concentration, where surfactant: water weight ratio = x: 1.

Both Fig. 4.8 and 4.18 show the effect of synthesis temperature on the BET surface area of MCP. The BET surface area decreased with increasing synthesis temperature at constant surfactant concentration. The BET surface area decreased on an average of 74 ± 5.5 % from RT to 100 °C for MCP synthesized at different surfactant concentrations. In addition, the BJH pore diameter of MCP increased gradually from an average of 150 Å (RT) to 230 Å (80 °C). This corresponded to the increase in micelle size with increasing synthesis temperature [157].

With increasing synthesis temperature, both PPO and PEO chains would experience dehydration, with the degree of dehydration much higher in PPO blocks. The PPO blocks situated in the central core of micelle became less hydrophilic and the dehydrated water

molecules would start displacing to the outer PEO shell at temperature, T > 40 °C [158]. A similar dehydration was observed for the highly hydrophilic PEO chains at T > 60 °C [65, 159]. As a result, the solubility and the volume of the PEO blocks were reduced, forcing the micelles to undergo restructuring to increase their aggregation number and PPO core radius [136, 137], leading to an increase in pore size. However, the high molecular weight F127 retarded the micelle restructuring and growth process and its hydrophilic character of F127 (70 % EO content) had not showed any micelle shape transition [137]. As the pore size increased, the BET surface area of MCP decreased accordingly [160, 161].

Moreover, the BET surface area of MCP was affected by the crystallite formation of the inorganic samples at higher synthesis temperatures [141, 162]. In order to confirm the presence of these crystallite phases, X-ray diffraction (XRD) analysis was studied on MCP prepared across varying synthesis temperatures. The MCP sample undergone calcination was shown as reference. In Fig. 4.19, the XRD pattern of MCP synthesized at higher temperature possessed sharper intensities and peaks which corresponded to higher crystallinity. The degree of crystallinity was presented by calculating the fraction of crystalline phase (X_c) in MCP using the following equation [163]:

$$X_c = 1 - (V_{112/300} / I_{300}) \tag{4.1}$$

where I_{300} is the intensity of (300) diffraction peak and $V_{112/300}$ is the intensity of the hollow between (112) and (300) diffraction peaks of MCP.
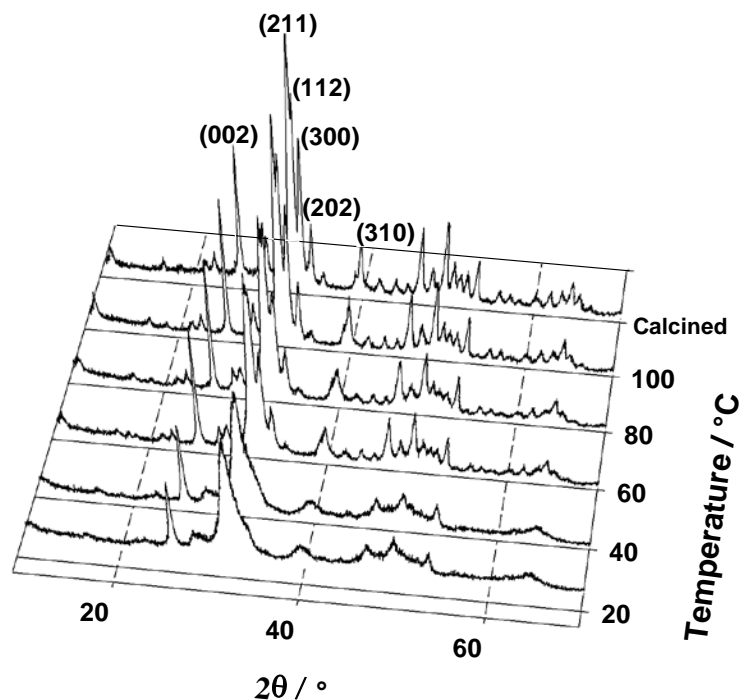
Figure 4.19 X-ray diffraction (XRD) patterns of MCP synthesized at RT, 40 °C, 60 °C, 80 °C, 100 °C and calcined MCP (reference).

The fraction of crystalline phase, X_c of MCP were 0.02, 0.08, 0.21 and 0.44 for synthesis temperature, T = 25 (RT), 40, 80 and 100°C, respectively. Hence, the crystallinity of MCP increased with increasing synthesis temperatures, favoring the nanocrystal growth in these structures [140, 164]. The calcined MCP (Fig. 4.19) showed an analogous diffraction pattern to water washed MCP samples synthesized at elevated temperatures (not shown). This indicated that the crystal growth of MCP was driven by the effect of temperature, resulting in a highly crystalline and ordered sample.

Besides that, the surface morphology of MCP was influenced by the temperature effect as shown in Fig. 4.9. MCP synthesized at room temperature (RT) possessed flake-like crystals

while MCP synthesized at 100 °C exhibited sharp edge crystals of plate-like shape. The low temperature MCP was more agglomerated than those at high temperature. Several studies [162, 165, 166] showed that samples of larger surface area and smaller precipitates tend to form large agglomerates which were ruled by surface energy minimization. Following that, the formation of crystals beyond the inorganic wall at high temperature would result in a lower BET surface area. The morphology changes of MCP, however, were not monitored in the effect of surfactant concentration.

The full nitrogen adsorption-desorption isotherms of MCP with varying surfactant concentrations and synthesis temperatures were explored. The isotherms for varying surfactant concentration of MCP (not shown) exhibited type IV curve and H1 type hysteresis loops [50, 130]. The hysteresis loops across all the concentrations were presented at a similar $P/P_0 \approx 0.65$. At the same time, the MCP synthesized using 0.8: 1 weight ratio of surfactant: water evolved from type IV to type III isotherm with increasing synthesis temperatures (Fig. 4.20). This indicated that the increase in synthesis temperature resulted in a gradual change of mesoporous materials towards non-porous solid.
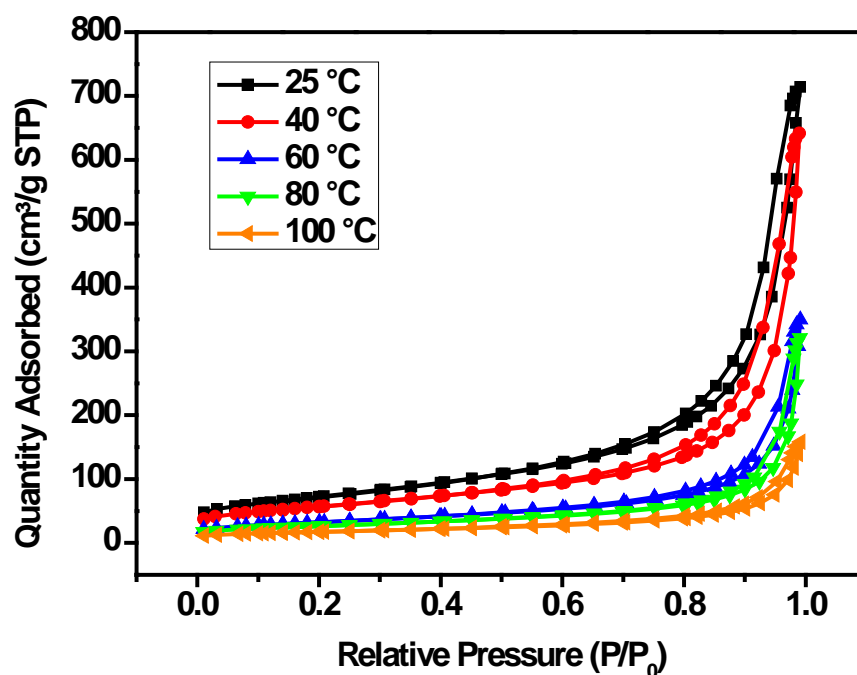
Figure 4.20 Nitrogen adsorption-desorption isotherms of MCP synthesized at RT, 40 °C, 60 °C, 80 °C and 100 °C, where surfactant: water weight ratio = 0.8: 1.

4.6 Summary

In order to obtain high surface area mesostructured calcium phosphates (MCP), several synthesis parameters were studied. First, two main surfactant removal techniques using continuous washing and calcination were carried out. The BET surface area of MCP prepared by surfactant washing (263 ± 36 m^2/g) was 6 times greater than calcined MCP (43 ± 13.8 m^2/g). At the same time, the surfactant washed MCP samples showed almost 840 % increase in BET surface area as compared to commercial CP (control) (28 ± 2.5 m^2/g). The curves of MCP either by washing or calcination showed type IV isotherm (characteristic of mesostructured materials) with H1 hysteresis loops, while commercial CP exhibited the nonporous type III isotherm.

Second, there were four types of solvents (water, ethanol, acetone, DCM) investigated for surfactant washing after the synthesis process. The high solvent polarity of water was confirmed to be a better solvent to remove the traces of surfactant in the MCP solution and it presented a higher BET surface area value. In addition, the importance of surfactant washing was shown here. For samples undergone washing before calcination (Fig. 4.5), their BET surface area was higher than calcined MCP without washing (Fig. 4.1).

Third, triblock copolymers Pluronic F127 and P123 were investigated in mesostructure templating. It was shown that both of these water soluble copolymers gave similar BET surface areas and particle morphologies of MCP at constant temperatures and surfactant concentrations. In our study, Pluronic F127 was adopted.

Fourth, the precipitation pH of MCP during synthesis was studied. Through several characterization experiments, it was observed that all the samples studied from pH 6 to 12 were calcium phosphates. With increasing pH, the BET surface area of MCP increased. The MCP compound precipitated at pH 6 was brushite (DCPD) of mean pore size distributed at around 32 Å. For precipitation at pH 9 and 12, the composition of the samples was confirmed as hydroxyapatite (HA) of mean pore size mainly distributed at 90 Å. The MCP samples gave type IV isotherm with hysteresis loops of type H3 (slit-shaped pores) at pH 6 and H1 (cylindrical pores) at pH 9 and 12.

Fifth, the effect of surfactant concentrations and synthesis temperatures were explored. The influence of the synthesis temperature was dominant as compared to surfactant concentration. The BET surface area increased with increasing surfactant concentrations at RT. With

decreasing synthesis temperature, the BET surface area of MCP increased and the samples were less crystalline. The synthesis temperature had a great influence on triblock copolymer behavior and the degree of crystallinity. On top of that, the morphology of MCP changed from flake-like to plate-like crystals with increasing temperature.

Overall, high BET surface area was achieved with the following synthesis requirements: (1) water washing without calcination, (2) triblock copolymer Pluronic F127, (3) pH 12, (4) high surfactant concentration and (5) low synthesis temperature. This optimized synthesis parameters would be adopted for further studies with proteins.

CHAPTER 5

5 SYNTHESIS OF MESOPOROUS BIOGLASSES (MBG)

Mesoporous bioactive glasses (MBG) have been widely studied [50] and have shown to be a good candidate in drug delivery system [52-54]. MBG which is a silica system can be easily introduced by evaporation-induced self-assembly (EISA) in the presence of surfactant. In our study, all the MBG samples templated using surfactant F127 ($EO_{100}PO_{65}EO_{100}$) underwent EISA process in air for the first 24 h and in 50 °C oven for the subsequent 6 days to speed up the processing time. The synthesis parameters of MBG including silica composition, calcination temperature, calcination dwell time and synthesis temperature, were studied to compare with the MCP samples in the next chapter of protein studies.

5.1 Silica composition

Mesoporous bioactive glasses (MBG, denoted as M) of 4 different molar ratio of silica SiO_2 (denoted as S) to calcium oxide CaO (denoted as C) including M40S45C, M60S35C, M80S15C and M90S5C were calcined at 600 °C for 5 h. The average BET surface area of MBG samples (Fig. 5.1) was sorted in ascending order where M40S45C <<< M60S35C < M90S5C ≤ M80S15C. The outcome of this oven dried samples was in good agreement with those reported by Yan et al. [50, 167] under similar synthesis condition except their EISA process was conducted at RT. With increasing silica content, due to higher concentration of nucleating sites in the gel-glasses [168], BET surface area was higher.
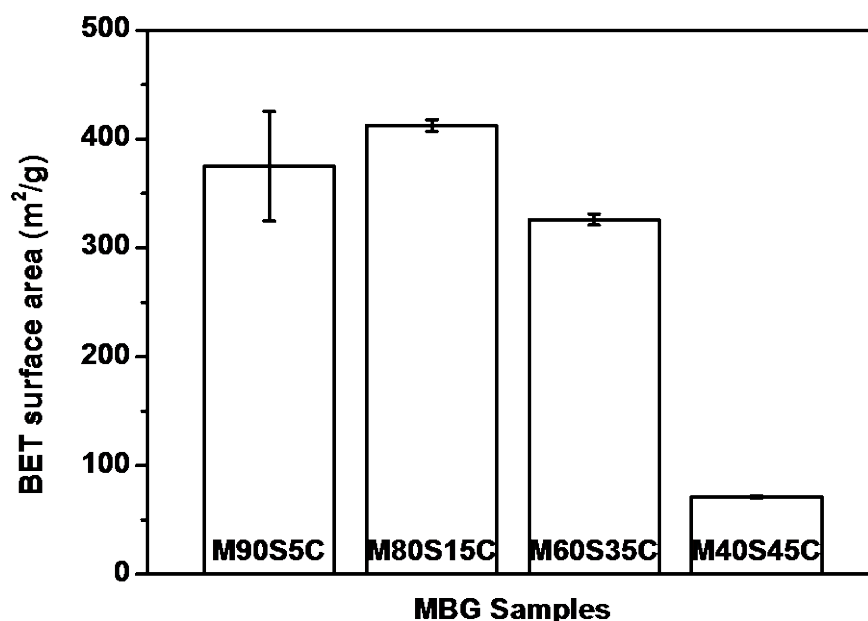
Figure 5.1 BET surface area comparison of MBG of different silica compositions: M40S45C, M60S35C, M80S15C and M90S5C.

The nitrogen adsorption-desorption isotherms of MBG (Fig. 5.2) were confirmed as type IV with H1 hysteresis loop [50, 130]. According to IUPAC classification, this type of isotherm is typical in mesostructured materials of constant cross section pores (i.e. cylindrical or hexagonal). Quantitatively, the isotherm shown after the low pressure adsorption step was steeper in M80S15C, followed by M90S5C and M60S35C, The lowest slope was found in M40S45C isotherm which corresponded to the lowest mesopore surface area among MBG samples. Nevertheless, the sharper feature in the pore-filling step curve of both M90S5C and M80S15C referred to a narrower pore size distribution. This correlation was further studied. For M40S45C, the hysteresis loop shifted to a much higher pressure, indicating larger pores was formed [169].
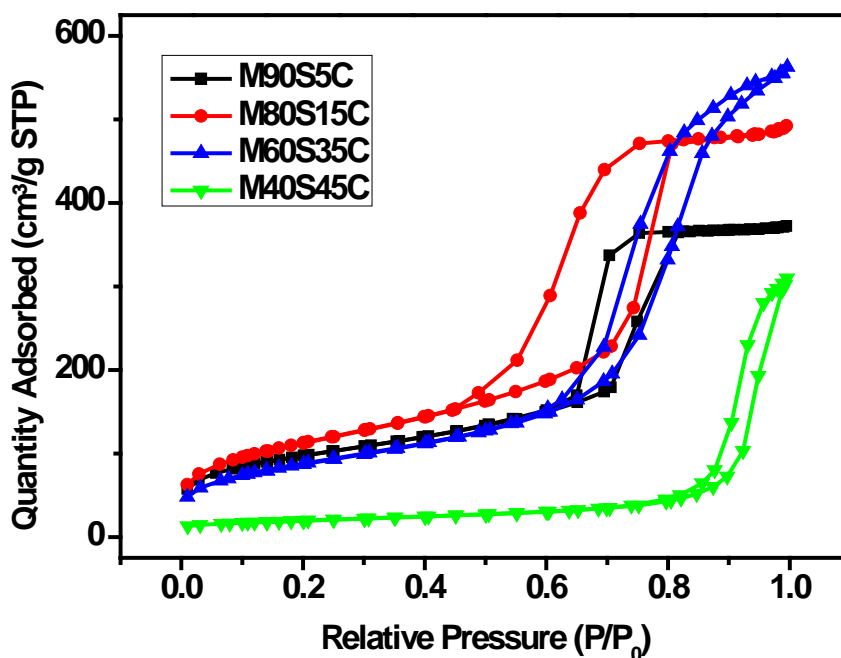
Figure 5.2 Nitrogen adsorption-desorption isotherms of MBG of different silica compositions: M40S45C, M60S35C, M80S15C and M90S5C.

Fig 5.3 plots the pore size distribution curve of MBG of different silica compositions. All the samples presented a single modal pore size distribution. MBG samples of higher silica compositions (i.e. M90S5C and M80S15C) had a sharper and defined pore size distribution centered around 77 Å and 90 Å, respectively. M60S35C displayed a bimodal peaks at 91 Å and 109 Å, while M40S45C showed a broader pore size distribution between 200 and 500 Å. Hence, the average pore size distribution increased and broadened as the silica content decreased. The increase in pore size could result in a decrease in surface area [160, 161]. Similarly, Pérez-Pariente et al. [170] who studied the SiO_2–CaO–P_2O_5–MgO system had demonstrated that glasses with higher silica composition showed higher surface area and smaller pore diameter.
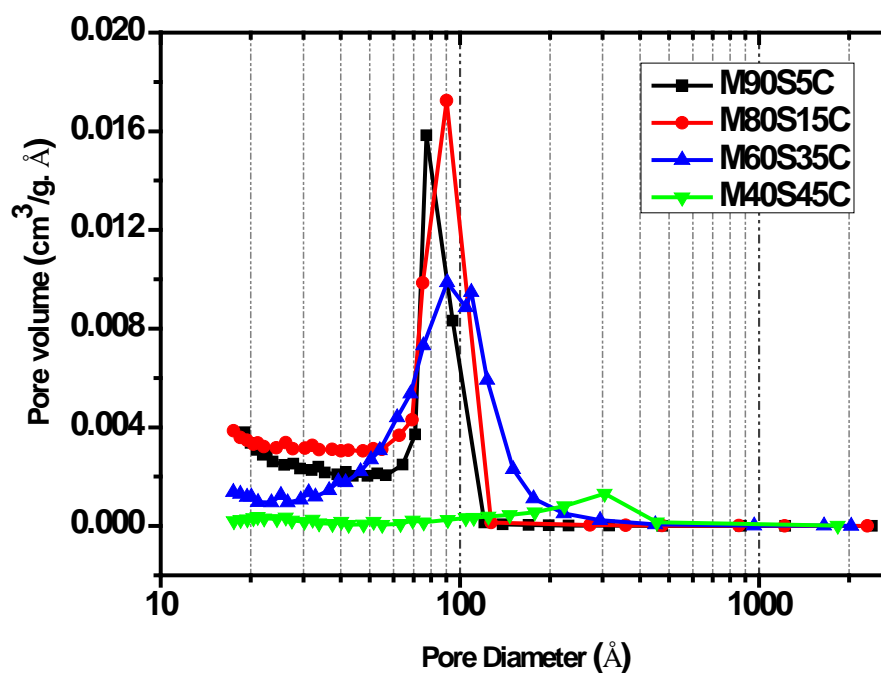
Figure 5.3 BJH pore size distribution of MBG of varying silica compositions: M40S45C, M60S35C, M80S15C and M90S5C.

Fig.5.4 shows the X-ray diffraction (XRD) patterns of MBG of different compositions calcined at 600 °C for 5 h. The study confirmed that MBG exist in the amorphous state with a broadened peak between 15° and 40° 2θ. It was observed that the broad peak shifted to a lower 2θ position at around 30 ° and its intensity increased with decreasing silica content. This indicated the presence of the amorphous calcium silicate component [171] in MBG samples.
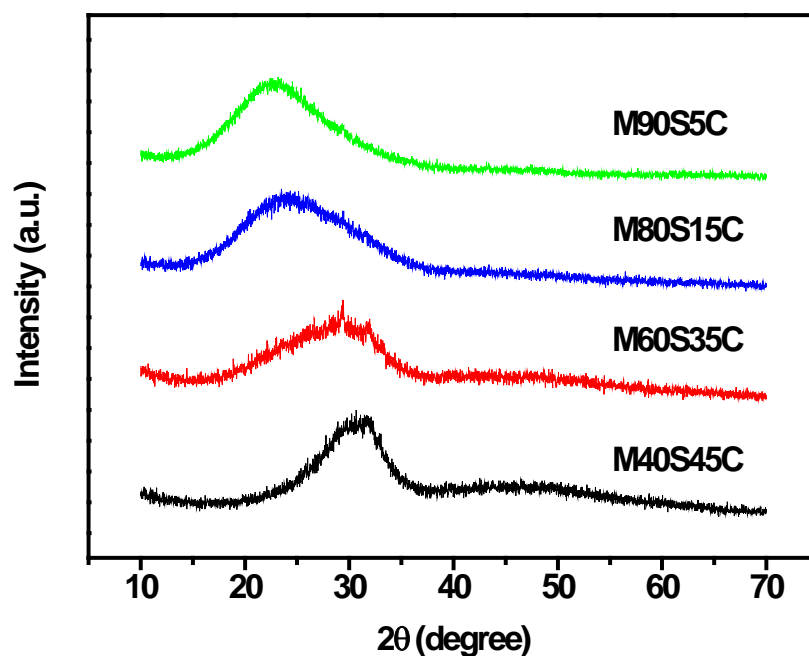
Figure 5.4 X-ray diffraction (XRD) patterns of MBG of varying silica compositions: M40S45C, M60S35C, M80S15C and M90S5C.

The FTIR spectra of the MBG of varying silica content were collected in the range of 400 – 4000 cm^{-1} as presented in Fig 5.5. All the spectra showed characteristic bands of Si-O bending and stretching vibration at 1075-1000 cm^{-1}, 800-770 cm^{-1} and 515-460 cm^{-1}. The absorptions decreased in intensity with increasing silica content. The bands from 1295 cm^{-1} to 1500 cm^{-1} and from 2800 cm^{-1} to 3000 cm^{-1} were assigned to the bending and stretching vibrations of ─CH_2─ in polyethylene oxide (PEO) in the Pluronic F127 surfactant. Such vibrations became almost undetectable at higher silica composition. The band between 3400 and 3600 cm^{-1} was due to the stretching vibration of O-H group which was associated with the adsorbed water.
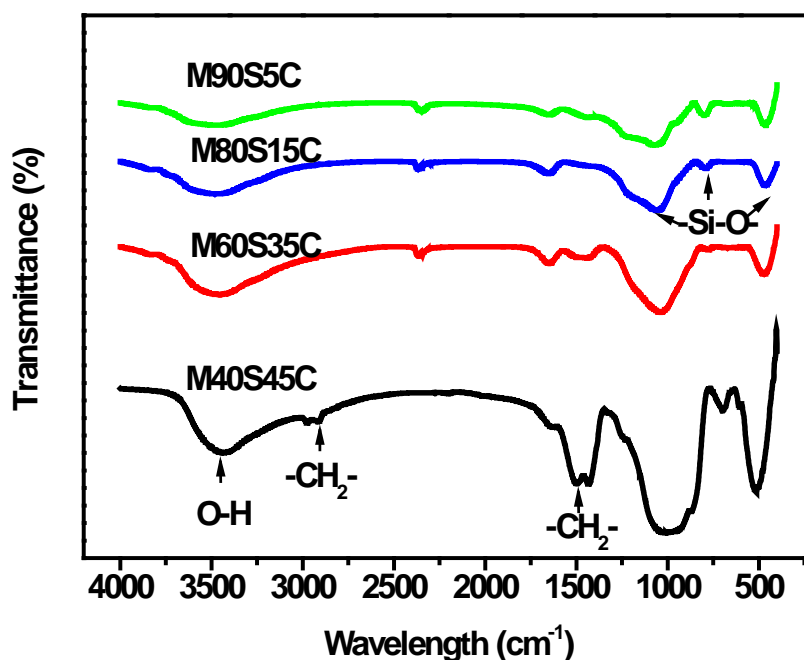
Figure 5.5 FTIR spectra of MBG of different silica compositions: M40S45C, M60S35C, M80S15C and M90S5C.

5.2 Calcination temperature

Calcination is usually performed for surfactant removal, leaving behind the desired mesostructure. Yan et al. [50] and Shih et al. [172] had both reported that calcination temperature had made a great impact on the textural properties of mesoporous bioglasses. Hence, the influence of calcination temperature on the synthesized MBG90S5C was investigated. The dried gel was calcined between 400 and 600 °C for various dwell/duration times (5 h, 12 h and 24 h). As shown in Fig. 5.6, the BET surface area of the M90S5C decreased with increasing calcination temperature at constant duration time. In addition, the average pore volume of M90S5C (not shown) decreased 15 %, 46 % and 29 % when the calcination temperature was raised from 400 to 600 °C for a dwell time of 5 h, 12 h and 24 h,

respectively. Hence, it was clear that the pore volume of M90S5C decreased with increasing calcination temperature. At lower calcination temperature but above surfactant decomposition temperature (i.e. 400 °C), the mesoporous structure remained intact and prohibited the crystal growth, resulting in a higher BET surface area [169]. When the calcination temperature was further increased, the pores started to collapse gradually and the crystallite was able to grow at a lower degree of suppression by the mesopores. Hence, the BET surface area would decrease with increasing calcination temperature.
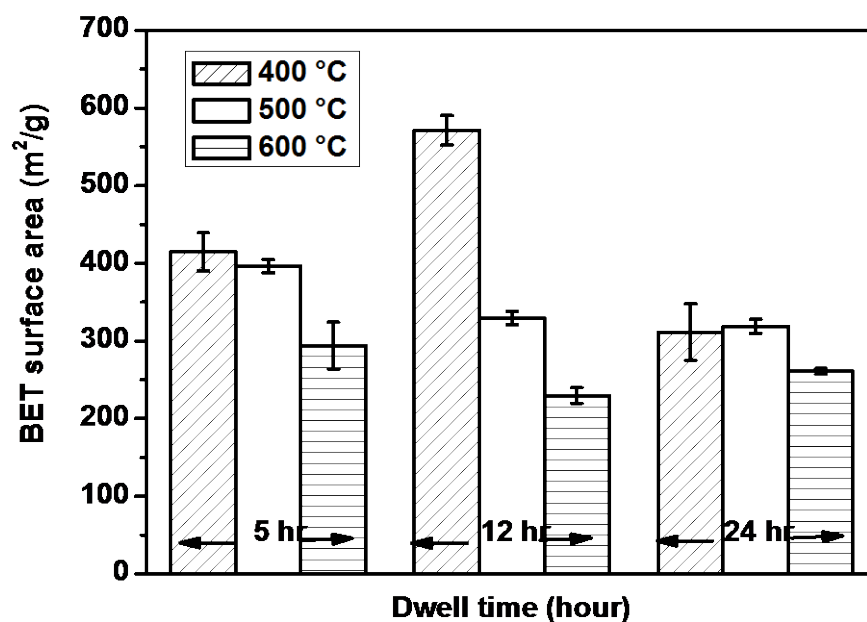
Figure 5.6 BET surface area comparison of M90S5C on calcination temperature of 400 °C, 500 °C & 600 °C and calcination dwell time of 5 h, 12 h &24 h.

The nitrogen adsorption-desorption isotherm of M90S5C calcined at varying temperatures for 5 h is illustrated in Fig. 5.7. All the curves exhibited type IV isotherm together with H1 type hysteresis loops [50, 130] in the almost identical P/P_0 at 0.4. The sharp pore-filling curve of M90S5C corresponded to a narrow pore size distribution. The slope of the curve

after the low pressure adsorption was found to increase with decreasing calcination temperature, corresponding to a higher mesopore area of M90S5C. In addition, their pore volume which was measured at the top of the mesopore filling step was higher at a lower calcination temperature, indicating the silica walls of lower temperature calcined M90S5C were thinner. The inset of Fig.5.7 confirms that the pore size distribution were quite uniform for all the M90S5C of different calcination temperatures The pore diameters for M90S5C calcined for 5h at 400, 500 and 600 °C were 65 Å, 63 Å and 68 Å, respectively.
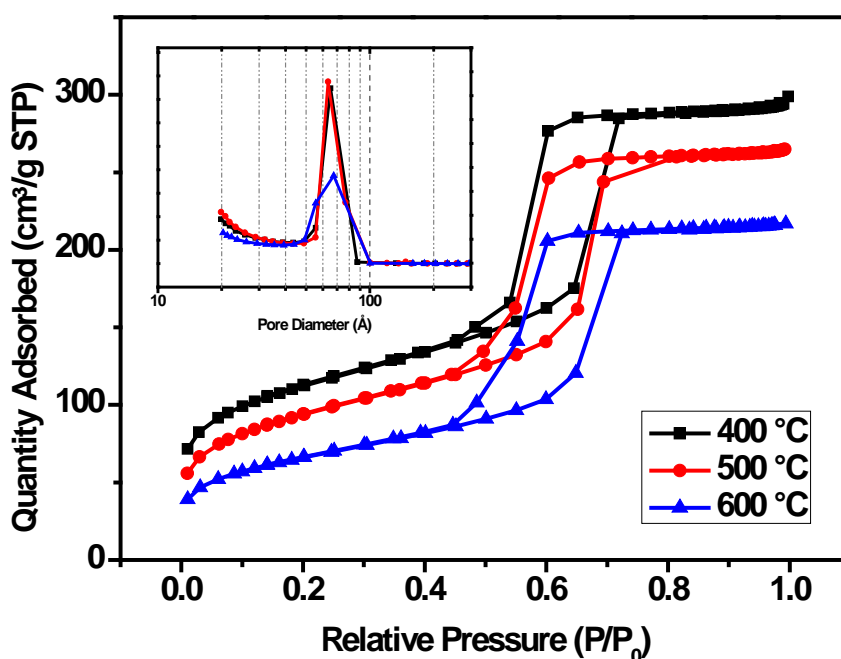
Figure 5.7 Nitrogen adsorption-desorption isotherms of M90S5C calcined at different temperatures for 5 h and its BJH pore size distribution (inset).

To further understand the phase and crystallographic structure of M90S5C, X-ray diffraction (XRD) was conducted. Fig. 5.8 shows the XRD patterns of M90S5C calcined at different temperatures for 5 h. A broad peak between 2θ range of 15 °and 40 ° were found on all the M90S5C samples studied, confirming the amorphous phase of these calcined glasses. When

the calcination temperature was further increased (> 600 ℃), the crystallization of the inorganic substances may lead to the collapse of the mesostructure of glasses which would result in low BET surface area [50, 172]. Nevertheless, a second small peak was found at $2\theta \approx 30°$ with decreasing calcination temperature, indicating the presence of amorphous calcium silicate phase [50] in M90S5C at low calcination temperature.

In addition, the FTIR spectra (not shown) at varying calcination temperature had a similar absorption peaks analogous to the spectra shown in Fig. 5.5, where the stretching and bending mode of Si-O-Si were at 1075-1000 cm^{-1}, 800-770 cm^{-1} and 515-460 cm^{-1}. However, no ─CH$_2$─ vibration due to the presence of PEO in F127 surfactant was observed. Hence, the surfactant in M90S5C was confirmed to be completely removed after calcination. The O-H stretching vibration was assigned to 3400 and 3600 cm^{-1} absorption.
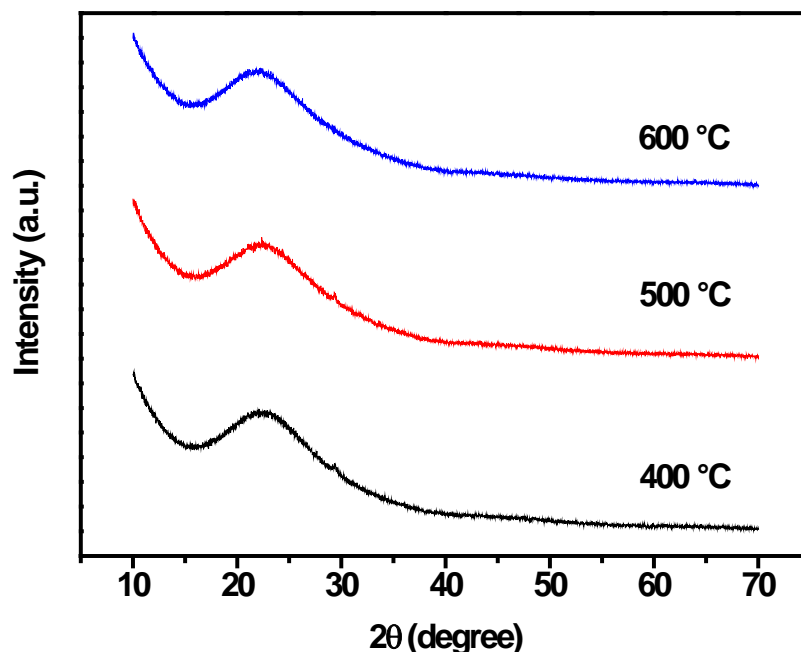
Figure 5.8 X-ray diffraction (XRD) patterns of M90S5C calcined at 400 ℃, 500 ℃ and 600 ℃ for 5 h.

5.3 Calcination dwell/ duration time

The effect of the calcination dwell time on the BET surface area of M90S5C was studied. Fig. 5.6 shows the BET surface area of M90S5C samples calcined at varying dwell time. At higher calcination temperature (i.e. 500 and 600 °C), a shorter duration time of calcination (i.e. 5 h) was favorable to achieve high BET surface area. When the dwell time of calcination was lengthen to 12 and 24 h, the value of BET surface area of M90S5C decreased and remained constant subsequently. On the contrary, when the M90S5C samples were calcined at 400 °C, higher BET surface area was presented in 12 h of calcination dwell time.

These findings could be correlated to the physical properties of surfactant F127. Since the decomposition temperature of F127 is around 300 - 400 °C, the surfactant molecules were confirmed to be totally removed at higher calcination temperature. However, when the M90S5C sample was calcined at 400 °C, a longer dwell time was required to thoroughly remove the surfactant molecules which might remain inside the structure. In this study, the optimum dwell time for 400°C calcined M90S5C samples was kept at 12 h. Similar to the high temperature calcined M90S5C which decreased with increasing calcination duration time, M90S5C calcined at 400 °C experienced a decrease in BET surface area from 12 h to 24 h dwell time. The outcome was supported by Shih et al. [172] in which they observed that the BET surface area initially decreased with increasing dwell time but remained reasonably constant afterwards. It was believed that the crystal growth rate differed with varying calcination temperature. At lower calcination temperature, the mesoporous structure remained stable and the crystal growth was prohibited, hence a longer calcination dwell time was allowed to achieve high BET surface area. On the contrary, a shorter dwell time was

enough to promote crystal growth at higher calcination temperature, resulting in a lower BET surface area with increasing calcination dwell time.

Besides that, the nitrogen adsorption-desorption isotherms of M90S5C calcined at 400°C for different dwell times are demonstrated in Fig. 5.9. All the curves studied exhibited type IV isotherm and H1 type hysteresis loops [50, 130] in the P/P_0 between 0.4 and 0.6. The isotherm of M90S5C calcined at 400 °C for 12 h after the low pressure adsorption was the steepest, hence resulting in a higher BET surface area. The defined pore-filling curve of the isotherm related to a narrow pore size distribution. This had been proven and is shown in the inset of Fig.5.9. The pore diameters for M90S5C calcined at 400°C for 5 h, 12 h and 24 h were 65 Å, 85 Å and 77 Å, respectively. The pore size of M90S5C which calcined for 12 h was comparatively larger. This was related to the isotherm of which the pore volume adsorbed (y-axis) at the top of the mesopore filling step was higher, indicating a thinner silica wall and therefore larger pores.
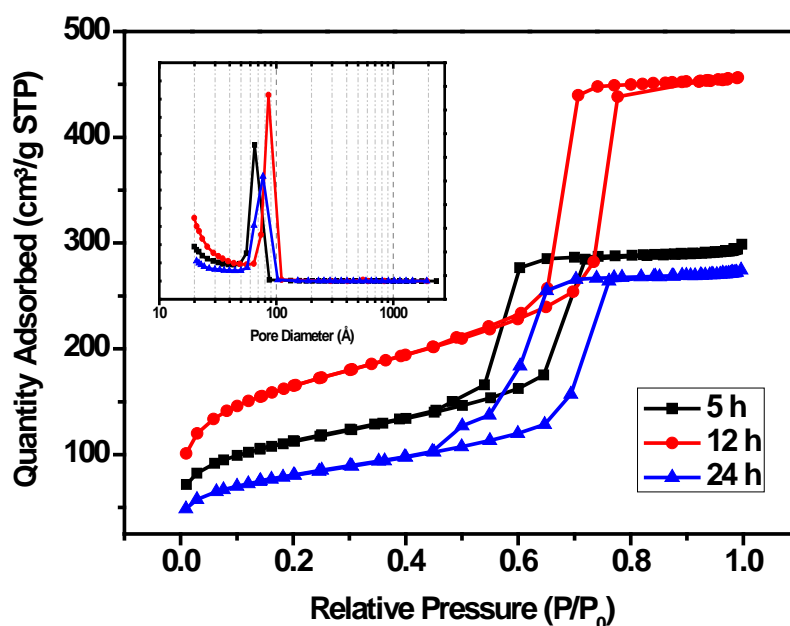
Figure 5.9 Nitrogen adsorption-desorption isotherms of M90S5C calcined at 400 °C for various calcination dwell time of 5 h, 12 h and 24 h.

Fig. 5.10 plots the X-ray diffraction (XRD) pattern of the M90S5C samples calcined at 400°C for 5 h, 12 h and 24 h. Similarly, a broadened peak between 2θ range of 15 °and 40 ° were found on all the samples studied, confirming the amorphous phase of these calcined glasses. In addition, a second small peak at 2θ ≈ 30° was observed especially in calcination dwell time of 12 h and 24 h, indicating the presence of amorphous calcium silicate phase [50] for longer treatment time of calcination.
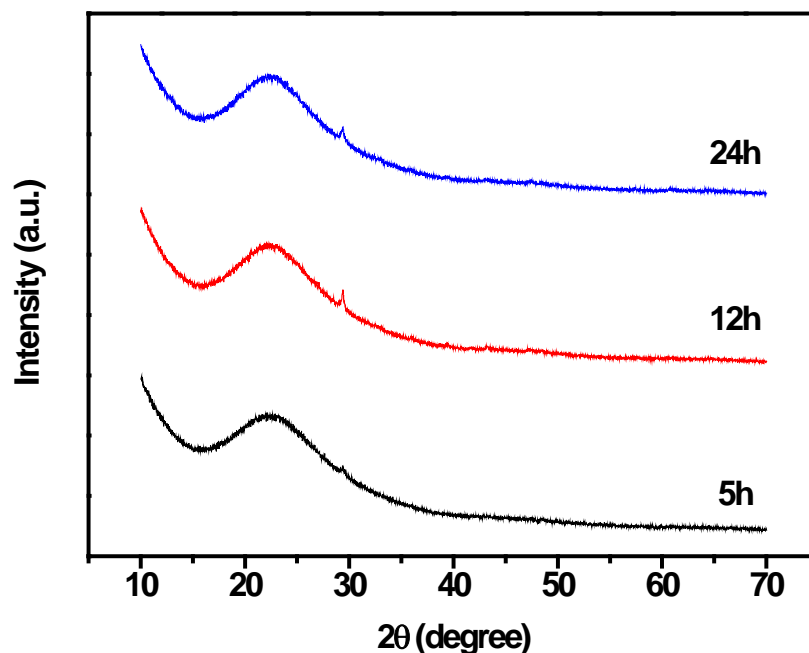
Figure 5.10 X-ray diffraction (XRD) patterns of M90S5C calcined at 400 •C for calcination dwell time of 5 h, 12 h and 24 h.

The chemical and structural composition of M90S5C samples were analyzed using FTIR. Fig. 5.11 plots the FTIR spectra of the M90S5C calcined at 400 °C for different duration time between 5 h and 24 h. The bands at 1075-1000 cm^{-1}, 800-770 cm^{-1} and 515-460 cm^{-1} referred to the Si-O bending and stretching vibration. It was observed that the intensity of the

absorption bands increased with increasing dwell time. On the other hand, the absorption between 3400 and 3600 cm^{-1} was due to the stretching vibration of O-H group which was associated with the adsorbed water.
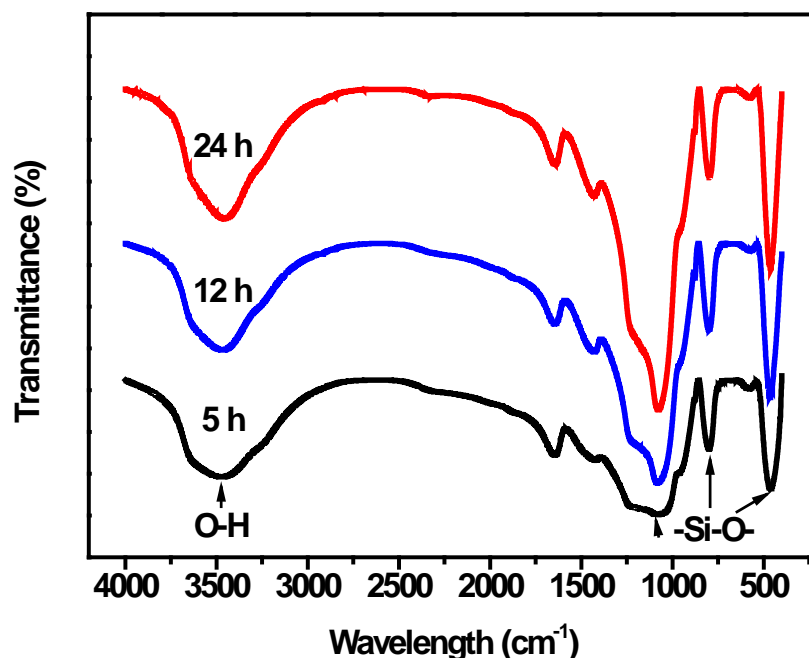
Figure 5.11 FTIR spectra of M90S5C calcined at 400 °C for calcination dwell time of 5 h, 12 h and 24 h.

5.4 Synthesis temperature

Similar to mesoporous calcium phosphates (MCP), in order to investigate the effect of synthesis temperature on the MBG samples, experiment was carried out under different temperatures. Since the synthesis solvent was ethanol of boiling point at ≈ 78.5 °C, the temperatures studied were kept below this point (i.e. RT, 40 and 60 °C). The M90S5C samples calcined at 400 °C for 12 h with three different synthesis temperatures were shown in Table 5.1. The BET surface area of the M90S5C samples remained relatively stable with

increasing synthesis temperatures. In terms of pore volumes and pore diameters, there was a decreasing trend observed with increasing synthesis temperatures.

Table 5.1 Textural properties of M90S5C synthesized at RT, 40 °C and 60 °C and calcined at 400 °C for 12 h.

Sample	BET surface area (m²/g)	BJH adsorption pore volume (cm³/g)	BJH adsorption pore diameter (nm)
M90S - RT	571 ± 19	0.63 ± 0.02	6.10 ± 0.17
M90S - 40	533 ± 9	0.58 ± 0.05	5.87 ± 0.17
M90S - 60	537 ± 31	0.52 ± 0.003	5.52 ± 0.03

BET, Barrett-Emmett-Teller; BJH, Barrett-Joyner-Halanda, M90S, mesoporous bioglass M90S5C

The nitrogen adsorption-desorption isotherm of M90S5C synthesized at different temperatures is demonstrated in Fig. 5.12. All the curves exhibited type IV isotherm with H1 type hysteresis loops [50, 130] in the P/P_0 between 0.4 and 0.6. The slopes for all the isotherms after the low pressure adsorption were similar, corresponding to a similar BET surface area of M90S5C samples treated at different synthesis temperatures. Besides that, the pore volume as calculated at the top of the mesopore filling step was higher at low synthesis temperature, indicating the silica walls of M90S5C-RT were thinner than the other two samples. Thinner silica wall would lead to a larger pore size which was in good agreement with the result as shown in Table 5.1.
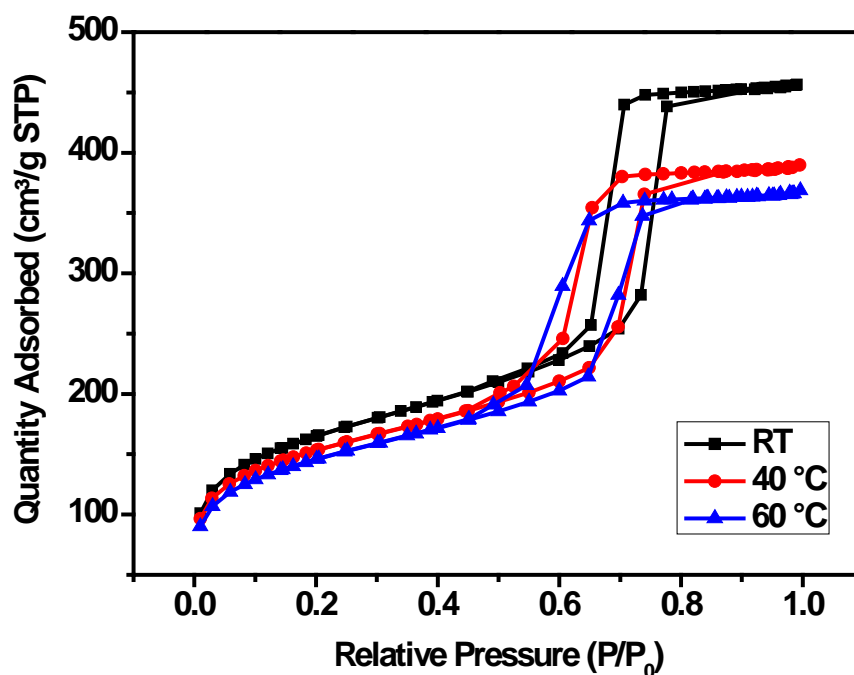
Figure 5.12 Nitrogen adsorption-desorption isotherms of M90S5C synthesized at RT (25 ºC), 40 ºC, 60 ºC and calcined at 400 ºC for 12h.

Fig. 5.13 depicts the X-ray diffraction (XRD) pattern of the M90S5C samples with varying synthesis temperatures calcined at 400°C for 12 h. A broadened peak between 2θ range of 15 °and 40 ° were found on M90S5C synthesized at different temperatures, confirming that all these calcined glasses were amorphous. Similarly, a second small peak at 2θ ≈ 30° was shown in room temperature (RT), 40 °C and 60 °C. The small peak signified the presence of the amorphous calcium silicate in M90S5C. Meanwhile, the FTIR spectra (not shown) of varying synthesis temperatures showed the main characteristic bands of M90S5C in which the stretching and bending mode of Si-O-Si were at 1075-1000 cm^{-1}, 800-770 cm^{-1} and 515-460 cm^{-1}.
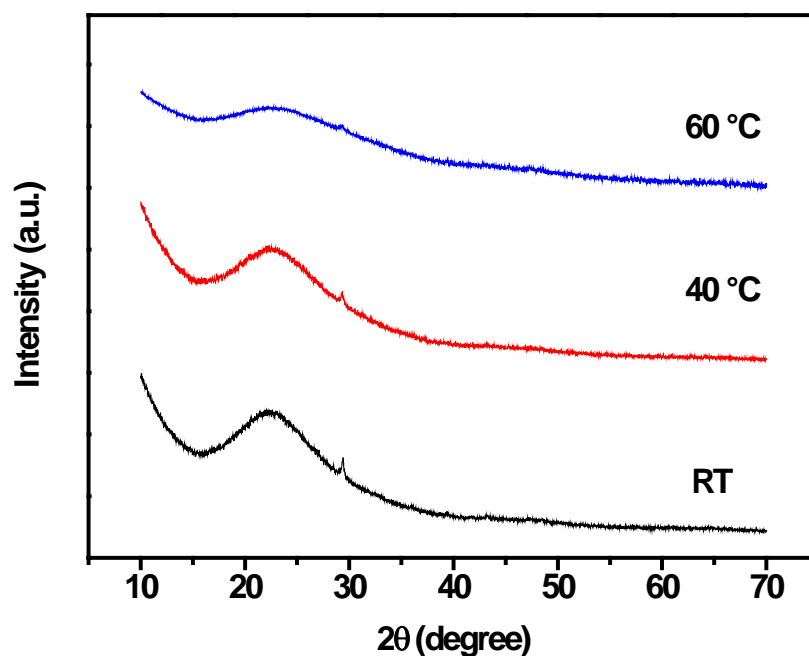
Figure 5.13 X-ray diffraction (XRD) patterns of M90S5C synthesized at RT (25 ºC), 40 ºC, 60 ºC and calcined at 400 ºC for 12h.

5.5 Summary

Mesoporous bioactive glasses (MBG) with different composition, calcination temperature, calcination dwell time and synthesis temperature had been synthesized by surfactant templating, followed by sol-gel and lastly evaporation-induced self-assembly (EISA) process at 50 °C.

In terms of textural properties of MBG, the BET surface area increased with (a) increasing silica composition and (b) decreasing calcination temperature. The calcination duration time was dependent on the calcination temperature of MBG. For M90S5C calcined at 400 °C, the BET surface area was the highest at 12 h dwell time. While for M90S5C calcined above

400 °C, the BET surface area was higher at lower dwell time (i.e. 5 h). In addition, the BET surface area remained fairly constant with increasing synthesis temperature (i.e. RT, 40 °C and 60 °C). All the MBG samples studied had small pore sizes and narrow pore size distribution except MBG40S45C which had a low BET surface area of 71 m^2/g and large BJH pore diameter of 26 nm. The pore volume of MBG was affected by the calcination temperature and synthesis temperature. The pore volume of M90S5C increased with decreasing calcination and synthesis temperature. All the nitrogen adsorption-desorption curve of MBG exhibited type IV isotherm with H1 type hysteresis loops, according to IUPAC classification.

The phase and crystallographic structure of MBG was discussed using X-ray diffraction (XRD) pattern which scanned between 10 ° and 70 ° 2θ. All the MBG samples studied were confirmed to be amorphous with a broad peak observed between 15 ° and 40 ° 2θ. A minor phase of amorphous calcium silicate was detected at $2\theta \approx 30°$ at lower silica composition, synthesis temperature and calcination temperature for all duration time. On the other hand, the FTIR analysis of the MBG samples synthesized showed main characteristic absorption bands of Si-O bending and stretching vibration at 1075-1000 cm^{-1}, 800-770 cm^{-1} and 515-460 cm^{-1}. Additional $-CH_2-$ vibrations which was due to the presence of PEO in F127 surfactant was noticed at low silica composition.

In conclusion, high BET surface area of 571 ± 19 m^2/g, pore volume of 0.63 ± 0.02 cm^3/g and pore diameter of 6.10 ± 0.17 nm (Table 5.1) was achieved in M90S5C -RT samples calcined at 400 °C for 12 h. This product would be studied on the following chapters of protein adsorption and release.

CHAPTER 6

6 *PROTEIN STUDIES OF MESOSTRUCTURED CALCIUM PHOSPHATES (MCP) AND MESOPOROUS BIOACTIVE GLASSES (MBG)*

Having rigorously characterized the properties of mesoporous calcium phosphates (MCP) and mesostructured bioactive glasses (MBG), the next phase of the study would focus on the protein adsorption and release of MCP and MBG in solid form. The control sample would be the commercial calcium phosphate (CP).

6.1 Mesostructured calcium phosphates (MCP) and mesoporous bioactive glasses (MBG) for protein adsorption

It is important for materials to have a high protein loading capacity in order to achieve controlled release kinetics [104]. Usually, the incorporation of proteins or drugs into carriers through physical adsorption has a low efficiency of loading. High surface area mesostructured materials were able to host more proteins into its nanoscale pores, thus it is hypothesized that they would enhance protein loading efficiency. However, up to date, there was no report on the incorporation of protein into MCP and MBG powder materials.

Hence, it was of our interest to study the protein loading profile. The MCP and MBG chosen had the highest BET surface area and pore volume after optimization as shown in Table. 6.1. Besides that, the secondary electron images (SEI) of the three samples are illustrated in Fig.

6.1. The particle morphology of commercial calcium phosphate (CP) exhibited rod-like crystals of uniform size of 70 – 80 nm. MCP synthesized at room temperature was of irregular flake-like structure of size ranged between 60 – 100 nm with some agglomeration. The MBG synthesized also had an amorphous structure.

Table 6.1 Textural properties of commercial CP (control), synthesized MCP and MBG.

Sample	BET surface area (m^2/g)	BJH adsorption pore volume (cm^3/g)	BJH adsorption pore diameter (nm)
CP	28 ± 2.5	0.21 ± 0.01	nil
MCP	263 ± 36	0.96 ± 0.14	13.54 ± 3.52
MBG	571 ± 19	0.63 ± 0.02	6.10 ± 0.17

Bovine serum albumin (BSA) and Lysozyme (LSZ) were employed as model proteins in the evaluation of mesostructured materials. BSA and LSZ are proteins of different surface charge and structural stability. As shown in Table. 2.2, BSA, a 69 kDa acidic protein with low isoelectric point (pI = 4.7), is a negatively charged protein, while LSZ (Mw 14.6 kDa, pI 11.1, basic protein) is a model positively charged protein. The pI is the pH value in solution at which the sum of the charges on the protein is zero.
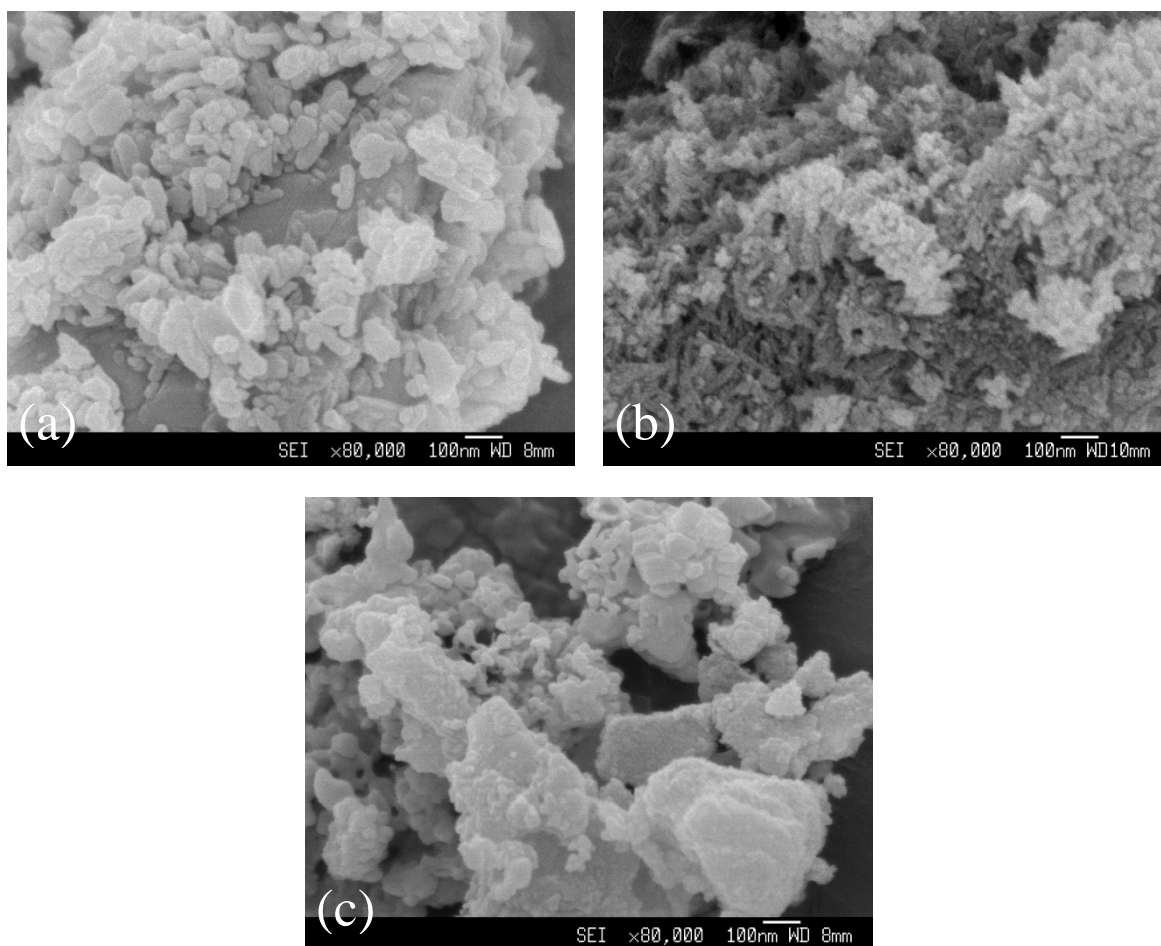
Figure 6.1 Field emission scanning electron images (SEI) of (a) commercial CP (control), (b) MCP and (c) MBG, magnification = 80K.

6.2 Protein loading study

6.2.1 UV-Vis assessment on protein adsorption

A predetermined amount of inorganic powders (CP, MCP or MBG) was added into 1 mg/ml of protein solution separately to evaluate the protein loading efficiency. The UV-Vis assessment was carried out after 24 hours of loading (RT, aqueous solution). Fig. 6.2 plots the loading capabilities of three LSZ–loaded samples, with respect to the LSZ-CP (control, ≈ 8.6 µg LSZ molecules stored per mg of CP) which represented the protein loaded nonporous

inorganic samples. It was shown that LSZ-CP exhibited the lowest adsorption, while the adsorptions of LSZ by MCP and MBG were 75 % and 475 % higher than the control, respectively. In the evaluation on BSA adsorption, the loading efficiency of BSA into MBG was 65 % lower than the control (BSA-CP) as demonstrated in Fig. 6.3. In contrast, the amount of BSA adsorbed by MCP was 3.2 times greater than CP ($\approx$ 59.8 µg/mg BSA adsorbed by CP). Another remarkable result was that MBG was adsorbed by the highest amount of LSZ but the lowest amount of BSA across the three samples. Overall for LSZ adsorption, the amount of protein loaded into inorganic materials arranged in ascending order was CP < MCP < MBG. For BSA adsorption, the amount of protein adsorbed was MBG < CP < MCP in ascending order.
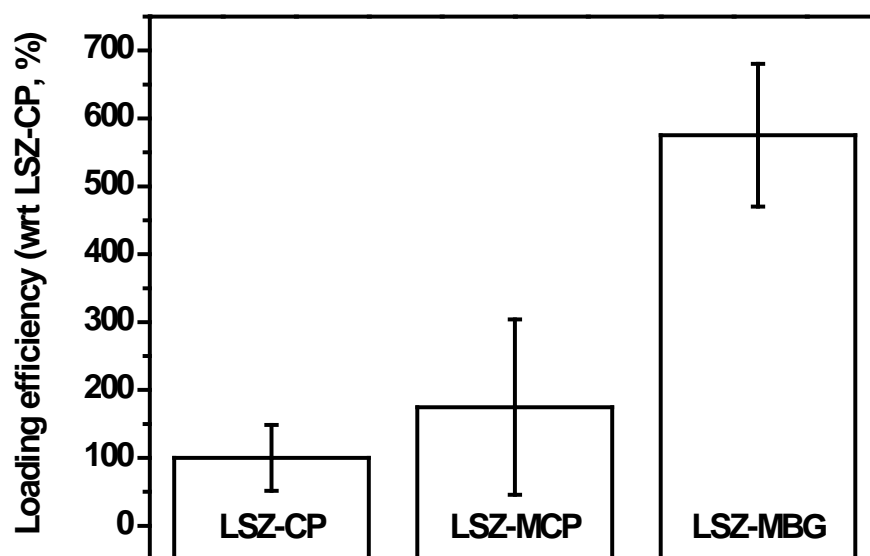
Figure 6.2 Percentage loading efficiency of Lysozyme (LSZ)-loaded CP, MCP and MBG with respect to LSZ-CP.
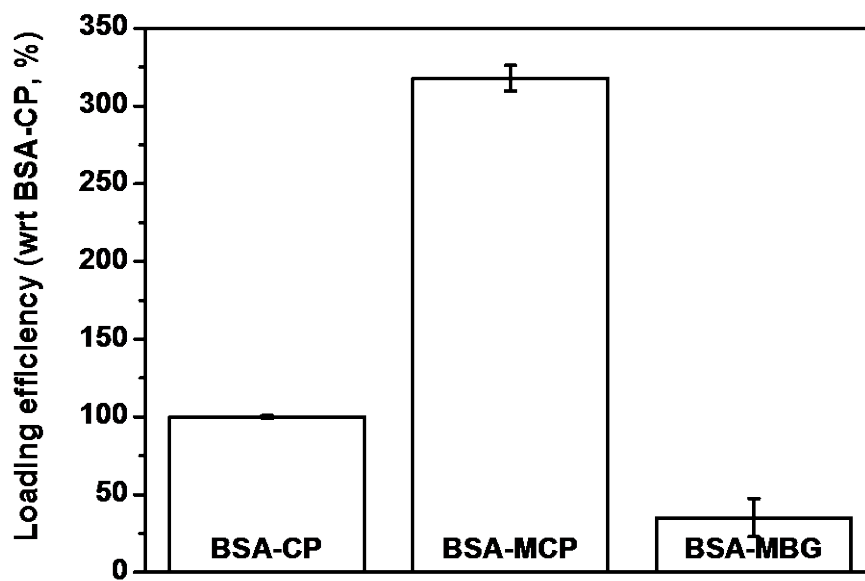
Figure 6.3 Percentage loading efficiency of Bovine serum albumin (BSA)-loaded CP, MCP and MBG with respect to BSA-CP.

The trend in the LSZ loading capacity of the samples could be attributed to the high surface area [104] of mesoporous structure compared to the nonporous CP (Table. 6.1). The loading efficiency of LSZ-MBG was around 3.3 times higher than LSZ-MCP since the higher surface area of MBG favored a comparable large amount of LSZ molecules into their mesopore. Besides surface area, the high pore volume also permits to host a larger amount of protein molecule. This characteristic was also true in the efficiency of BSA adsorption since MCP has a pore volume as high as 0.96 ± 0.14 cm^3/g, which in turn resulted in a higher BSA loading as compared to BSA-MBG.

In addition, it was shown that higher adsorption capacity was found on BSA compared to LSZ in calcium phosphate materials (both nonporous and mesoporous). The dimensions of LSZ, which are about $3 \times 3 \times 4.5$ nm^3, are much smaller than BSA, which is a larger protein

with dimensions $4 \times 4 \times 14$ nm^3 (Table. 2.2). Looking at the pore diameter of MCP which was around 13.5 nm (Table. 6.1), the pores would have a better accessibility for efficient BSA loading. On top of that, the conformational stability of both proteins affected the loading efficiency in these inorganic materials as well [96, 111, 112].

BSA (bovine serum albumin) loaded mesostructured calcium phosphate (MCP) nanoparticles had shown to achieve ~ 95% of loading efficiency (Table 6.2). Comparing to the commercial calcium phosphate (CP), the loading was > 3 times higher in MCP. Besides, the loading efficiency of MCP is relatively higher as compared to polymeric [173] and solid lipid nanoparticles [174]. This could be attributed to the mesoporous structure of the MCP in housing higher amount of proteins.

Table 6.2 Protein loading efficiency comparison between MCP nanoparticles and other nanoparticles

Protein loaded nanoparticles	Loading efficiency (%)
BSA - MCP	95.00 $\pm$ 2.47
BSA - CP	29.88 $\pm$ 0.27
G-CSF-PLGA nanoparticles [173]	37.8
Catalase-Solid Lipid Nanoparticles [174]	53.9 $\pm$ 1.85

BSA – Bovine Serum Albumin; G-CSF - recombinant human granulocyte colony-stimulating factor

Note: All loading efficiencies are calculated through the same technique.

Fig. 6.4a displays the UV absorbance spectra of protein LSZ before (control) and after 24 h loading into CP, MCP and MBG over the wavelength range 250-300 nm. It was shown that there was no significant peak shift of LSZ with various inorganic materials. This indicated that there was no sign of degradation and the tertiary structure of LSZ was retained [99] after loading. The UV spectra of the adsorption of BSA (Fig. 6.4b) onto CP and MBG were similar to the BSA spectrum before loading (control). In contrast, no peak was found in the UV spectrum of BSA-MCP due to the high adsorption of BSA onto MCP after 24 h ($\approx 95 \pm 2.5$ % adsorption), resulting in a very low concentration of BSA left in the solution after loading. The intensity decreased in UV absorbance after loading reflected the reduction of the protein concentration in solution. As a result, the protein molecules had been stored into the mesostructured materials and control.
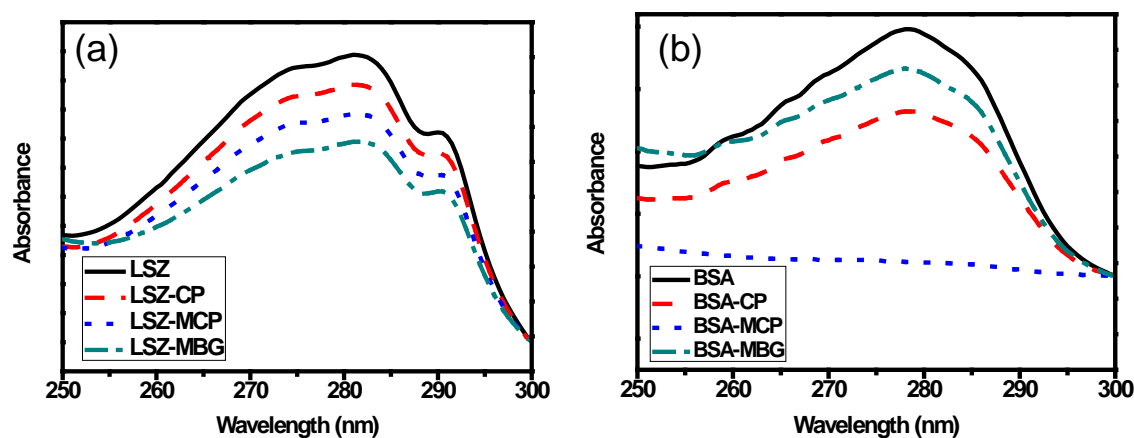
Figure 6.4 UV absorbance spectra of (a) LSZ and (b) BSA loaded CP, MCP and MBG with respect to proteins before loading (control).

6.2.2 FTIR analysis

The presence of amide bands of protein after adsorption [85] was discussed using FTIR analysis. The amide I band near 1650 cm^{-1} was due to the stretching of C=O. The amide II band near 1520 cm^{-1} referred to the bending and stretching vibration of N—H and C—N. Fig. 6.5 shows the FTIR spectra of the mesostructured materials before and after protein loading in comparison to the pure protein LSZ and BSA. For protein LSZ (Fig. 6.5a-c) the amide I and amide II bands was found at 1653 cm^{-1} and 1537 cm^{-1}, respectively. While for protein BSA (Fig. 6.5d-f), the amide I and amide II bands were centered at 1657 cm^{-1} and 1541 cm^{-1}, respectively. The strong amide I bands represent the α-helical structure of protein. At the same time, the strong amide II bands contributed to the parallel β-sheet conformation of protein [175].

For all the samples loaded protein studied, amide I bands were identified between 1650 and 1660 cm^{-1}. Across all the samples loaded with proteins, the FTIR spectrum of BSA-MBG in particular, had a rather low intensity of amide II band than the other samples. It might be due to the lower loading efficiency of BSA as the intensities of all the bands would increase with increasing loading [85]. Besides that, the two bands between 1380 and 1480 cm^{-1} were assigned to the stretching of —CH$_2$— and —CH$_3$ in the aliphatic moieties of amino acid side chains.
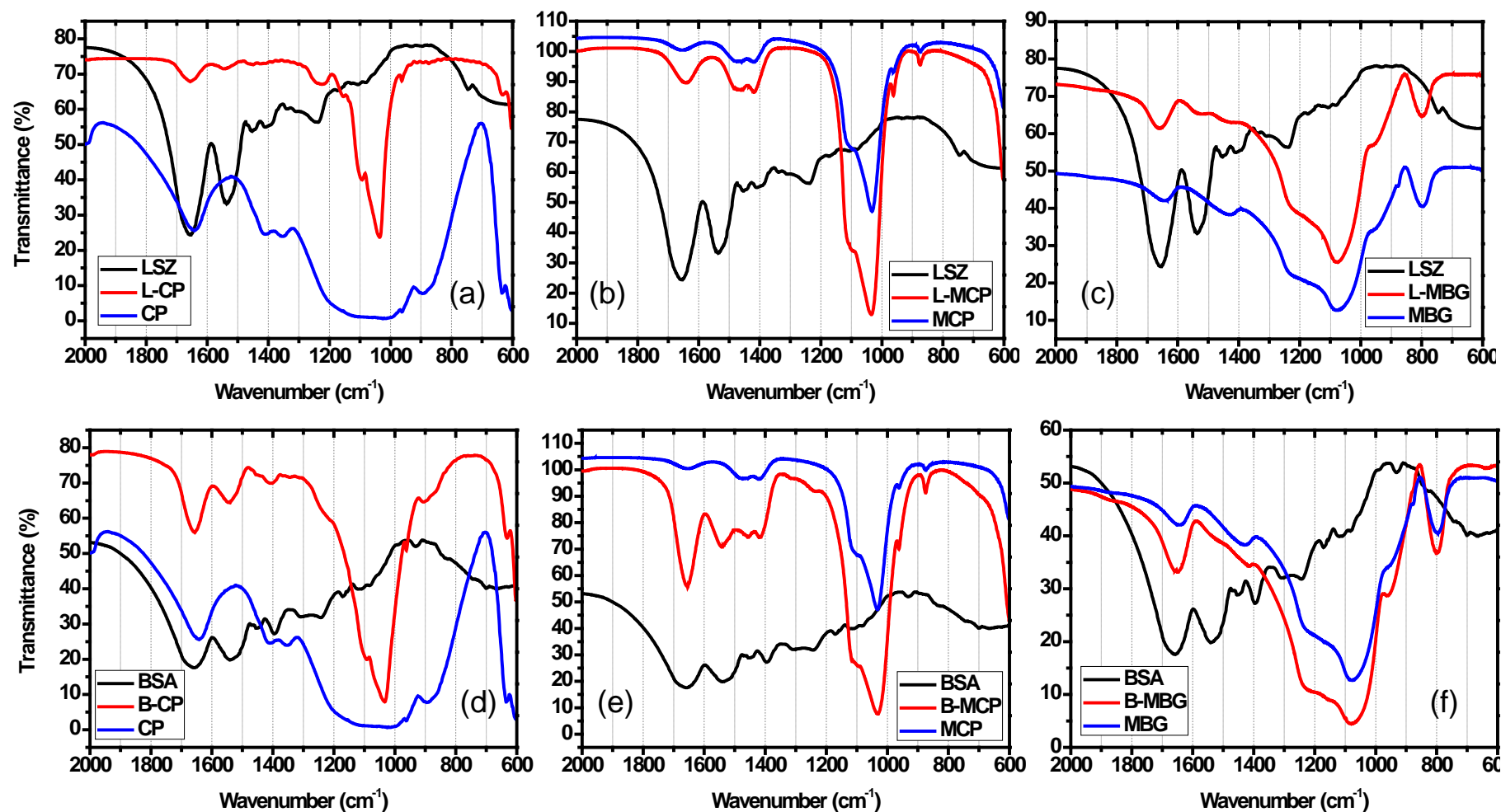
Figure 6.5 FTIR spectra of Lysozyme (LSZ)-loaded (a) CP, (b) MCP, (c) MBG and Bovine serum albumin (BSA)-loaded (d) CP, (e) MCP and (f) MB, with respect to their pure protein and inorganic materials.

6.2.3 TGA

The presence of protein in a material could be determined by thermogravimetric analysis (TGA) measurement. Fig. 6.6a illustrates the thermograms of protein BSA (black line) and LSZ (red line). Both thermograms were divided into three regions. The initial 10 % weight loss (region I) of both proteins due to the desorption of adsorbed water was shown between room temperature and 200 °C. Following that, a major weight loss of protein occurred in region II between 200 °C and 450 °C (50 %), which was similar to those reported [176]. For LSZ, the weight loss in region II was between 200 °C and 400 °C (40 %). The weight loss of BSA and LSZ in region III up to 800 °C would be 40 % and 50 %, respectively. The weight loss in region II and III contributed to the degradation of protein in air.

Fig. 6.6b shows the thermogram of commercial calcium phosphate (CP) having a weight loss of around 5 % and maintained the thermal stability up to 800 °C. The TGA curve of BSA-CP showed a greater percentage weight loss (8.5 % combining region II and III) than LSZ-CP (4 % loss). The remaining residue from the curve contributed to the highly stable inorganic material CP. Both the thermograms of synthesized MCP (Fig. 6.6c) and MBG (Fig. 6.6d) showed approximately 12 % weight loss due to the loss of adsorbed water at the temperature range of 25-400 °C. There was no further weight loss on heating up to 800 °C, showing the stability of these two mesostructured materials. With respect to the pure bioceramics samples, all the proteins (both LSZ and BSA) were successfully loaded into the respective samples as shown in Fig. 6.6b, c and d.
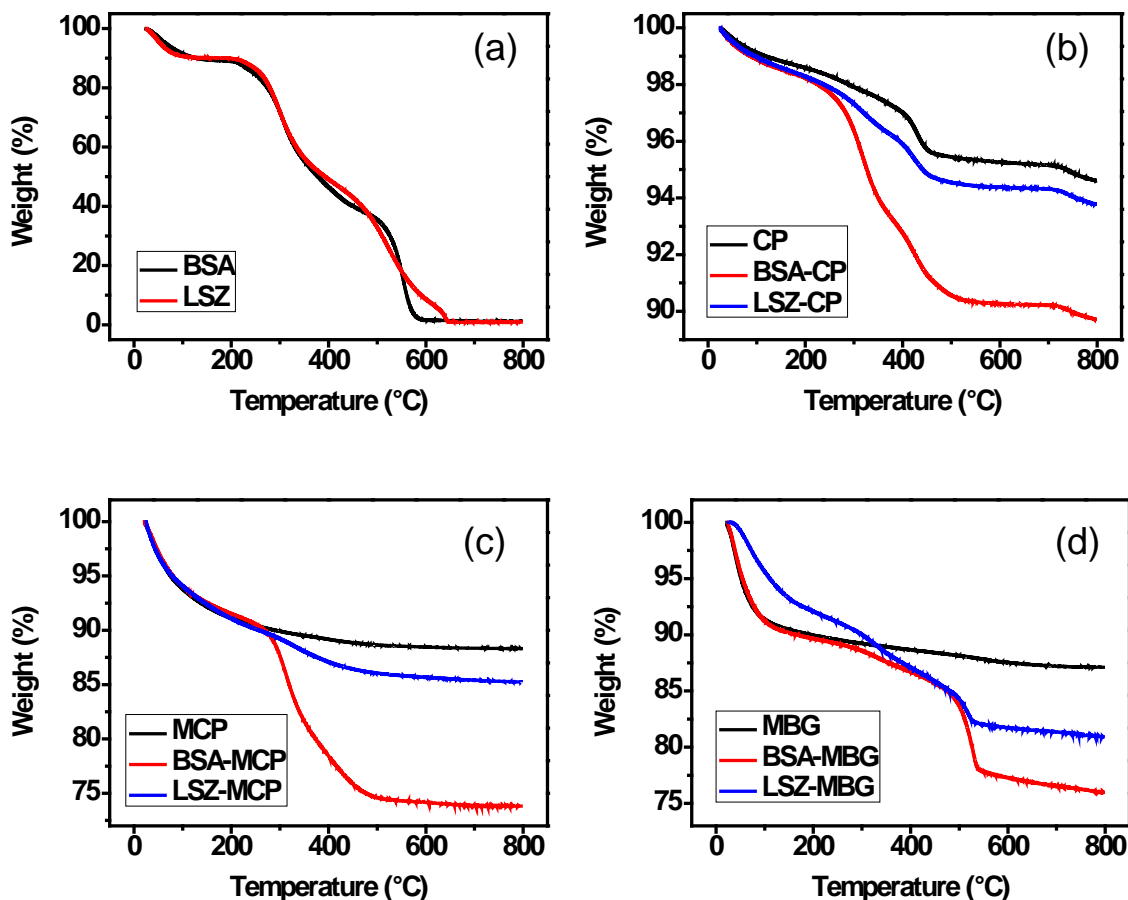
Figure 6.6 Thermograms of BSA & LSZ (a) before loading, (b) after loading into CP; (c) after loading into MCP and (d) after loading into MBG.

6.2.4 Charge interaction

In order to study the charge interaction between protein and the inorganic materials, zeta potential measurement was carried out in the medium similar to the loading condition – aqueous solution. Since the solution pH of the system was around 7, LSZ molecules (pI = 11.1) were positively charged while BSA molecules (pI = 4.7) were negatively charged (Table. 6.2). The surface of CP and MCP were close to neutral (ζ < 10 mV) while the MBG exhibited a negatively charged surface.

Kandori et al. [86] had discussed that the values of zeta potential would increase with increasing protein loading efficiency. The adsorption of LSZ protein on negatively charge surface of MBG was in line with electrostatic attraction. Therefore, LSZ-MBG had the highest protein adsorption among the samples studied (Fig. 6.2). Since the zeta potential of CP was closer to neutral with a lowest net negative charge, the LSZ-CP gave the lowest loading of protein as confirmed by both UV-Vis (Fig. 6.2) and TGA analysis (Fig. 6.6b). Therefore, the adsorption of positively charged protein LSZ on oppositely charged inorganic materials was governed by both the surface area (as mentioned earlier) [177] as well as the electrostatic interaction [107, 108].

Table 6.3 Zeta potential (ζ) value of protein LSZ & BSA and inorganic nanoparticles CP, MCP and MBG in aqueous solution.

Sample	Zeta potential (mV)
LSZ	+15.5 ± 4.6
BSA	-30.4 ± 1.9
CP	-2.2 ± 0.2
MCP	-8.6 ± 1.3
MBG	-22.3 ± 2.4

The adsorption of the negatively charged BSA on the negatively charged MBG gave lowest net charge difference, resulting in the strongest repulsion between BSA and MBG. Besides that, owing to the high surface area of MBG, the repulsive charge on the surface of MBG was thus being augmented; hence the adsorption of BSA-MBG was reduced. In contrast, for zeta potential closer to neutral (zp < 10 mV), there was less charge interaction between MCP or CP and charged protein. Considering the surface area of MCP which was approximately 9 times higher than CP, the high BSA adsorption was dominated by the surface area in a neutral charge environment.

6.2.5 Protein type

6.2.5.1 Conformational stability

It had also been reported that the adsorption mechanism was dependent on the protein structural stability [96, 111, 112]. Proteins with structure highly stabilized by Gibbs free energy such as LSZ would act like a "hard protein". Such protein was known to favorably adsorb on all hydrophobic interfaces under all conditions but only on hydrophilic surfaces of oppositely charged. This was confirmed from the previous study where the positively charged LSZ adsorb on all the oppositely charged surfaces studied.

Conversely, proteins having lower structure stability such as BSA were driven by an extra force to undergo structural rearrangements upon adsorption. As a result, such "soft protein" was able to adsorb on any surfaces under all electrostatic conditions. This was proven in the three inorganic samples which were not electrostatically attracted to the negatively charged

protein BSA. There was still a number of protein molecules adsorbed on the surface regardless of the amount although there was no attractive interaction occurred.

6.2.5.2   Protein adsorption behavior on calcium phosphates

Through the study of calcium phosphates, it was explained that the binding effects of calcium and phosphate ions dissolved in the solutions from calcium phosphates would affect the adsorption affinity [86]. The dissolved Ca^{2+} ions on the calcium phosphate surface had the tendency to bind to the negatively charged BSA. In the case of positively charged LSZ molecules, it can be postulated that the dissolved PO_4^{3-} ions offer an adsorption site in an opposite way. Similar binding mechanism was reported by Becourt et al. [113] and Luong et al. [114].

However, it was observed that the amount adsorbed by LSZ on CP and MCP was generally much less than BSA's according to both the UV-Vis (Fig. 6.2 and 6.3) and TGA measurement (Fig. 6.6b and 6.6c). Kandori et al. [115] realized that the affinity of BSA was much stronger than LSZ in calcium phosphates because the protein BSA exhibited highly irreversible adsorption. This was due to the weak affinity of LSZ to phosphate ions on the calcium phosphate surface as compared to that of BSA which was adsorbed by an electrostatic attractive force. On top of that, since BSA is a "soft protein", its low structural stability adsorb even under a repulsive surface by a structural reorganization, resulting in a higher protein loading [102, 111, 112].

6.2.6 Summary

The protein loading capacity had been analyzed through UV-Vis, FTIR, TGA and zeta potential measurements. In general, the high protein loading capacity could be attributed to several main factors including surface area, electrostatic interaction and conformational stability of protein.

For protein LSZ, the loading efficiency was strongly influenced by the surface area, charge interaction as well as the structural stability. It was shown that with increasing surface area (CP < MCP < MBG) and attractive charge interaction (CP < MCP < MBG), the adsorption capacity increased. The high surface area of mesostructured materials was able to house more proteins, thus increasing the efficiency of protein adsorption. The zeta potential would increase with increasing amount of adsorbed proteins. As a result, the electrostatic interaction of the oppositely charged surface between LSZ and the samples studied facilitated the high LSZ loading efficiency.

In a like charge environment, the adsorption between BSA and MBG was governed by repulsive interaction and surface area. The highly repulsive surface of MBG gave a low loading of BSA in return. For the adsorption of BSA on a neutral charge surface (i.e. MCP and CP), the loading efficiency was mainly due to the surface area and pore volume. Besides that, the low structural stability of BSA allowed structure rearrangement even under unfavorable conditions such as hydrophilic surface and repulsive interaction, thus improving the BSA adsorption amount.

From the materials point of view, MCP could house more BSA molecules than LSZ molecules. This was due to the higher adsorption affinity of BSA to Ca^{2+} ions in comparison to the LSZ to PO_4^{3-} ions on the MCP surface. In addition, the conformational stability of BSA allowed structural rearrangement under all conditions, resulting in a better BSA loading in MCP. Besides that, the pore diameter of MCP which was around 13.5 nm could better fit in by the larger BSA molecules ((4 x 4 x 14 nm^3) than LSZ, allowing a better pore accessibility for efficient BSA loading.

Another remarkable result was that MBG was adsorbed by the highest amount of LSZ but the lowest amount of BSA across the three samples. This phenomenon was generally governed by the electrostatic interaction followed by surface area. For adsorption between LSZ and MBG surface, the attractive interaction occurred. This further augmented the attraction in high surface area MBG, resulting in a high LSZ adsorption capacity. Likewise, for the same charge interaction between BSA and MBG, a large repulsion charge was on the surface of high surface area MBG, resulting in the rejection of protein adsorption on MBG, thus the loading was very low. Last but not least, the tertiary structure of both LSZ and BSA retained after adsorption of all the samples studied (CP, MCP and MBG) was preserved through the UV absorbance spectra shown.

6.3 *In vitro* release of protein from mesostructured materials

6.3.1 UV-Vis measurement

The *in vitro* experiments monitoring the release of the protein LSZ and BSA from CP, MCP and MBG were performed in pH 7.4 PBS. Here three parallel *in vitro* protein release measurements were conducted, and all data were expressed as means ± standard deviation (SD) for *n* = 3. Fig. 6.7a plots the release profile of BSA from MCP and CP in the initial 24 hour incubation. The release of BSA from MCP (99 µg/mg) and CP (29.5 µg/mg) was fast in the first 1 hour. After that, between 1st and 8th hour, the release rate decreased, releasing cumulative amount of 192 µg/mg (MCP) and 70 µg/mg (CP) of BSA molecules. Next, the release rate of BSA from MCP (253 µg/mg) and CP (92 µg/mg) was slower down between 8 and 240 h (10 days) as shown in Fig. 6.7c. Overall, the release rate of BSA from MCP in the first day (24 h) was higher than CP.
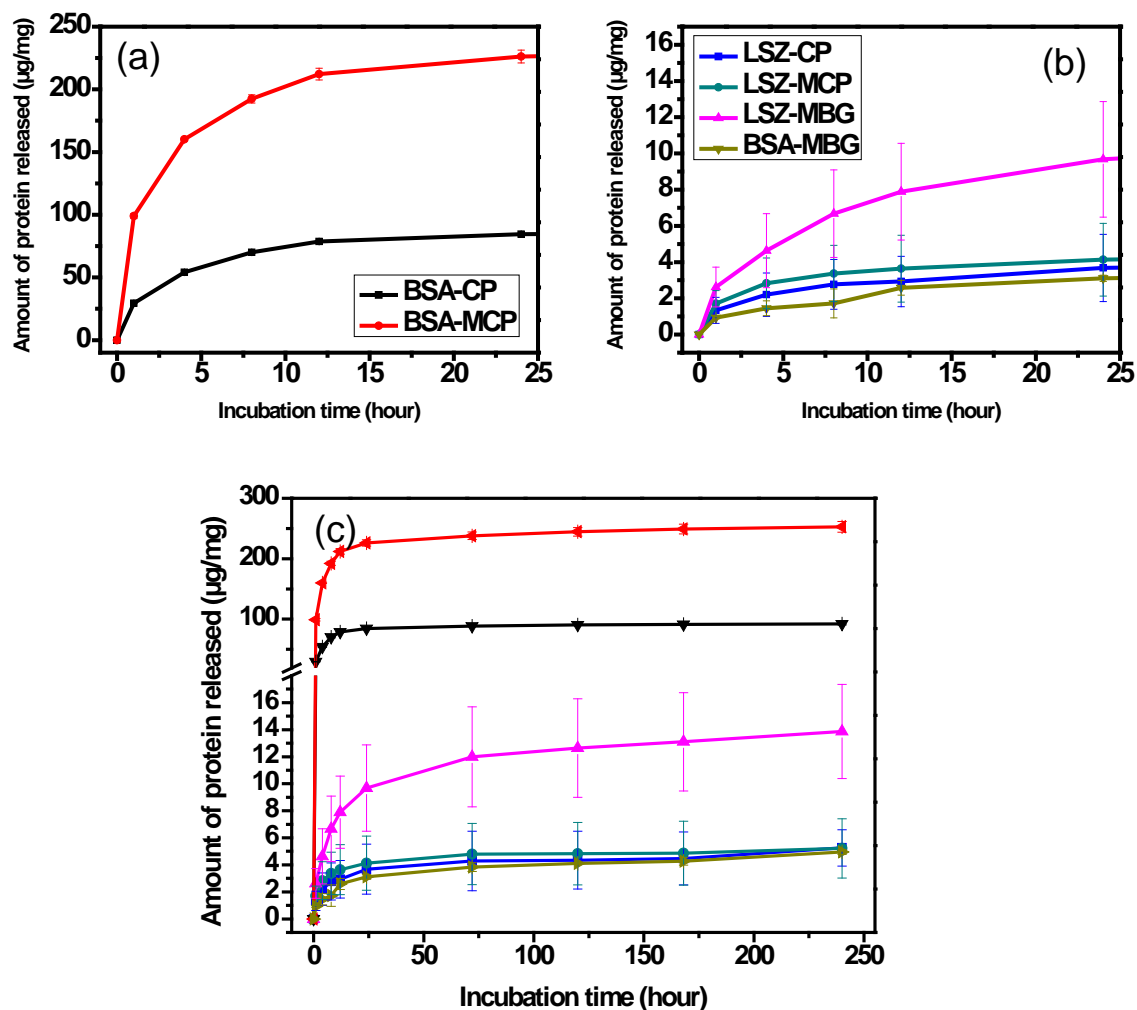
Figure 6.7 Cumulative amount of protein released: (a) BSA-CP & BSA-MCP; (b) LSZ-CP, LSZ-MCP, LSZ-MBG and BSA-MBG over first 24 h; (c) over a period of 250 h study.

The release rate of protein as a function of time as illustrated in Fig. 6.7b was lower than the release of BSA-CP and BSA-MCP as shown in Fig. 6.7a. The slow LSZ release from MBG showed an initial burst of 2.6 µg/mg LSZ within 24 h and achieved 12 µg per mg of LSZ loaded MBG after 72 hour. The subsequent release was performed at an even lower rate, releasing a total amount of 13.9 µg/mg LSZ up to 240 h (Fig. 6.7c). For the low protein release of LSZ-CP, LSZ-MCP and BSA-MBG (Fig. 6.7b), their release behaviour was comparable throughout the study. In these samples, a fast release occurred in the first hour,

followed by a slower release of protein ($< 4 \, \mu g/mg$), up to 24 h of sample incubation. Next, a steadily decreasing release of protein was shown up to the end of the release (240 h) (Fig. 6.7c). The total amount of protein being released from LSZ-CP, LSZ-MCP and BSA-MBG was $5.26 \, \mu g/mg$, $5.22 \, \mu g/mg$ and $4.95 \, \mu g/mg$, respectively.

Fig. 6.7c shows the LSZ and BSA release behaviours from CP, MCP and MBG system over a 240 h period at pH 7.4 PBS. Generally, the curves showed an initial fast release followed by a subsequent slow release profile. The fast release was due to the dissolution of the protein which was physically adsorbed on the surface of the inorganic materials. The slow release of protein might be due to the chemically adsorbed proteins. The release rate of the initial fast release part could be predicted using the theoretical model by Higuchi [122] in the following equation:

$$a = kt^{1/2} \tag{6.1}$$

where a is the release amount after time t and k is the release constant.

These assumptions [121] were (i) the initial protein concentration in the system was much higher than the matrix solubility; (ii) perfect sink conditions were maintained; (iii) the diffusivity of the protein was constant and (iv) the swelling of the polymer was negligible.

Table 6.3 provides the release constant k of protein from inorganic sample in the first 8 h. The k of BSA-MCP which was 68.0 was much larger than other protein loaded samples,

indicating the fastest release in the first 8 h. The release constant k of BSA-CP and LSZ-MBG were 24.8 and 2.36, respectively. For LSZ-MCP, LSZ-CP and BSA-MBG, their release constant k was lower than 1.2, signifying a slower release than other protein loaded samples.

Table 6.4 The release constant (k) of protein from the inorganic samples in the first 8 h.

Samples	k (h$^{-1/2}$)
LSZ-CP	0.98
LSZ-MCP	1.19
LSZ-MBG	2.36
BSA-CP	24.8
BSA-MCP	68.0
BSA-MBG	0.61

For the dispersion of protein and the diffusion through solvent-filled pores in a matrix, the formulation of the release constant k was dependent on several factors:

$$k = f\ (D, \varepsilon, C, A) \tag{6.2}$$

where D is the diffusivity of the protein in the solvent, ε is the porosity of the matrix, C is the solubility of the protein in the solvent used and A is the total amount of the protein loaded in the matrix.

For the CP, MCP and MBG studied the release tests were carried out all in PBS. Hence, considering protein BSA released from the inorganic samples, the release constant k was highest in BSA-MCP and lowest in BSA-MBG. Therefore, k was dependent on the high loading of BSA (A). The release of LSZ was similarly affected by the total amount of LSZ loaded (A).

Next, each of the inorganic samples were compared with the two proteins being released (i.e. LSZ-CP vs BSA-CP). It was clearly shown that the difference in their release kinetics (k) in the first 8 h was affected by A, which was the amount of protein being loaded for the release test. Since the protein loaded samples were all kept at 20 mg, hence the amount of protein presented in the inorganic samples was dependent on its adsorption efficiency. The release rate (k) increased with the increase of protein loading; therefore BSA-MCP having a high loading efficiency had a large k value, followed by BSA-CP and LSZ-MBG. Since the adsorption capacity of LSZ-CP, LSZ-MCP and BSA-MBG were comparably low, their release constant (k) as shown in Table 6.3 was less than 1.2.

6.3.2 Protein stability

Marco et al. [27] reviewed that the protein structure after loading in polymer particles was not fully preserved. One of the factors was due to the preparation process where the polymer is exposed to harsh environments, such as heating, sonication, and organic solutions [28, 29]. For instance, Qi et al. [174] had reported that uncoated catalase-loaded solid lipid nanoparticles prepared in 1:1 acetone/DCM environment lost its protein activity with 1 hour

after release. Another factor could be due to the release process. The instability has been attributed to a local pH drop inside the particles due to trapped acid PLGA degradation products [178-180].

The protein stability of BSA released from mesoporous and non-mesoporous calcium phosphate (MCP) was studied to monitor any possible structural changes due to protein denaturation during sample preparation. The residue ellipticity (θ) of BSA after release at the 190 – 260 nm region determined by the circular dichroism (CD) spectropolarimeter is shown in Fig. 6.8a. The CD spectra of BSA after release from CP and MCP exhibited strong negative ellipticity at 208 and 222 nm, which was a typical secondary α-helical structure of protein [181]. While for the low release of BSA-MBG (inset), the concentration detected was much lower. The two negative peak maxima at 208 and 222 nm could be observed from the CD spectrum. The results here therefore proved the ability of calcium phosphate, mesoporous or non-mesoporous in nature, in preserving the structure of BSA proteins. This is due to the advantageous approach of loading proteins onto pre-synthesized calcium phosphate under physiological conditions. Unlike polymeric nanoparticles [27-29, 178-180], the high surface area of MCP is therefore not only able to achieve high loading efficiency, but also able to retain the structure of BSA.

On the other hand, due to the minor α-helical conformation of LSZ [99], a weaker ellipticity of LSZ after release from CP, MCP and MBG is detected in Fig. 6.8b. The broader negative ellipticity (θ) of LSZ which scanned between 200 and 250 nm was centred at 208 and 229

nm. Through this bioactivity study, it was confirmed that the secondary structure of the

protein was retained after release.
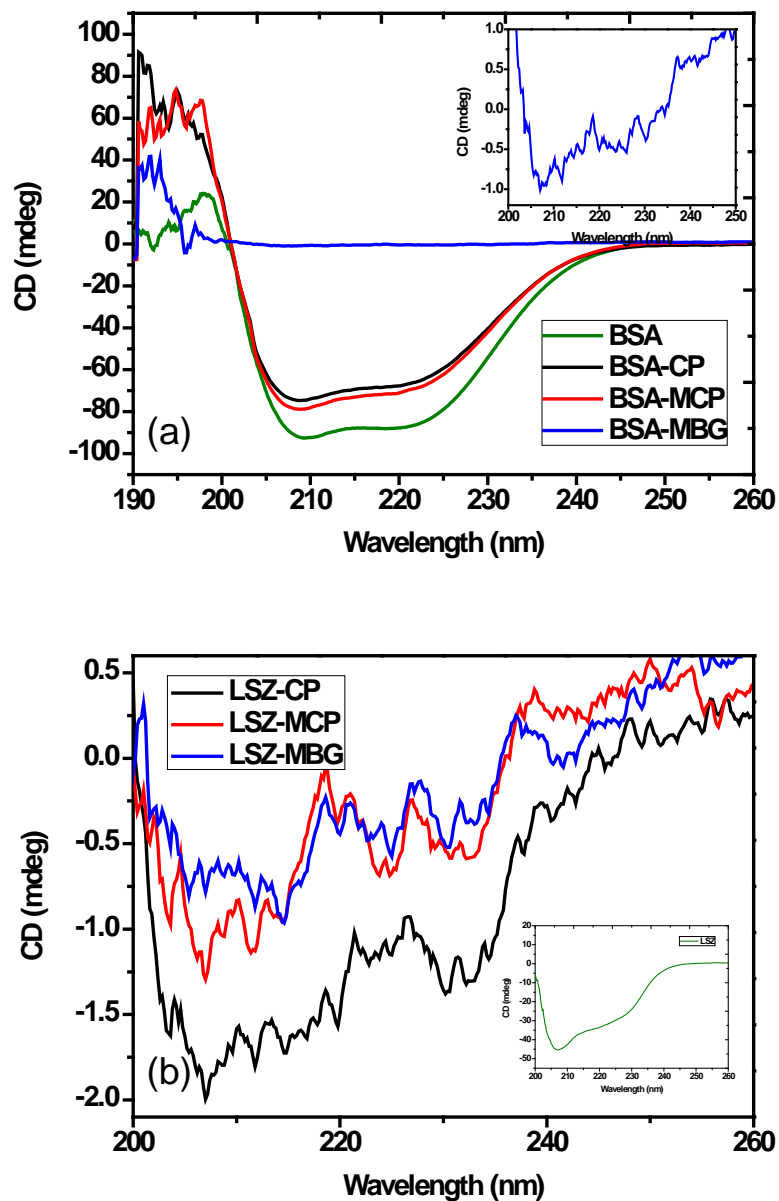
Figure 6.8 CD spectra of (a) Bovine serum albumin (BSA) and (b) Lysozyme (LSZ) after being released from the CP, MCP and MBG nanoparticles and pure proteins were used as controls (green color).

6.3.3 Summary

The protein release profile from the mesostructured materials (MCP and MBG) as well as the control (CP) exhibited an initial fast release followed by a steadily decreased rate with time. According to the formulation of the Higuchi model [122], the release constant (k) of protein for the initial 8 h was calculated. The amount of protein released from the samples was dependent primarily on the amount of protein loaded (A). The bioactivity of proteins LSZ and BSA released from the inorganic materials was supported by the CD measurements. The secondary structure of both the proteins was preserved after release.

CHAPTER 7

7 IN VITRO DEGRADATION AND PROTEIN RELEASE FROM PLGA/MESOPOROUS MATERIALS FILM

Mesostructured materials had been examined and proved that its high surface area properties was able to house higher amount of protein molecules and more proteins could then be released *in vitro* as compared to the nonporous materials. Many reports had revealed that the ceramic-polymer composite could have better combined mechanical and physiological properties in the field of biomaterials. For instance, the hydrophilicity and the acidic degradation by-products released from polymers during degradation could be improved by incorporating bioceramics such as calcium phosphates and bioactive glasses [78, 84, 182]. Therefore, it was speculated that the combination of high surface area mesostructured ceramics with biodegradable polymers would further enhance the physiochemical and biological properties as well as protein adsorption.

7.1 Film degradation studies

7.1.1 Effect of MCP content on PLGA film *in vitro* degradation

The highest surface area of mesostructured calcium phosphate (MCP) (Table 6.1) synthesized was studied in this experiment. MCP of different weight ratios (1MCP/PLGA, 5MCP/PLGA and 10MCP/PLGA) was explored to study the *in vitro* degradation and surface

morphology. Together, 75/25 poly(DL-lactide-glycolide) (PLGA) would serve as the polymer matrix for the dispersion of MCP.

7.1.1.1 Buffer absorption and mass loss of MCP/PLGA

Fig. 7.1 shows the influence of MCP of different weight ratios on the buffer absorption of the PLGA film over a period of 56 days. Within the first 14 days of incubation, the buffer absorption increased with increasing MCP content. For PLGA film which acted as the control, the buffer uptake shown was comparable low with a slow increase throughout the 49 days incubation. However, a sudden increase of buffer absorption (131.5 %) was exposed after day 49. The increase in buffer uptake signified the soluble oligomers fragments and monomer products were formed.

For the addition of MCP into PLGA films, buffer absorption of the composite films increased rapidly with time for the initial 2 weeks. For 10MCP/PLGA film, the buffer uptake increased gradually over the 56 days incubation with a final increase of 41 %. In contrast, the 1MCP/PLGA and 5MCP/PLGA films experienced a sudden increase of buffer absorption after 35 days of immersion, which was similar to the degradation profile of PLGA film (control) after 49 days. The buffer uptake of 1MCP/PLGA and 5MCP/PLGA film was 110.6 % and 99.2 %, respectively in the end of the period of incubation.
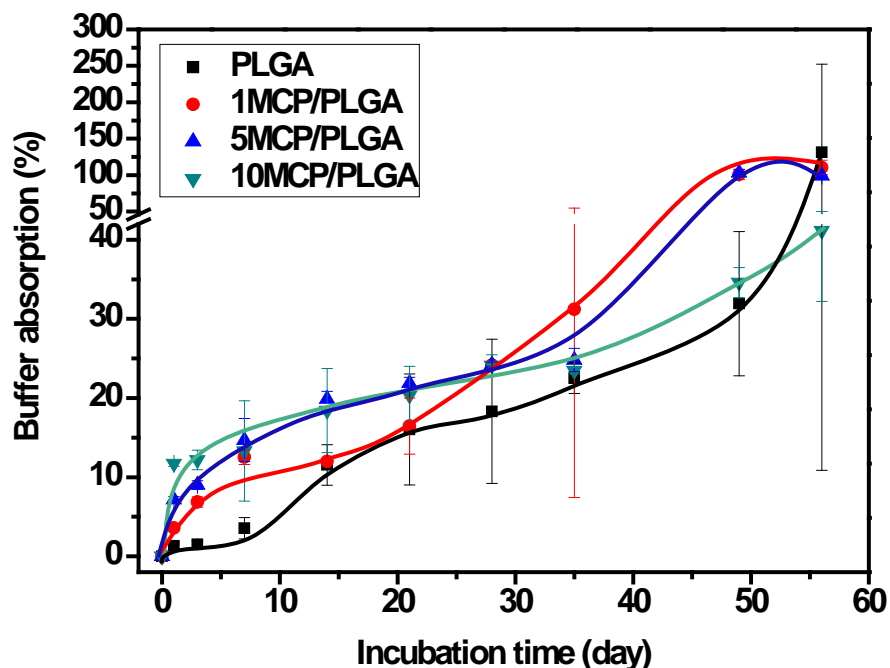
Figure 7.1 Percentage buffer absorption of 0, 1, 5 & 10MCP/PLGA films over 56 days of in vitro degradation.

The effect of MCP content on the mass loss of the PLGA film over a period of 56 days is depicted in Fig. 7.2. The PLGA, 1MCP/PLGA and 5MCP/PLGA films possessed a similar mass loss pattern: a fast loss of mass in the initial stage, followed by an increase at a reduced rate and an exponential loss of mass after 35 days of immersion. The rate of rapid mass loss decreased with increasing MCP weight ratio, where the rate of mass loss of 5MCP/PLGA film was lower. The mass loss pattern of 10MCP/PLGA film was different from the other three samples. The mass loss of this film increased progressively with time for the initial 2 weeks and continued to increase at a reduced rate up to 56 days. At the end of film incubation, all the films reached a mass loss of 84 % (PLGA), 70 % (1MCP/PLGA), 40 % (5MCP/PLGA) and 16 % (10MCP/PLGA).
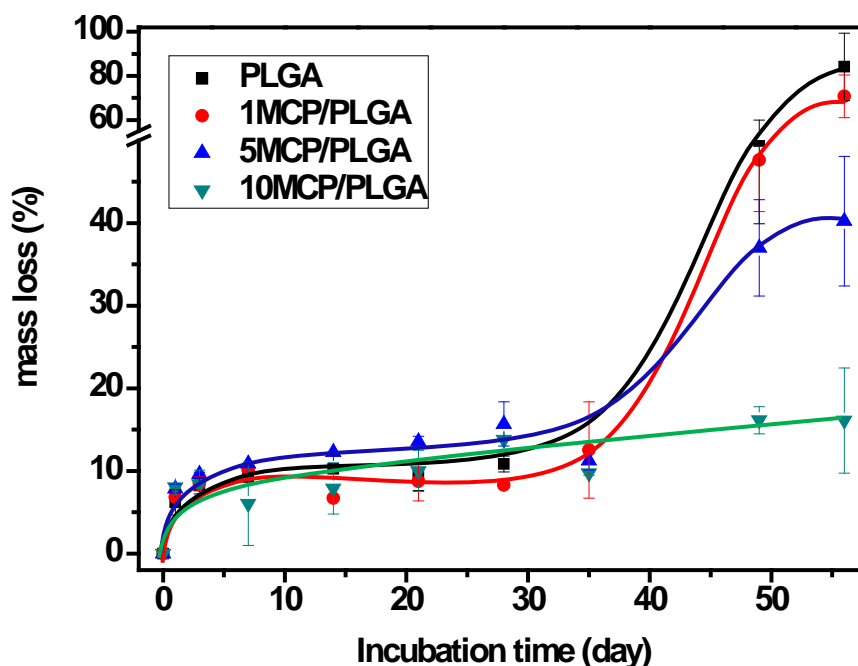
Figure 7.2 Percentage mass loss of 0, 1, 5 & 10MCP/PLGA films over 56 days of in vitro degradation.

The initial buffer absorption and mass loss of the control (PLGA film) were lower as compared to composite film due to absence of MCP. The degradation was mainly contributed to the dissolution of the soluble oligomers produced by the degradation of PLGA upon incubation. At the same time, the pH environment of the polymer matrix became more and more acidic when most of the oligomers fragments and monomer products turn soluble. At certain time point, when most of the water soluble degradation products (oligomers and/or monomers) diffused out of the PLGA film and dissolved in the surrounding buffer, a rapid buffer uptake and mass loss would be detected.

The buffer absorption and mass loss examined in this PLGA/MCP composite system was initially contributed to the presence of MCP, which lead to the increase of the bulk hydrophilicity of the PLGA matrix. As a result, the polymer chains were converted into shorter fragments at a faster rate. Finally, when there was a rapid increase of buffer absorption and mass loss, the dissolution of oligomers in PBS dominated [182]. The increase of the buffer absorption and mass loss were due to the dissolution of the accumulated hydrophilic acidic oligomers and monomers formed during the degradation process. PLGA would then become completely soluble.

Comparing the buffer absorption result of PLGA and MCP/PLGA, it was clearly shown that the addition of MCP in PLGA film enhanced the bulk hydrophilicity of PLGA especially in the early 14 days of *in vitro* degradation. This improved absorption was able to manipulate the degradation rates of the materials as reported by Loher et al. [183]. However, over a long period of incubation time, higher MCP content (10MCP/PLGA) in PLGA film would help to prevent the rapid uptake of buffer by retarding the autocatalysis effect of polymer film [84] which would lead to the increase of acidic pH surrounding the environment [182, 184] and provoke inflammatory response.

7.1.1.2   Thermogravimetric analysis

The change of mass loss measured was the result of two competing processes: (1) dissolution of oligomers/degradation products and (2) leaching of the MCP content. In our study, the chances of mass loss due to the dissolution of the MCP were minimized because the samples

studied had low solubility in water [182]. Since the weight of composite after degradation consisted of MCP, adsorbed water and the remaining PLGA, a rough estimation on the contribution of the mass loss was conducted using thermogravimetric analysis (TGA) from room temperature up to 800 °C in air. As a result, both the PLGA and the water would be removed, and the remaining residue calculated would be the remaining weight percentage of MCP.

Fig. 7.3 plots the percentage of MCP content remained inside MCP/PLGA film after incubated for 7 and 28 days. The MCP content before incubation (day 0) was normalized to 100 %. At day 7, all the MCP percentage inside the MCP/PLGA films increased in comparison to day 0, with the MCP content highest in 1MCP/PLGA film and lowest in 5MCP/PLGA film. For films after 28 days of incubation, it was examined that the MCP content in 1MCP/PLGA film decreased and lower than the content before immersion. All the MCP contents were decreased from day 7 to day 28 degradation.

The initial increase of MCP content in the composite film at day 7 contributed to the dissolution of degradation products at this stage. Referring to Fig. 7.1 and 7.2, it was believed that in the earlier stage (before day 7) of degradation, the presence of MCP inside the polymer matrix increased the bulk hydrophilicity (buffer absorption). At the same time, leaching of MCP took place, resulting in a better freedom for PLGA to convert its chains to shorter water soluble fragments due to the minimization of buffering effect by MCP. The higher percentage of MCP found at day 7 signified that the dissolution of oligomers was faster than the leaching, resulted in an arbitrary higher proportion of MCP in the matrix. At

day 28, the leaching of MCP dominated. Since the lower amount of MCP provided a room for the high conversion of polymer chains to short fragments, buffer uptake of MCP/PLGA films was increased. However, the mass loss showed that the leaching of MCP was low but at a relatively faster rate than dissolution of degradation products as illustrated in the TGA measurements (Fig. 7.3).
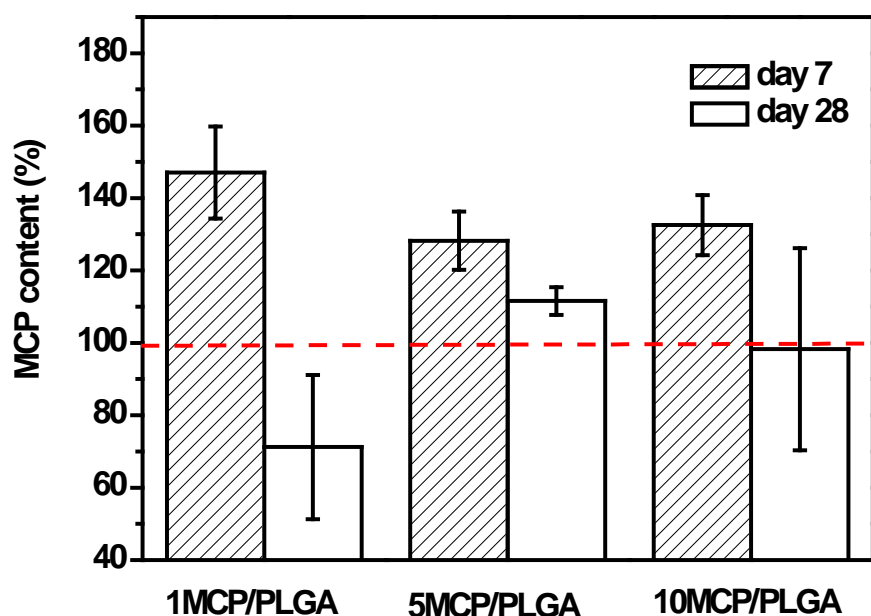
Figure 7.3 Percentage of MCP content remained on 1MCP/99PLGA, 5MCP/95PLGA and 10MCP/90PLGA films after day 7 & day 28 degradation, calculated by determining the residue left from the TGA thermogram.

7.1.1.3   Molecular weight change

Fig. 7.4 shows the molecular weight change of PLGA for the 4 samples with time. Over a period of 49 days, the molecular weight of all the films decreased right after placement in buffer solution and continued to decrease throughout the incubation period. With increasing MCP amount, the molecular weight of PLGA decreased slower. The control PLGA film

degraded and lost its 96 % of M_w after 49 days of incubation. While for MCP/PLGA composite films, the M_w of 1MCP/PLGA, 5MCP/PLGA and 10MCP/PLGA decreased 94 %, 91 % and 80 %, respectively.
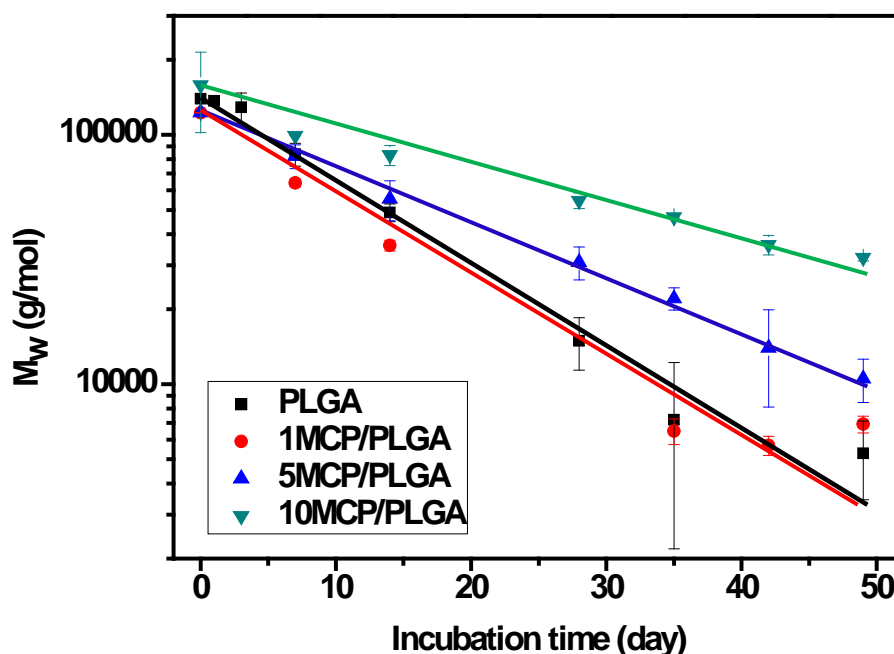
Figure 7.4 Molecular weight change of 0, 1, 5 & 10MCP/PLGA films over 56 days of in vitro degradation.

The study of the molecular weight provided information of the weight of the polymer matrix including insoluble degradation products and some soluble products that did not diffuse out of the matrix. With increasing MCP content, the pH environment was controlled; hence less generation of the oligomers and monomers in PLGA matrix. As a result, the molecular weight of the PLGA decreased at a slower rate and the degradation of the polymer was retarded.

7.1.1.4   Surface morphology

Fig. 7.5 displays the secondary electron images (SEI) of 10MCP/PLGA film incubated at (c) day 0 and (d) day 42 with reference to the PLGA film (control). The PLGA film had a smooth and flat surface at day 0 and pores of size approximate 3 μm were seen on the surface which might be due to the dissolution of acidic degradation products form in bulk of the film.
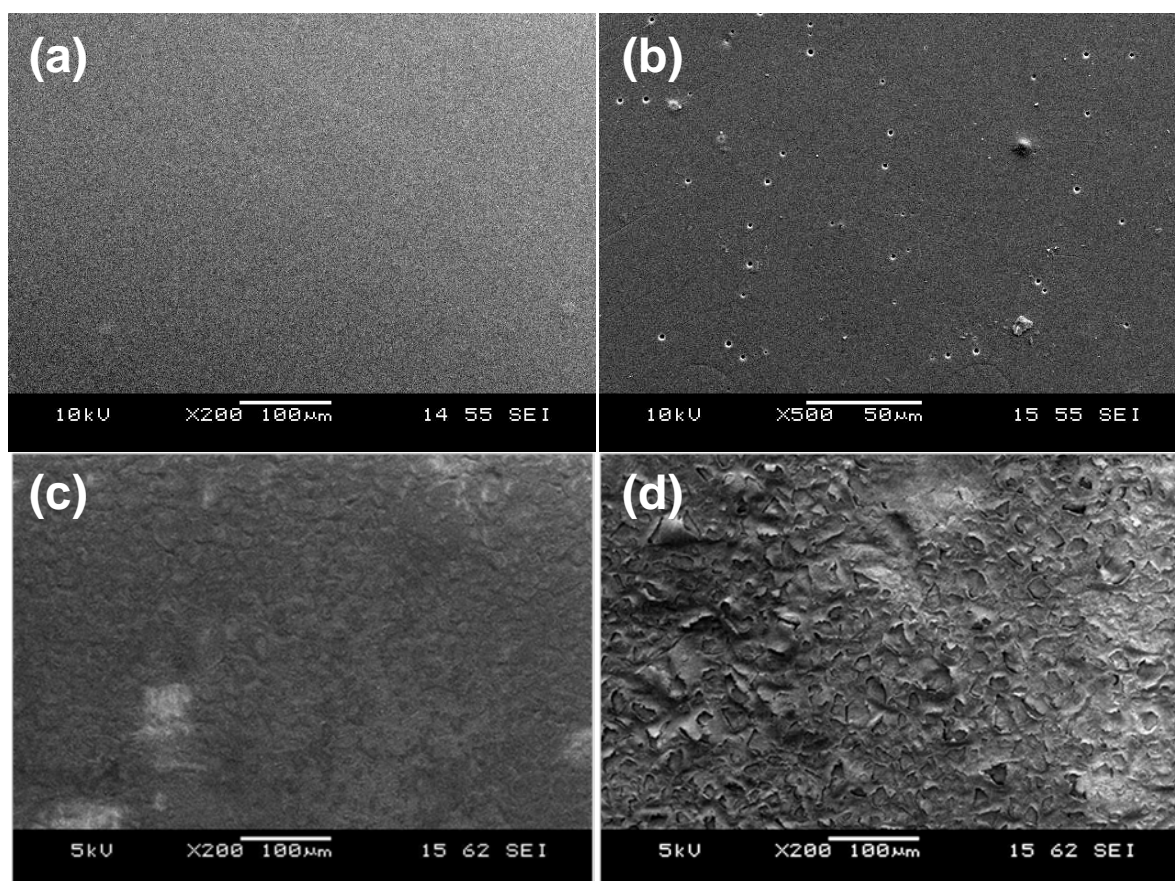
Figure 7.5 Surface morphologies of PLGA (control) (a) before degradation, (b) after 42 days of in vitro degradation, magnification = 200 & 500; 10MCP/90PLGA film (c) before degradation and (d) after 42 days of in vitro degradation, magnification = 200.

Before immersion, the 10MCP/PLGA film was rough due to the dispersion of MCP into PLGA solution during fabrication. No inclusion was observed on the surface of the film. At day 42, the surface of the PLGA was roughened and slit of cracks were visible on the surface. The formation of cracks was correlated mainly to the diffusion of the acidic degradation products and minor leaching of MCP content from the PLGA matrix. As the cracks completely propagate through the material, diffusion rates might speed up.

7.1.2 Effect of MBG content on PLGA film *in vitro* degradation

The highest surface area of mesostructured bioactive glasses (MBG) (Table 6.1) synthesized was studied in this experiment. Similar to MCP, MBG of varying content (1MBG/PLGA, 5 MBG/PLGA and 10 MBG/PLGA) was explored to study the *in vitro* degradation and surface morphology. Together, 75/25 poly(DL-lactide-glycolide) (PLGA) would serve as the polymer matrix for the dispersion of MBG.

7.1.2.1 Buffer absorption and mass loss of MBG/PLGA

The effect of MBG content on the buffer absorption of the PLGA film over a period of 56 days is shown in Fig. 7.6. In the early 7 days of immersion, the buffer absorption showed an increasing trend with increasing MBG content. For the 100 % PLGA film (control), the buffer absorption was gradually increased until day 49 of incubation. Beyond this time point, a sudden increase of buffer uptake (131.5 %) was achieved. As discussed earlier, the rapid increase in buffer absorption was due to the dissolution of the accumulated hydrophilic acidic oligomers and monomers formed during the degradation process.
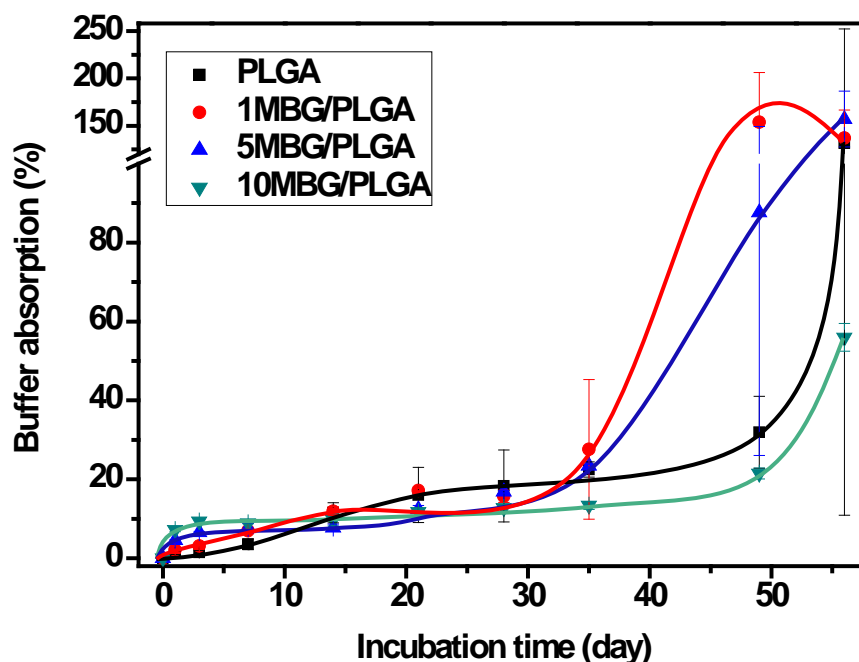
Figure 7.6 Percentage buffer absorption of 0, 1, 5 & 10MBG/PLGA films over 56 days of in vitro degradation.

The buffer absorption pattern of 1MBG/PLA film was similar to the PLGA film (control). Its buffer absorption increased progressively with time, reached a maximum at day 49 and then decreased. For 5MBG/PLGA film, the buffer uptake was similar to 1MBG/PLGA film but at a longer incubation time to reach the rapid increase of buffer absorption. The incorporation of higher MBG content into PLGA film (10MBG/PLGA) resulted in a steadily increase of buffer uptake, prior to an increase of buffer uptake from day 49 (21.5 %) to day 56 (56 %) of immersion. It was speculated that the buffer uptake might increase if the 10MBG/PLGA film was placed in the PBS for longer period of time. However, the increase would still lower than the control.

The mass losses of the MBG/PLGA films together with the control are illustrated in Fig. 7.7 over 56 days of PBS immersion. It was clearly shown that all the sample curve plotted have a similar trend, with the difference of time point of which rapid mass loss would occur at the later stage of the incubation. With increasing MBG content, the mass loss from the PLGA film increased. And this trend was sustained for 4 weeks (28 days). After which, the PLGA and 1MBG/PLGA films experienced a rapid loss of mass and reached 84 % and 64 %, respectively at day 56. Similarly, the 5MBG/PLGA film also experienced the same rapid loss of mass at a slower rate and reached 69 % of mass loss at the end of degradation study. Nonetheless, for 10MBG/PLGA film, the rapid loss only happened after 49 days of incubation and had a 52 % of mass loss at day 56.

Through the MBG/PLGA composite system study, it was shown that the system could be manipulated by varying content of MBG. Similar to the MCP/PLGA system, the buffer absorption and mass loss profiles were initially contributed by the buffer uptake of the polymer degradation products. When the dissolution of acidic carboxyl end groups formed during the degradation process took place, the buffer absorption and mass loss were rapidly increased, the diffusion of the soluble oligomers and monomer products occurred (mass loss) and hence the polymer matrix became completely soluble (buffer absorption). The higher MBG content of PLGA film (i.e. 10MBG/PLGA film) was proven to be able to buffer the pH environment acidified by the degradation products [78, 84] and minimized the buffer uptake and mass loss. The presence of MBG could lengthen the mid time phase diffusion process because the inorganic samples could neutralize the pH environment of the matrix and prevent rapid mass loss and buffer absorption to take place.
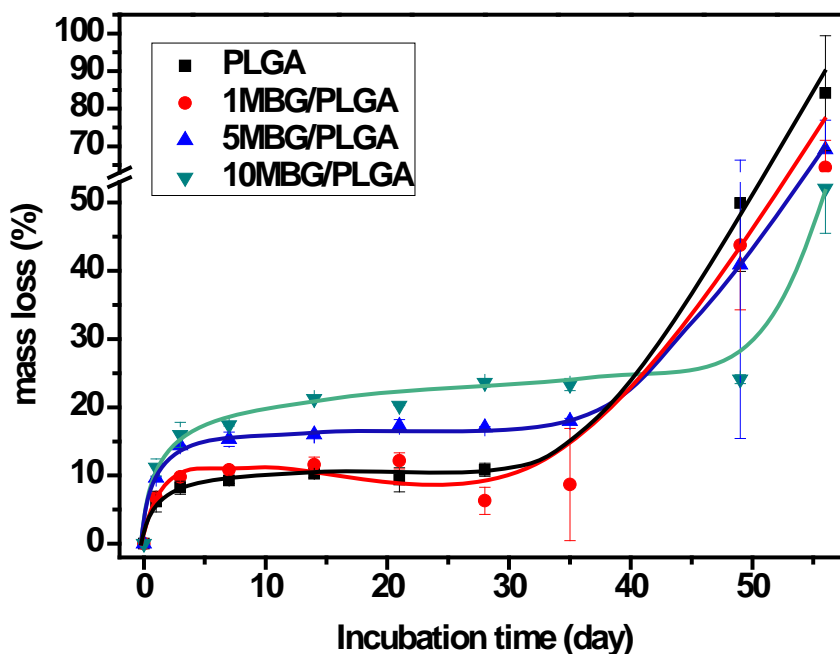
Figure 7.7 Percentage mass loss of 0, 1, 5 & 10MBG/PLGA films over 56 days of in vitro degradation.

7.1.2.2   Thermogravimetric analysis

The remaining MBG content after degradation for 7, 14, 28 and 56 days was studied using TGA as shown in Fig. 7.8. It was found that both 1MBG/PLGA and 5MBG/PLGA had a similar trend presented where the MBG content increased at day 7, but then decreased at time point 14 and 28, and followed by a high increase of MBG content at day 56 of *in vitro* degradation. In contrast, the MBG content of 10MBG/PLGA started to decrease after day 7 of immersion, then maintained at a comparable percentage of MBG up to day 56.
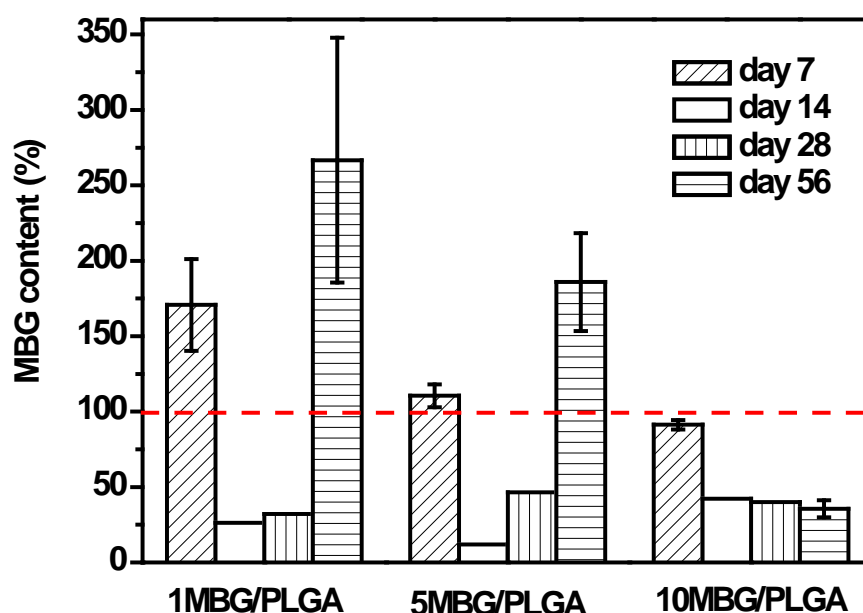
Figure 7.8 Percentage of MBG content remained on 1MBG/99PLGA, 5MBG/95PLGA and 10MBG/90PLGA films after day 7, 14, 28 & 56 of in vitro degradation, calculated by determining the residue left from the TGA thermogram.

With reference to the buffer absorption (Fig. 7.6) and mass loss (Fig. 7.7) study of MBG/PLGA, the buffer uptake and mass loss increased with increasing MBG weight ratio in the initial stage of degradation. At time point day 7, the presence of MBG increased the bulk hydrophilicity of the PLGA matrix; hence the diffusion of acidic degradation products of PLGA occurred (mass loss increased). Although the hydrophilicity and mass loss were increased in higher MBG weight ratio which we expected more acidic degradation products would diffuse out from 10MBG/PLGA, an opposite trend was observed in the TGA measurement (Fig. 7.8). This was contributed to the pH neutralization effect of MBG, where higher content of MBG can slow down the degradation by buffering the acidic environment in PLGA matrix during degradation. Hence, it was observed that in 1MBG/PLGA film, the percentage of MBG content remained was the highest as the amount of the acidic degradation

products diffused out was the greatest. Hence, it was predicted that both the early dissolution of acidic degradation products (dominated in 1MBG/PLGA film) as well as the leaching of MBG (dominated in 10MBG/PLGA) took place at the time period earlier than day 7.

At day 14 and 28 of degradation, both the buffer absorption (Fig. 7.6) and mass loss (Fig. 7.7) of the composite films increased at a reduced rate compared to day 7. The percentage of MBG content remained was decreased. At this stage of time, there was a competing process between the degradation fragments and the MBG which served as a buffering tool. Hence, the bulk hydrophilicity did not increase tremendously and less number of acidic products was diffused out (stable mass loss). Therefore, the percentage of the MBG content remained after 800 °C of combustion could be governed by the accumulation of non soluble degradation products, especially in lower weight ratio of MBG, resulting in a lower arbitrary proportion of MBG in the PLGA matrix. However, a slow leaching of MBG occurred, allowing the degradation products to be accumulated.

At the end of 56 days degradation, the remained content of MBG was greatly increased in both 1MBG/PLGA and 5MBG/PLGA films. This showed that the degradation products themselves undergo the autocatalysis [84], resulting in a rapid increase in buffer absorption and mass loss. The dissolution of the oligomers would then dominate at this stage. For 10MBG/PLGA, the degradation was retarded, hence no sudden increase of remaining MBG content could be observed at this moment. This film was still experiencing the second stage of degradation where a balance between the presence of MBG and the oligomers took place.

7.1.2.3   Molecular weight change of MBG/PLGA

The molecular weight change of MBG/PLGA film as well as the control was examined over an incubation period of 49 days as illustrated in Fig. 7.9. The molecular weight of the PLGA films decreased after being immersed in PBS and continued to decrease throughout the immersion period. The molecular weight decreased at a slower rate with increasing MCP amount. The M_w losses for PLGA, 1MBG/PLGA, 5MBG/PLGA and 10MBG/PLGA were 95 %, 94 %, 90 % and 78 %, respectively after 35 days of incubation.

Therefore, the incorporation of MBG at a higher content (> 10 wt%) could prohibit the fast degradation and molecular weight change resulted from the acidic degradation products. The presence of MBG could maintain a neutral pH environment for the degradation to be conducted.
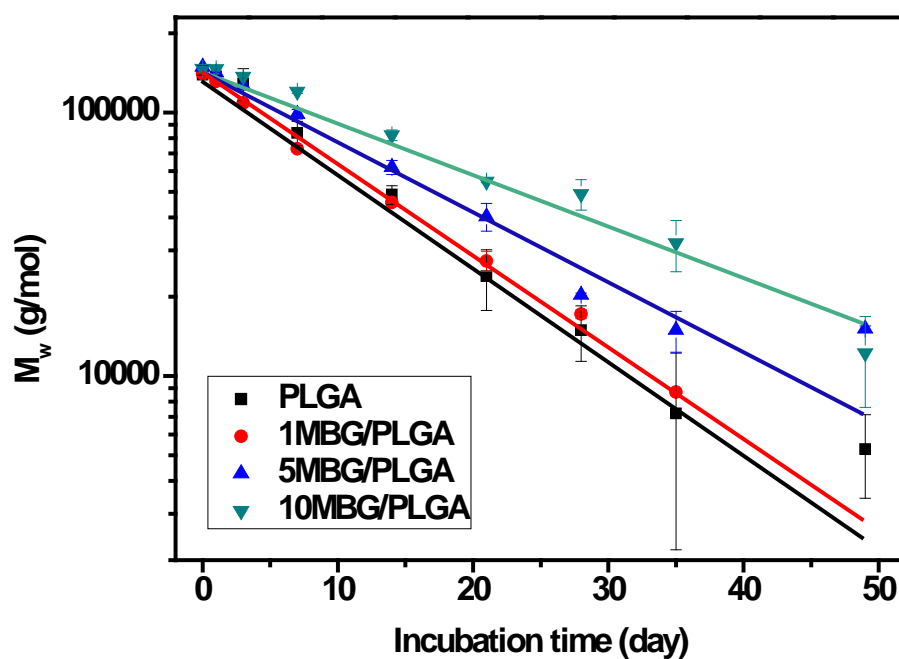
Figure 7.9 Molecular weight change of 0, 1, 5 & 10MBG/PLGA films over 56 days of in vitro degradation.

7.1.2.4   Surface morphology

The surface morphologies of 10MBG/PLGA film (a) before and (b) after 42 days of incubation are shown in Fig. 7.10. Compared to the film at day 0, the surface was roughened and pores were formed on the surface of 10MBG/PLGA film after incubation for 42 days. This was due to the diffusion of the oligomers and monomers when both buffer absorption and weight loss were rapidly increased.
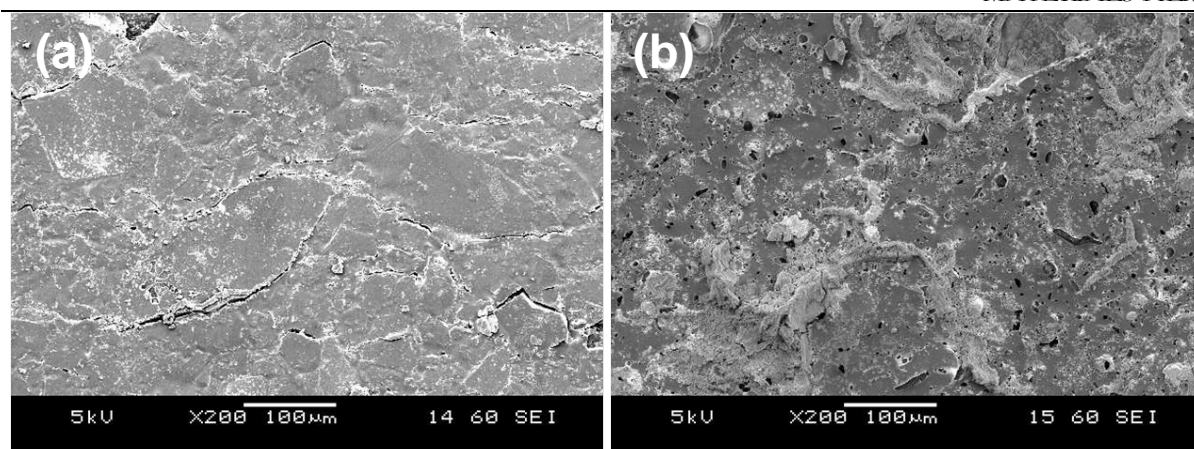
Figure 7.10 Surface morphology of 10MBG/90PLGA film (a) before degradation and (b) after 42 days of in vitro degradation, magnification = 200.

7.1.3 Summary

The *in vitro* degradation of PLGA/MCP and PLGA/MBG composite film was examined through the measurement of buffer absorption, weight loss, thermogravimetric analysis (TGA), molecular weight change through Gel Permeation Chromatography (GPC) and scanning electron images (SEI) over a period of 56 days. Three different weight ratios of MCP and MBG were compared with the control PLGA film in this study.

Higher content of MCP or MBG increased the initial buffer absorption of the polymer matrix. The polymer chains were then converted into shorter water soluble fragments. Therefore, a faster rate of degradation was expected. However, the basic product of MCP and MBG helped to lower the acidic pH environment created by the oligomers and monomers from PLGA, thus retarding the degradation. Hence, it was concluded that the presence of MCP or MBG ($\geq$ 10 wt%), increased the buffer uptake of the polymer matrix without causing a rapid loss of buffer uptake and mass loss throughout the degradation process. It was deduced that a

competing process between the buffering effect of the inorganic materials, leaching of the inorganic materials and the dissolution of acidic degradation products took place especially in the mid phase of degradation.

On the contrary, the buffering effect was not true at lower MCP or MBG weight ratio (< 10 wt%) as the amount was too low to take effect. The degradation profile of lower inorganic content/PLGA films was similar to the control. For this type of degradation, rapid increase of mass loss and buffer uptake was noticed and this might result in a collapse of the polymer matrix with time. However, the molecular weight change studied provided information that the rate of degradation was dependent on the amount of inorganic content incorporated. With higher weight ratio of inorganic content added, the degradation was retarded.

Another interesting finding was that comparing 10MCP/PLGA and 10MBG/PLGA films, both the buffer absorption and mass loss of the latter were higher. The buffer uptake could be attributed to the presence of Si-OH groups of MBG [185] which resulted in greater hydrophilicity than MCP. The mass loss of MCP/PLGA within the 56 days of *in vitro* degradation was very low (16 %) compared to PLGA/MBG (52 %). Hence, it was speculated that the leaching of MCP was lower than MBG. Therefore, the buffering effect of MCP was greater than MBG in the polymer matrix, resulting in a lower formation and dissolution of oligomers and monomers.

7.2 Protein release from MCP or MBG/PLGA film

Through the *in vitro* degradation studies, it was found that higher content of MCP and MBG in PLGA film helped to neutralize the pH environment of the polymer matrix to prevent burst release of the oligomers. Therefore, for the study on the protein release from the composite film, 10 wt% of protein loaded mesostructured materials would be incorporated into PLGA solution for film fabrication. The control of this study will be the addition of 10 wt% of protein LSZ or BSA into the polymer matrix. The protein release experiments were carried out over a period of 84 days incubated at pH 7.4 PBS.

7.2.1 UV-Vis assessment

The *in vitro* experiments examining the release of the protein BSA from the composite films are presented in Fig. 7.11a. BSA loaded films showed a four phase release profile – a short (1 day) initial release (inset), then a slow release (up to day 14), followed by a substantial release, before a linear release was observed after 35 days. The BSA loaded PLGA/MCP films presented a multi phase release profile, where a short (1 day) initial release, followed by a slow increase (up to day 14), then a substantial release (up to day 24), next a sustained release (up to day 56), and lastly a linear release was observed. Likewise, for BSA loaded PLGA/MBG films, a shorter lag phase (inset) was observed (up to day 3), followed by a substantial release (up to day 7), then a sustained release, prior to a linear increased release was noticed after 49 days of incubation. The total amount of BSA being released after 84 days of incubation was 9.3 µg/mg, 7.3 µg/mg and 8.4 µg/mg for PLGA-BSA, PLGA-MCP-BSA and PLGA-BSA-MBG, respectively.
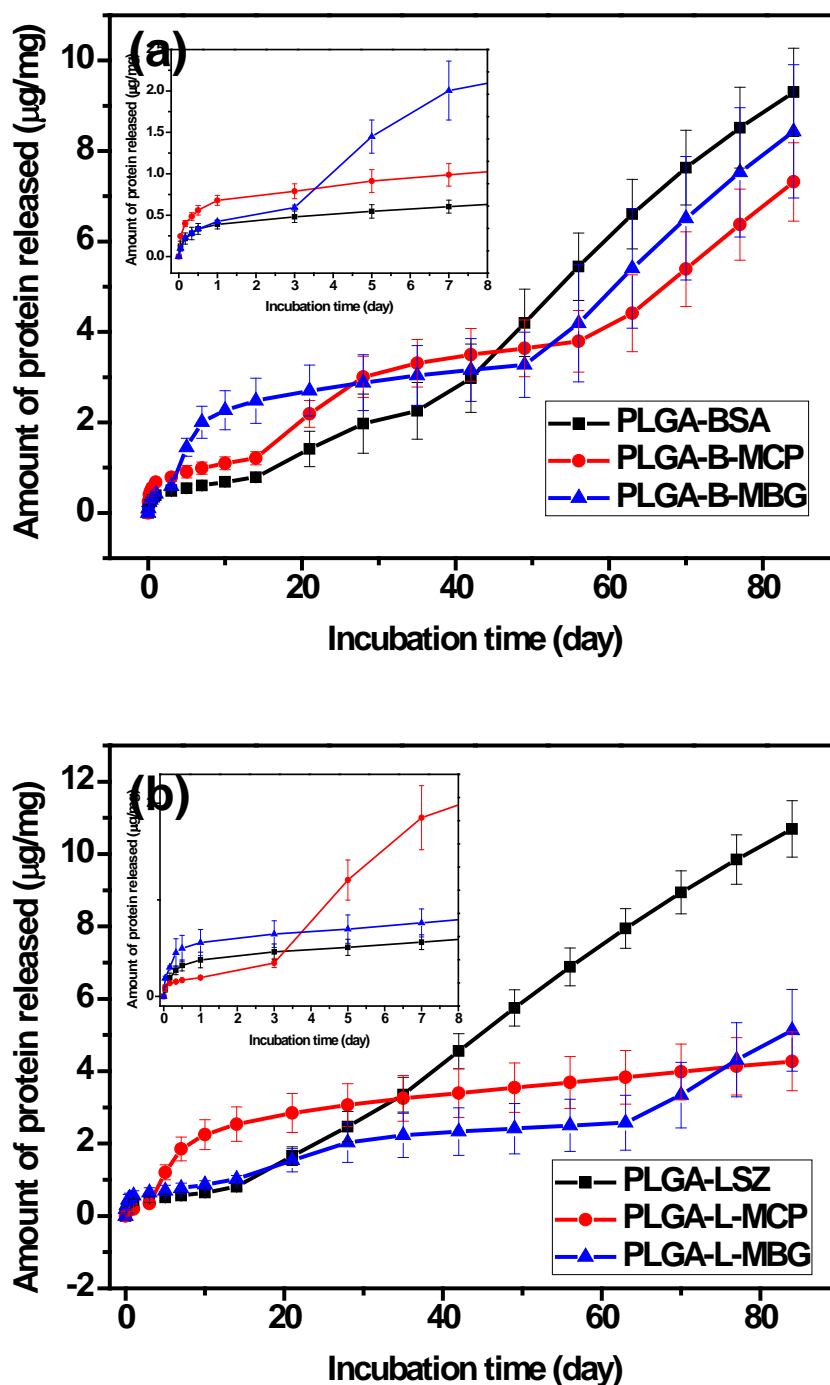
Figure 7.11 Cumulative amount of (a) BSA & (b) LSZ released from PLGA-CP, PLGA-MCP and PLGA-MBG films with the inset of the release profile for the first 7 days.

Fig.7.11b plots the amount of LSZ released from the PLGA and composite films. The release

of the PLGA-LSZ was observed to be similar to that of PLGA-BSA, where an initial short

release (1 day), followed by a slow release (up to day 14), then a substantial release (up to day 35) and lastly a linear release. While for the LSZ loaded PLGA/MCP film, a three phase (triphasic) release profile was shown as well. However, the release pattern was totally different from PLGA-BSA. A substantial release was observed after a 3 day initial release, and then from day 7 onwards, a sustained release of LSZ was presented. For PLGA-LSZ-MBG, the protein release was initiated by a slow release (up to day 14), followed by a small increase in the release (up to day 21), then a sustained release, before an increasing linear release was observed after 63 days of incubation. The total amount of LSZ being released after 84 days of incubation was 10.7 µg/mg, 4.3 µg/mg and 5.1 µg/mg for PLGA-LSZ, PLGA-LSZ-MCP and PLGA-LSZ-MBG, respectively.

It had been reported that diffusion took place when the release of drug was faster than matrix erosion [16, 186]. Therefore, it was believed that the slow substantial release of BSA from the pure PLGA film before 35 days was attributed to the diffusion of BSA through the polymer matrix and the result fitted well ($R^2 > 0.99$) with the Higuchi's model [122] as shown in Table 7.1. This phenomenon corresponded to the increase of buffer absorption and stable mass loss (Fig. 7.1 and Fig. 7.2) at this stage of incubation. Next a final release was observed as the PLGA exhibited substantial mass loss (day 35 onwards). The last time phase of release pattern was calculated as shown in Table 7.1, the results was fitted well into two models: diffusion (Higuchi's) and zero-order release. Therefore, it was believed that when the buffer uptake and mass loss of the PLGA matrix increased rapidly, the BSA release was a balance between diffusion controlled and zero-order release mechanism. Accordingly, the LSZ release from the pure PLGA film followed a similar explanation, but the last phase of linear release was dominated by diffusion.

Table 7.1 Value of R^2 (correlation coefficient) from the release data of different PLGA films at different time phase for Higuchi and zero-order models of protein release mechanism.

	BSA	B-MCP	B-MBG	LSZ	L-MCP	L-MBG
	PLGA matrix					
Time phase 1	3-14	3-14	7-35	3-14	3-10	1-14
	Higuchi model					
R^2	0.9955	0.9981	0.9919	0.9553	0.9701	0.9601
Time phase 2	-	28-56	-	-	-	28-63
	Higuchi model					
R^2	-	0.9885	-	-	-	0.9797
Time phase 3	35-84	63-84	49-84	21-84	10-84	63-84
	Higuchi model					
R^2	0.995	0.998	0.9938	0.99	0.9961	0.9969
	Zero-order model					
R^2	0.9455	0.9938	0.9785	0.8533	0.8558	0.9881

For BSA released from PLGA/MCP film, the initial low release of BSA could be dominated by the diffusion of some BSA molecules found on the surface as well as inside the polymer matrix during sample preparation. At the same time, the presence of MCP increased the bulk hydrophilicity of the whole polymer system and hence the desorption of BSA from MCP took place. The BSA molecules from the MCP diffused rapidly through the polymer matrix with increasing buffer absorption especially in the time frame between day 14 to day 56 of incubation. After 56 days of incubation, an increasing rate of linear release occurred where a rapid mass loss was shown. Again, the linear increase of BSA release was dominated by diffusion and zero-order kinetics. This pattern can be used to explain the release pattern of PLGA-BSA-MBG as well. The difference was that the diffusion of BSA molecules from

MBG penetrating the PLGA matrix happened at an earlier time point (day 3). This was because the adsorption capacity of BSA on MCP (190 µg/mg) was higher than that on MBG (21 µg/mg) by keeping the amount of protein loaded samples (i.e. BSA-MCP) constant. A higher loading of protein decreased the initial release rate [107, 187] because the desorption process was longer and hence the diffusion of protein into the matrix would be delayed.

For the LSZ loaded PLGA/MCP film, a different pattern of release was observed. Similarly, a small amount of the LSZ molecules adsorbed on the surface of PLGA was released for the early 3 days. Then diffusion of LSZ molecules released from the MCP took place throughout the process. Comparing to the release profile of BSA loaded PLGA/MCP film, the amount of LSZ loaded in MCP was relatively low (15 µg/mg). Hence the MCP content inside the PLGA here was relatively higher than BSA-MCP in PLGA matrix. In this case, the slow increase of mass loss without burst of 10MCP/PLGA (Fig. 7.2) was related. Hence, the degradation was retarded due to the pH buffering function of MCP [182, 184] in the PLGA system.

Nevertheless, the release pattern of LSZ loaded PLGA/MBG film was similar to PLGA-BSA-MCP film. A small lag phase took place in the initial stage comparing to the PLGA-BSA-MBG of relatively lower protein loaded. The second diffusion time phase for PLGA-LSZ-MBG was higher than PLGA-BSA-MBG (Table 7.1) and the final increase rate of release was started at a delay of 14 days from the onset of rapid mass loss. This could be attributed to the strong attractive force between LSZ and MBG (Table 6.3) and hence lengthen the diffusion process. Again, the final time phase of release profile for PLGA-LSZ-MBG was governed by diffusion and zero-order release mechanism.

7.2.2 Protein stability

To structure of the released LSZ and BSA from the composite film were analyzed by using circular dichroism (CD) over the wavelength 190 - 260 nm. Fig. 7.12 plots the far-UV CD spectra of the protein (a) BSA and (b) LSZ released from PLGA (control), PLGA/MCP and PLGA/MBG materials. For BSA released from PLGA/MCP, a broad negative ellipticity centered at 215 nm was noticed. While for all the other tested samples including the control, two similar minima were presented at 216 nm and 235 nm. All the spectra shown are unsmoothed which might be due to the low concentration of protein being released.

The weak minimum at 235 nm was due to an aromatic contribution [188, 189]. The low negative ellipticity of 216 nm was the characteristic of β-sheet conformation [190, 191]. It was observed that compared to the native spectrum of LSZ [191] and BSA [181], the peak minima might be shifted: a conformational switch from α-helix to β-sheet was induced. In other words, the native structure of the protein might be affected after being released from films. Since the experiments discussed in earlier chapter showed that the protein released from mesostructured powders retained their native α-helical structure, the structural change of the protein studied here might be originated from the solvent casting preparation process. The use of this technique exposed the protein adsorbed on the mesostructured materials to organic solvent chloroform during preparation.
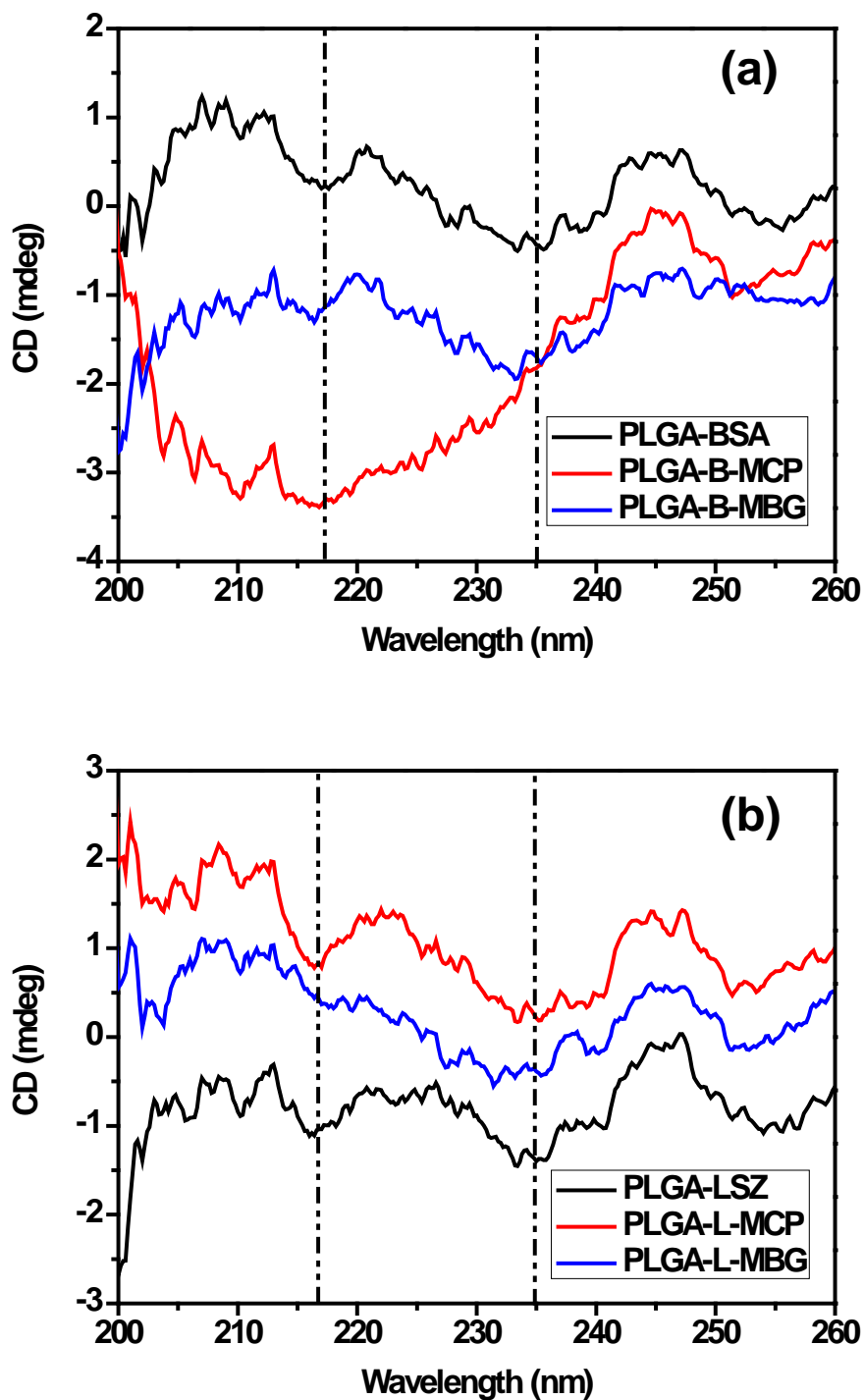
Figure 7.12 CD spectra of (a) Bovine serum albumin (BSA) and (b) Lysozyme (LSZ) after being released from the PLGA (control), PLGA/MCP and PLGA/MBG.

7.2.3 Summary

The protein release behavior and structure stability of PLGA/MCP and PLGA/MBG was examined using UV-Vis spectrophotometer and Circular Dichroism (CD) spectropolarimeter, respectively. The release was carried out over a period of 84 days (12 weeks). The LSZ molecules in PLGA film released through 3 stages of diffusion throughout the whole process. The release was in good pace with the degradation of PLGA film. When a rapid buffer absorption and mass loss was observed in the film, the rate of diffusion increased. On the other hand, the release of BSA from PLGA film adopted a similar release pattern. However, the release mechanism at the last stage of study involved diffusion as well as zero-order release.

In PLGA/MCP film, the initial low release was caused by the diffusion of some BSA molecules outside the MCP into polymer matrix. This phenomenon was observed in LSZ molecules of the same composite film as well. The presence of MCP raised the hydrophilicity inside the polymer matrix and therefore the diffusion of BSA molecules released from the MCP was initiated. Similarly, relating the degradation to the release process, a rapid increase in the buffer absorption resulted in a faster diffusion and zero-order release kinetics (both $R^2 >$ 0.99) in the last stage of release study. For the release of LSZ molecules, the diffusion started earlier than that of BSA molecules due to the lower loading of protein. The diffusion release was dominated throughout the process due to the buffering function of MCP. The slow increase of mass loss was in good agreement with the release profile. It was foreseen that another increased rate of release would occur at a longer time period when the MCP had leached to an extent of losing its buffering function.

For PLGA/MBG film, both the BSA as well as LSZ release exhibited a diffusion release mechanism. Similar to the principle of initial amount of protein loaded, the higher adsorption of LSZ into MBG had a lag phase of diffusion. The final time phase of the release profile for both the protein molecules from PLGA/MBG was governed by diffusion and zero-order release mechanism.

With the incorporation of MCP or MBG, the release profile was modified as compared to the pure PLGA film. The release system exhibited several phases of release favoring the delivery system which acquired time phase release. The initial release rate could be controlled by the amount of protein adsorbed on the inorganic materials. Besides that, higher content of inorganic samples could lengthen the mid time phase diffusion process because the inorganic samples could neutralize the pH environment of the matrix and prevent rapid mass loss and buffer absorption to take place.

In addition, the structure of the proteins was investigated to ascertain the bioactivity of the protein was preserved after released from PLGA film. A peak shift of the negative ellipticity (θ) from 208 nm to 216 nm was observed. This reflected a switch from α-helix to β-sheet conformation was induced. Hence, the bioactivity of protein BSA and LSZ released from PLGA film was affected. A possibility of this change was due to the solvent casting preparation process. The use of this technique exposed the protein adsorbed on the mesostructured materials to organic solvent chloroform during preparation.

CHAPTER 8

8 CONCLUSION AND RECOMMENDATION FOR FUTURE WORK

8.1 Conclusion

The effectiveness of mesostructured bioceramics in loading and preservation of protein bioactivity were studied in this work. By optimizing certain key synthesis parameters, it was found that high BET surface area bioceramics of MCP and MBG can be obtained. Proteins were subsequently loaded and it was found that the protein loading efficiency of the high surface area MCP and MBG was mainly affected by surface area, electrostatic interaction and conformational stability of protein. The initial *in vitro* protein release rate of the inorganic samples was governed by the amount of protein being loaded. Besides that, the secondary structure of both the proteins was preserved after release. Lastly protein-loaded MCP and MBG were incorporated into PLGA films to study how proteins will be released from these films. It was found that the presence of MCP and MBG affected the degradation rate of PLGA polymer films by increasing buffer absorption and mass loss, but reducing rate of molecular weight decrease. Higher amount of MCP and MBG could neutralize the pH environment of the matrix and prevent abrupt mass loss and buffer absorption to take place. Subsequently, protein release from PLGA/mesoporous materials film was studied, and it was found that the composite system exhibited time dependent release and was in good track with the *in vitro* degradation of PLGA composite film studied. The bioactivity of protein released from MCP and MBG films were affected, this was possibly attributed to the use of chloroform in casting of the PLGA films.

8.2 Future work

8.2.1 Protein selection in adsorption system

The protein adsorption using mesostructured calcium phosphates (MCP) has been studied and analyzed through several characterization techniques. In terms of protein selection, it is of our interest to understand that the hypothesis of mesostructured materials give rise to higher protein loading efficiency is valid with varying protein parameters. For instance, Lysozyme (MW ≈ 14.6 kDa, pI = 11.1) [86, 95], Myoglobin (MW = 17.8 kDa, pI = 7.0) [86] and α-Lactoalbumin (MW ≈ 14.4 kDa, pI = 4.1-4.8) [89] of similar molecular weight but different surface charge in physiological condition (pH 7.4) can be studied on MBG and MCP, respectively. The outcome would further enhance the effect of surface charge on the study of mesostructured materials in protein loading.

In addition, BSA (MW = 67.2 kDa, pI = 4.7) [86, 95], β-Casein (MW = 24.4 kDa, pI = 4.6) and Invertase (MW = 270 kDa, pI = 4.6) [89] can be selected as the protein candidates of similar surface charge but different molecular weight in protein loading. The influence of the molecular weight of protein could then be studied in-depth in the protein adsorption on mesostructured samples.

8.2.2 Film fabrication technique

In the last phase of the study, the proteins encountered conformational change after being released from the PLGA film which might be caused by the chloroform in the film preparation process. From the outcome, we realized that the mesostructured materials synthesized was able to adsorb and release from the powder samples in PBS however failed to protect the protein molecules in the harsh environment before release from PLGA film. Hence, other alternatives of film fabrication such as microemulsion [192, 193] can be proposed.

Besides that, another possibility of the result might be due to the pore size of the mesostructured materials and the protein sizes were different. The host material might have left with spaces for the penetration of chloroform into it if the protein sizes were either too small or too big to adsorb on. Hence while finding a suitable technique for the film fabrication; the selection of proteins is critical as well.

REFERENCES

[1] Mishra M, Kumar H, Tripathi K. Diabetic delayed wound healing and the role of silver nanoparticles. Digest Journal of Nanomaterials and Biostructures 2008;3:49-54.

[2] Zhang SF, Uludag H. Nanoparticulate Systems for Growth Factor Delivery. Pharmaceutical Research 2009;26:1561-80.

[3] Ong HT, Loo JSC, Boey FYC, Russell SJ, Ma J, Peng KW. Exploiting the high-affinity phosphonate-hydroxyapatite nanoparticle interaction for delivery of radiation and drugs. J Nanopart Res 2008;10:141-50.

[4] Sengupta S, Eavarone D, Capila I, Zhao G, Watson N, Kiziltepe T, et al. Temporal targeting of tumour cells and neovasculature with a nanoscale delivery system. Nature 2005;436:568-72.

[5] Fournier E, Passirani C, Montero-Menei CN, Benoit JP. Biocompatibility of implantable synthetic polymeric drug carriers: focus on brain biocompatibility. Biomaterials 2003;24:3311-31.

[6] Champion JA, Katare YK, Mitragotri S. Particle shape: A new design parameter for micro- and nanoscale drug delivery carriers. Journal of Controlled Release 2007;121:3-9.

[7] Panyam J, Dali MM, Sahoo SK, Ma W, Chakravarthi SS, Amidon GL, et al. Polymer degradation and in vitro release of a model protein from poly(,-lactide-co-glycolide) nano- and microparticles. Journal of Controlled Release 2003;92:173-87.

[8] Torchilin VP. Block copolymer micelles as a solution for drug delivery problems. Expert Opin Ther Patents 2005;15:63-75.

[9] Sutton D, Nasongkla N, Blanco E, Gao JM. Functionalized micellar systems for cancer targeted drug delivery. Pharmaceutical Research 2007;24:1029-46.

[10] Meyer J, Whitcomb L, Collins D. Efficient Encapsulation of Proteins Within Liposomes for Slow-release in-vivo. Biochemical and Biophysical Research Communications 1994;199:433-8.

[11] Murakami T, Tsuchida K. Recent advances in inorganic nanoparticle-based drug delivery systems. Mini-Rev Med Chem 2008;8:175-83.

[12] Hu L, Mao ZW, Gao CY. Colloidal particles for cellular uptake and delivery. Journal of Materials Chemistry 2009;19:3108-15.

[13] Uskokovic V, Uskokovic DP. Nanosized hydroxyapatite and other calcium phosphates: Chemistry of formation and application as drug and gene delivery agents. Journal of Biomedical Materials Research Part B-Applied Biomaterials 2011;96B:152-91.

[14] Xu ZP, Zeng QH, Lu GQ, Yu AB. Inorganic nanoparticles as carriers for efficient cellular delivery. Chem Eng Sci 2006;61:1027-40.

[15] Cortial G, Siutkowski M, Goettmann F, Moores A, Boissière C, Grosso D, et al. Metallic Nanoparticles Hosted in Mesoporous Oxide Thin Films for Catalytic Applications. Small 2006;2:1042-5.

[16] Soppimath KS, Aminabhavi TM, Kulkarni AR, Rudzinski WE. Biodegradable polymeric nanoparticles as drug delivery devices. Journal of Controlled Release 2001;70:1-20.

[17] Vallet-Regí M, Balas F, Arcos D. Mesoporous Materials for Drug Delivery. Angewandte Chemie International Edition 2007;46:7548-58.

[18] Wang S. Ordered mesoporous materials for drug delivery. Microporous and Mesoporous Materials 2009;117:1-9.

[19] Vallet-Regí M, Ramila A, del Real RP, Perez-Pariente J. A New Property of MCM-41: Drug Delivery System. Chemistry of Materials 2001;13:308-11.

[20] Kanatzidis MG. Beyond silica: Nonoxidic mesostructured materials. Adv Mater 2007;19:1165-81.

[21] Vallet-Regí M. Ordered Mesoporous Materials in the Context of Drug Delivery Systems and Bone Tissue Engineering. Chemistry - A European Journal 2006;12:5934-43.

[22] Izquierdo-Barba I, Ruiz-González L, Doadrio JC, González-Calbet JM, Vallet-Regí M. Tissue regeneration: A new property of mesoporous materials. Solid State Sciences 2005;7:983-9.

[23] Wang HL, Zhai LF, Li YH, Shi TJ. Preparation of irregular mesoporous hydroxyapatite. Mater Res Bull 2008;43:1607-14.

[24] Prélot B, Zemb T. Calcium phosphate precipitation in catanionic templates. Materials Science and Engineering C 2005;25:553-9.

[25] Yao J, Tjandra W, Chen YZ, Tam KC, Ma J, Soh B. Hydroxyapatite nanostructure material derived using cationic surfactant as a template. Journal of Materials Chemistry 2003;13:3053-7.

[26] Zhao YF, Ma J. Triblock co-polymer templating synthesis of mesostructured hydroxyapatite. Microporous and Mesoporous Materials 2005;87:110-7.

[27] Wan de Weert M, Hennink WE, Jiskoot W. Protein Instability in Poly(Lactic-co-Glycolic Acid) Microparticles. Pharmaceutical Research 2000;17:1159-67.

[28] Tabata Y, Takebayashi Y, Ueda T, Ikada Y. A formulation method using D, L-lactic acid oligomer for protein release with reduced initial burst. Journal of Controlled Release 1993;23:55-63.

[29] Tabata Y, Yamamoto M, Ikada Y. Biodegradable hydrogels for bone regeneration through growth factor release. Pure and Applied Chemistry 1998;70:1277-82.

[30] Soler-illia GJD, Sanchez C, Lebeau B, Patarin J. Chemical strategies to design textured materials: From microporous and mesoporous oxides to nanonetworks and hierarchical structures. Chemical Reviews 2002;102:4093-138.

[31] Kresge CT, Leonowicz ME, Roth WJ, Vartuli JC, Beck JS. Ordered mesoporous molecular sieves synthesized by a liquid-crystal template mechanism. Nature 1992;359:710-2.

[32] Vallet-Regí M, Colilla M, Izquierdo-Barba I. Bioactive Mesoporous Silicas as Controlled Delivery Systems: Application in Bone Tissue Regeneration. J Biomed Nanotechnol 2008;4:1-15.

[33] Yiu HHP, Wright PA, Botting NP. Enzyme immobilisation using SBA-15 mesoporous molecular sieves with functionalised surfaces. Journal of Molecular Catalysis B: Enzymatic 2001;15:81-92.

[34] Deere J, Magner E, Wall JG, Hodnett BK. Mechanistic and Structural Features of Protein Adsorption onto Mesoporous Silicates. The Journal of Physical Chemistry B 2002;106:7340-7.

[35] Balas F, Manzano M, Colilla M, Vallet-Regí M. L-Trp adsorption into silica mesoporous materials to promote bone formation. Acta Biomaterialia 2008;4:514-22.

[36] Vinu A, Murugesan V, Tangermann O, Hartmann M. Adsorption of Cytochrome c on Mesoporous Molecular Sieves: Influence of pH, Pore Diameter, and Aluminum Incorporation. Chemistry of Materials 2004;16:3056-65.

[37] Katiyar A, Ji L, Smirniotis PG, Pinto NG. Adsorption of Bovine Serum Albumin and lysozyme on siliceous MCM-41. Microporous and Mesoporous Materials 2005;80:311-20.

[38] Salinas AJ, Vallet-Regí M. Evolution of Ceramics with Medical Applications. Zeitschrift für anorganische und allgemeine Chemie 2007;633:1762-73.

[39] Vallet-Regi M. Revisiting ceramics for medical applications. Dalton Transactions 2006:5211-20.

[40] El-Ghannam A. Bone reconstruction: from bioceramics to tissue engineering. Expert Review of Medical Devices 2005;2:87-101.

[41] Arcos D, Izquierdo-Barba I, Vallet-Regí M. Promising trends of bioceramics in the biomaterials field. Journal of Materials Science: Materials in Medicine 2009;20:447-55.

[42] Hench LL, Polak JM. Third-Generation Biomedical Materials. Science 2002;295:1014-7.

[43] Hench LL, Splinter RJ, Allen WC, Greenlee TK. Bonding mechanisms at the interface of ceramic prosthetic materials. J Biomed Mater Res 1971;5:117-41.

[44] Hench LL. Bioceramics: From Concept to Clinic. Journal of the American Ceramic Society 1991;74:1487-510.

[45] Best SM, Porter AE, Thian ES, Huang J. Bioceramics: Past, present and for the future. Journal of the European Ceramic Society 2008;28:1319-27.

[46] Vallet-Regi M. Ceramics for medical applications. Journal of the Chemical Society, Dalton Transactions 2001:97-108.

[47] Mano JF, Sousa RA, Boesel LF, Neves NM, Reis RL. Bloinert, biodegradable and injectable polymeric matrix composites for hard tissue replacement: state of the art and recent developments. Composites Science and Technology 2004;64:789-817.

[48] Mikos AG, Herring SW, Ochareon P, Elisseeff J, Lu HH, Kandel R, et al. Engineering complex tissues. Tissue Engineering 2006;12:3307-39.

[49] Yan XX, Yu CZ, Zhou XF, Tang JW, Zhao DY. Highly ordered mesoporous bioactive glasses with superior in vitro bone-forming bioactivities. Angew Chem-Int Edit 2004;43:5980-4.

[50] Yan XX, Deng HX, Huang XH, Lu GQ, Qiao SZ, Zhao DY, et al. Mesoporous bioactive glasses. I. Synthesis and structural characterization. J Non-Cryst Solids 2005;351:3209-17.

[51] Yun H-s, Kim S-e, Hyeon Y-t. Highly ordered mesoporous bioactive glasses with Im3m symmetry. Materials Letters 2007;61:4569-72.

[52] Zhao LZ, Yan XX, Zhou XF, Zhou L, Wang HN, Tang HW, et al. Mesoporous bioactive glasses for controlled drug release. Microporous and Mesoporous Materials 2008;109:210-5.

[53] Xia W, Chang J. Well-ordered mesoporous bioactive glasses (MBG): A promising bioactive drug delivery system. Journal of Controlled Release 2006;110:522-30.

[54] Xia W, Chang J. Preparation, in vitro bioactivity and drug release property of well-ordered mesoporous 58S bioactive glass. J Non-Cryst Solids 2008;354:1338-41.

[55] Vallet-Regí M, González-Calbet JM. Calcium phosphates as substitution of bone tissues. Progress in Solid State Chemistry 2004;32:1-31.

[56] Hutmacher DW, Schantz JT, Lam CXF, Tan KC, Lim TC. State of the art and future directions of scaffold-based bone engineering from a biomaterials perspective. Journal of Tissue Engineering and Regenerative Medicine 2007;1:245-60.

[57] Habraken W, Wolke JGC, Jansen JA. Ceramic composites as matrices and scaffolds for drug delivery in tissue engineering. Advanced Drug Delivery Reviews 2007;59:234-48.

[58] Dorozhkin SV, Epple M. Biological and Medical Significance of Calcium Phosphates. Angewandte Chemie International Edition 2002;41:3130-46.

[59] Buranapanitkit B, Srinilta V, Ingviga N, Oungbho K, Geater A, Ovatlarnporn C. The Efficacy of a Hydroxyapatite Composite as a Biodegradable Antibiotic Delivery System. Clinical Orthopaedics and Related Research 2004;424:244-52 10.1097/01.blo.0000130268.27024.c1.

[60] Hamanishi C, Kitamoto K, Tanaka S, Otsuka M, Doi Y, Kitahashi T. A self-setting TTCP-DCPD apatite cement for release of vancomycin. J Biomed Mater Res 1996;33:139-43.

[61] Liu T-Y, Chen S-Y, Liu D-M, Liou S-C. On the study of BSA-loaded calcium-deficient hydroxyapatite nano-carriers for controlled drug delivery. Journal of Controlled Release 2005;107:112-21.

[62] Itokazu M, Sugiyama T, Ohno T, Wada E, Katagiri Y. Development of porous apatite ceramic for local delivery of chemotherapeutic agents. J Biomed Mater Res 1998;39:536-8.

[63] Zahouily M, Abrouki Y, Bahlaouan B, Rayadh A, Sebti S. Hydroxyapatite: new efficient catalyst for the Michael addition. Catalysis Communications 2003;4:521-4.

[64] Huo Q, Margolese DI, Ciesla U, Feng P, Gier TE, Sieger P, et al. Generalized synthesis of periodic surfactant/inorganic composite materials. Nature 1994;368:317-21.

[65] Soler-Illia GJAA, Crepaldi EL, Grosso D, Sanchez C. Block copolymer-templated mesoporous oxides. Curr Opin Colloid Interface Sci 2003;8:109-26.

[66] Schüth F. Non-siliceous Mesostructured and Mesoporous Materials. Chemistry of Materials 2001;13:3184-95.

[67] Coelho J, Moreira J, Almeida A, Monteiro F. Synthesis and characterization of HAp nanorods from a cationic surfactant template method. Journal of Materials Science: Materials in Medicine 2010;21:2543-9.

[68] Schmidt SM, McDonald J, Pineda ET, Verwilst AM, Chen YM, Josephs R, et al. Surfactant based assembly of mesoporous patterned calcium phosphate micron-sized rods. Microporous and Mesoporous Materials 2006;94:330-8.

[69] Zhang S, Wang Y, Wei K, Liu X, Chen J, Wang X. Template-assisted synthesis of lamellar mesostructured hydroxyapatites. Materials Letters 2007;61:1341-5.

[70] Mohanty P, Lee J, Jebrell Glover K, Landskron K. Discoid Bicelles as Efficient Templates for Pillared Lamellar Periodic Mesoporous Silicas at pH 7 and Ultrafast Reaction Times. Nanoscale Research Letters 2010:1-5.

[71] Guo Y, Zhou Y, Jia D, Tang H. Fabrication and characterization of hydroxycarbonate apatite with mesoporous structure. Microporous and Mesoporous Materials 2009;118:480-8.

[72] Ikawa N, Oumi Y, Kimura T, Ikeda T, Sano T. Synthesis of lamellar mesostructured calcium phosphates using n-alkylamines as structure-directing agents in alcohol/water mixed solvent systems. J Mater Sci 2008;43:4198-207.

[73] Shi G, Cai Q, Wang C, Lu N, Wang S, Bei J. Fabrication and biocompatibility of cell scaffolds of poly(L-lactic acid) and poly(L-lactic-co-glycolic acid). Polymers for Advanced Technologies 2002;13:227-32.

[74] Cohen S, Yoshioka T, Lucarelli M, Hwang LH, Langer R. Controlled Delivery Systems for Proteins Based on Poly(Lactic/Glycolic Acid) Microspheres. Pharmaceutical Research 1991;8:713-20.

[75] Mano JF, Sousa RA, Boesel LF, Neves NM, Reis RL. Bioinert, biodegradable and injectable polymeric matrix composites for hard tissue replacement: state of the art and recent developments. Composites Science and Technology 2004;64:789-817.

[76] Bergsma EJ, Rozema FR, Bos RRM, Bruijn WCD. Foreign body reactions to resorbable poly(l-lactide) bone plates and screws used for the fixation of unstable zygomatic fractures. Journal of Oral and Maxillofacial Surgery 1993;51:666-70.

[77] Martin C, Winet H, Bao JY. Acidity near eroding polylactide-polyglycolide in vitro and in vivo in rabbit tibial bone chambers. Biomaterials 1996;17:2373-80.

[78] Agrawal CM, Athanasiou KA. Technique to control pH in vicinity of biodegrading PLA-PGA implants. J Biomed Mater Res 1997;38:105-14.

[79] Rezwan K, Chen QZ, Blaker JJ, Boccaccini AR. Biodegradable and bioactive porous polymer/inorganic composite scaffolds for bone tissue engineering. Biomaterials 2006;27:3413-31.

[80] Dunn AS, Campbell PG, Marra KG. The influence of polymer blend composition on the degradation of polymer/hydroxyapatite biomaterials. Journal of Materials Science: Materials in Medicine 2001;12:673-7.

[81] Boccaccini AR, Maquet V. Bioresorbable and bioactive polymer/Bioglass® composites with tailored pore structure for tissue engineering applications. Composites Science and Technology 2003;63:2417-29.

[82] Li X, Shi J, Dong X, Zhang L, Zeng H. A mesoporous bioactive glass/polycaprolactone composite scaffold and its bioactivity behavior. Journal of Biomedical Materials Research Part A 2008;84A:84-91.

[83] Xue JM, Shi M. PLGA/mesoporous silica hybrid structure for controlled drug release. Journal of Controlled Release 2004;98:209-17.

[84] Wu C, Ramaswamy Y, Zhu Y, Zheng R, Appleyard R, Howard A, et al. The effect of mesoporous bioactive glass on the physiochemical, biological and drug-release properties of poly(dl-lactide-co-glycolide) films. Biomaterials 2009;30:2199-208.

[85] Hartmann M. Ordered Mesoporous Materials for Bioadsorption and Biocatalysis. Chemistry of Materials 2005;17:4577-93.

[86] Kandori K, Mizumoto S, Toshima S, Fukusumi M, Morisada Y. Effects of Heat Treatment of Calcium Hydroxyapatite Particles on the Protein Adsorption Behavior. The Journal of Physical Chemistry B 2009;113:11016-22.

[87] Kandori K, Oda S, Fukusumi M, Morisada Y. Synthesis of positively charged calcium hydroxyapatite nano-crystals and their adsorption behavior of proteins. Colloids and Surfaces B: Biointerfaces 2009;73:140-5.

[88] Kandori K, Fudo A, Ishikawa T. Adsorption of myoglobin onto various synthetic hydroxyapatite particles. Physical Chemistry Chemical Physics 2000;2:2015-20.

[89] Imamura K, Shimomura M, Nagai S, Akamatsu M, Nakanishi K. Adsorption characteristics of various proteins to a titanium surface. Journal of Bioscience and Bioengineering 2008;106:273-8.

[90] Sugio S, Kashima A, Mochizuki S, Noda M, Kobayashi K. Crystal structure of human serum albumin at 2.5 Å resolution. Protein Engineering 1999;12:439-46.

[91] Carter DC, JX H. Structure of serum albumin. Advances in Protein Chemistry 1994;45:153-203.

[92] Figge J, Rossing T, Fencl V. The role of serum proteins in acid-base equilibria. The Journal of laboratory and clinical medicine 1991;117:453-67.

[93] Poole S, West SI, Fry JC. Effects of basic proteins on the denaturation and heat-gelation of acidic proteins. Food Hydrocolloids 1987;1:301-16.

[94] Rüegg M, Moor U, Blanc B. A calorimetric study of the thermal denaturation of whey proteins in simulated milk ultrafiltrate. Journal of Dairy Research 1977;44:509-20.

[95] Zhang X, Bai R, Tong YW. Selective adsorption behaviors of proteins on polypyrrole-based adsorbents. Separation and Purification Technology 2006;52:161-9.

[96] Katiyar A, Thiel SW, Guliants VV, Pinto NG. Investigation of the mechanism of protein adsorption on ordered mesoporous silica using flow microcalorimetry. Journal of Chromatography A 2010;1217:1583-8.

[97] Blake CCF, Koenig DF, Mair GA, North ACT, Phillips DC, Sarma VR. Structure of Hen Egg-White Lysozyme: A Three-dimensional Fourier Synthesis at 2 [angst] Resolution. Nature 1965;206:757-61.

[98] Kharakoz DP, Sarvazyan AP. Hydrational and intrinsic compressibilities of globular proteins. Biopolymers 1993;33:11-26.

[99] Kandori K, Oda S, Tsuyama S. Effects of Pyrophosphate Ions on Protein Adsorption onto Calcium Hydroxyapatite. The Journal of Physical Chemistry B 2008;112:2542-7.

[100] Hayashi K, Kugimiya M, Funatsu M. Heat Stability of Lysozyme-substrate Complex. Journal of Biochemistry 1968;64:93-7.

[101] Remmele RL, McMillan P, Bieber A. Raman-spectroscopic studies of then egg-white lysozyme at high temperatures and pressures. Journal of Protein Chemistry 1990;9:475-86.

[102] Norde W, Arai T, Shirahama H. Protein adsorption in model systems. Biofouling: The Journal of Bioadhesion and Biofilm Research 1991;4:37 - 51.

[103] Klibanov AM. Immobilized Enzymes and Cells as Practical Catalysts. Science 1983;219:722-7.

[104] Xue W, Bandyopadhyay A, Bose S. Mesoporous calcium silicate for controlled release of bovine serum albumin protein. Acta Biomaterialia 2009;5:1686-96.

[105] Vallet-Regi M, Balas F, Colilla M, Manzano M. Drug Confinement and Delivery in Ceramic Implants. Drug Metabolism Letters 2007;1:37-40.

[106] Katiyar A, Ji L, Smirniotis P, Pinto NG. Protein adsorption on the mesoporous molecular sieve silicate SBA-15: effects of pH and pore size. Journal of Chromatography A 2005;1069:119-26.

[107] Cai C, Bakowsky U, Rytting E, Schaper AK, Kissel T. Charged nanoparticles as protein delivery systems: A feasibility study using lysozyme as model protein. European Journal of Pharmaceutics and Biopharmaceutics 2008;69:31-42.

[108] Rezwan K, Meier LP, Gauckler LJ. Lysozyme and bovine serum albumin adsorption on uncoated silica and AlOOH-coated silica particles: the influence of positively and negatively charged oxide surface coatings. Biomaterials 2005;26:4351-7.

[109] Burns N, Holmberg K. Surface charge characterization and protein adsorption at biomaterials surfaces. In: Solans C, Infante M, García-Celma M, editors. Trends in Colloid and Interface Science X: Springer Berlin / Heidelberg; 1996. p. 271-5.

[110] Servagent-Noinville S, Revault M, Quiquampoix H, Baron MH. Conformational Changes of Bovine Serum Albumin Induced by Adsorption on Different Clay Surfaces: FTIR Analysis. Journal of Colloid and Interface Science 2000;221:273-83.

[111] Arai T, Norde W. The behavior of some model proteins at solid-liquid interfaces 1. Adsorption from single protein solutions. Colloids and Surfaces 1990;51:1-15.

[112] Norde W, Anusiem ACI. Adsorption, desorption and re-adsorption of proteins on solid surfaces. Colloids and Surfaces 1992;66:73-80.

[113] Belcourt A. Adsorption of human salivary proteins on synthetic hydroxyapatite. Archives of Oral Biology 1976;21:717-22.

[114] Luong LN, Hong SI, Patel RJ, Outslay ME, Kohn DH. Spatial control of protein within biomimetically nucleated mineral. Biomaterials 2006;27:1175-86.

[115] Kandori K, Fujiwara A, Mukai M, Yasukawa A, Ishikawa T. Evaluation of the adsorption affinity of proteins to calcium hydroxyapatites by desorption and pre-adsorption methods. Colloids and Surfaces B: Biointerfaces 1998;11:313-20.

[116] Vegt W, Mei HC, Busscher HJ, Norde W. pH dependence of the kinetics of interfacial tension changes during protein adsorption from sessile droplets on FEP-Teflon. Colloid & Polymer Science 1996;274:27-33.

[117] Korsmeyer RW, Gurny R, Doelker E, Buri P, Peppas NA. Mechanisms of solute release from porous hydrophilic polymers. International Journal of Pharmaceutics 1983;15:25-35.

[118] Gunder W, Lippold BH, Lippold BC. Release of drugs from ethyl cellulose microcapsules (diffusion pellets) with pore formers and pore fusion. European Journal of Pharmaceutical Sciences 1995;3:203-14.

[119] Borodkin S, Tucker FE. Linear drug release from laminated hydroxypropyl cellulose-polyvinyl acetate films. Journal of Pharmaceutical Sciences 1975;64:1289-94.

[120] Niwa K, Takaya T, Morimoto T, Takada K. Preparation and evaluation of a time-controlled release capsule made of ethylcellulose for colon delivery of drugs. Journal of Drug Targeting 1995;3:83-9.

[121] Higuchi T. Rate of release of medicaments from ointment bases containing drugs in suspension. Journal of Pharmaceutical Sciences 1961;50:874-5.

[122] Higuchi T. Mechanism of sustained-action medication. Theoretical analysis of rate of release of solid drugs dispersed in solid matrices. Journal of Pharmaceutical Sciences 1963;52:1145-9.

[123] Avachat A, Kotwal V. Design and evaluation of matrix-based controlled release tablets of diclofenac sodium and chondroitin sulphate. AAPS PharmSciTech 2007;8:51-6.

[124] Varshosaz J, Tavakoli N, Kheirolahi F. Use of hydrophilic natural gums in formulation of sustained-release matrix tablets of tramadol hydrochloride. AAPS PharmSciTech 2006;7:E168-E74.

[125] Kim SW, Bae YH, Okano T. Hydrogels: Swelling, Drug Loading, and Release. Pharmaceutical Research 1992;9:283-90.

[126] Chien Y. Novel drug delivery stystems. 2nd ed.

[127] Brahmankar. Biopharmaceutics and pharmacokinetics. 5th ed.

[128] Mathiowitz E. Encyclopedia of controlled drug delivery. 1st ed.

[129] Wise D. Hand book of pharmaceutical controlled release technology. 1st ed.

[130] Sing KSW. Reporting physisorption data for gas/solid systems with special reference to the determination of surface area and porosity (Provisional). Pure and Applied Chemistry 1982;54:2201-18.

[131] Johnson JF, Porter RS. Gel permeation chromatography. Progress in Polymer Science 1970;2:201-56.

[132] Ng S, Guo J, Ma J, Loo SCJ. Synthesis of high surface area mesostructured calcium phosphate particles. Acta Biomaterialia 2010;6:3772-81.

[133] Mohsen-Nia M, Amiri H, Jazi B. Dielectric Constants of Water, Methanol, Ethanol, Butanol and Acetone: Measurement and Computational Study. Journal of Solution Chemistry 2010;39:701-8.

[134] Gregory AP, Clarke RN. Traceable measurements of the static permittivity of dielectric reference liquids over the temperature range 5–50 °C. Measurement Science and Technology 2005;16:1506.

[135] Weast RC. CRC Handbook of Chemistry and Physics. 47th ed.

[136] Jain NJ, Aswal VK, Goyal PS, Bahadur P. Micellar structure of an ethylene oxide propylene oxide block copolymer: A small-angle neutron scattering study. Journal of Physical Chemistry B 1998;102:8452-8.

[137] Kadam Y, Ganguly R, Kumbhakar M, Aswal VK, Hassan PA, Bahadur P. Time Dependent Sphere-to-Rod Growth of the Pluronic Micelles: Investigating the Role of Core and Corona Solvation in Determining the Micellar Growth Rate. The Journal of Physical Chemistry B 2009;113:16296-302.

[138] Salahi E, Moztarzadeh F. Composition of calcium phosphates precipitated from aqueous solutions at different pH values. Cfi-Ceramic Forum International 2001;78:E43-E6.

[139] Kalita SJ, Bhardwaj A, Bhatt HA. Nanocrystalline calcium phosphate ceramics in biomedical engineering. Materials Science and Engineering: C 2007;27:441-9.

[140] Loo SCJ, Siew YE, Ho S, Boey FYC, Ma J. Synthesis and hydrothermal treatment of nanostructured hydroxyapatite of controllable sizes. J Mater Sci-Mater Med 2008;19:1389-97.

[141] Al-Qasas NS, Rohani S. Synthesis of pure hydroxyapatite and the effect of synthesis conditions on its yield, crystallinity, morphology and mean particle size. Sep Sci Technol 2005;40:3187-224.

[142] Wei K, Wang YJ, Lai C, Ning CY, Wu DX, Wu G, et al. Synthesis and characterization of hydroxyapatite nanobelts and nanoparticles. Materials Letters 2005;59:220-5.

[143] Posner AS, Perloff A, Diorio AF. Refinement of the hydroxyapatite structure. Acta Crystallographica 1958;11:308-9.

[144] Mandel S, Tas AC. Brushite ($CaHPO_4 \cdot 2H_2O$) to octacalcium phosphate ($Ca_8(HPO_4)_2(PO_4)_4 \cdot 5H_2O$) transformation in DMEM solutions at 36.5 °C. Materials Science & Engineering C-Materials for Biological Applications 2010;30:245-54.

[145] Beevers C. The crystal structure of dicalcium phosphate dihydrate, CaHPO4.2H2O. Acta Crystallographica 1958;11:273-7.

[146] Rehman I, Bonfield W. Characterization of hydroxyapatite and carbonated apatite by photo acoustic FTIR spectroscopy. Journal of Materials Science: Materials in Medicine 1997;8:1-4.

[147] Eslami H, Solati-Hashjin M, Tahriri M. Synthesis and Characterization of Hydroxyapatite Nanocrystals via Chemical Precipitation Technique. Iranian Journal of Pharmaceutical Sciences 2008;4:127-34.

[148] Komath M, Varma HK. Development of a fully injectable calcium phosphate cement for orthopedic and dental applications. Bulletin of Materials Science 2003;26:415-22.

[149] Koutsopoulos S. Synthesis and characterization of hydroxyapatite crystals: A review study on the analytical methods. J Biomed Mater Res 2002;62:600-12.

[150] Joshi VS, Joshi MJ. FTIR spectroscopic, thermal and growth morphological studies of calcium hydrogen phosphate dihydrate crystals. Crystal Research and Technology 2003;38:817-21.

[151] Rodriguez-Lorenzo LM, Vallet-Regi M. Controlled Crystallization of Calcium Phosphate Apatites. Chemistry of Materials 2000;12:2460-5.

[152] Huang LF, Lu PS, Chiou LC, Chang IL, Shih CJ. Influence of Surfactant Concentration on Mesoporous Bioactive Glass Scaffolds with Superior in Vitro Bone-Forming Bioactivities. In: Lim CT, Goh JCH, editors. 13th International Conference on Biomedical Engineering: Springer Berlin Heidelberg; 2009. p. 1366-8.

[153] Su Y-l, Wang J, Liu H-z. FTIR Spectroscopic Investigation of Effects of Temperature and Concentration on PEO−PPO−PEO Block Copolymer Properties in Aqueous Solutions. Macromolecules 2002;35:6426-31.

[154] Lin Y, Alexandridis P. Temperature-Dependent Adsorption of Pluronic F127 Block Copolymers onto Carbon Black Particles Dispersed in Aqueous Media. The Journal of Physical Chemistry B 2002;106:10834-44.

[155] Alexandridis P, Holzwarth JF, Hatton TA. Micellization of Poly(ethylene oxide)-Poly(propylene oxide)-Poly(ethylene oxide) Triblock Copolymers in Aqueous Solutions: Thermodynamics of Copolymer Association. Macromolecules 1994;27:2414-25.

[156] González-Pérez A, Ruso JM. Temperature dependence of micellar sphere-to-rod transition using adiabatic compressibility. Colloids and Surfaces A: Physicochemical and Engineering Aspects 2010;356:84-8.

[157] Galarneau A, Cambon H, Di Renzo F, Fajula F. True microporosity and surface area of mesoporous SBA-15 silicas as a function of synthesis temperature. Langmuir 2001;17:8328-35.

[158] Jain NJ, Aswal VK, Goyal PS, Bahadur P. Salt induced micellization and micelle structures of' PEO/PPO/PEO block copolymers in aqueous solution. Colloids and Surfaces A: Physicochemical and Engineering Aspects 2000;173:85-94.

[159] Guo C, Liu HZ, Chen JY. A Fourier transform infrared study of the phase transition in aqueous solutions of Ethylene oxide–propylene oxide triblock copolymer. Colloid & Polymer Science 1999;277:376-81.

[160] El Hammari L, Merroun H, Coradin T, Cassaignon S, Laghzizil A, Saoiabia A. Mesoporous hydroxyapatites prepared in ethanol-water media: Structure and surface properties. Materials Chemistry and Physics 2007;104:448-53.

[161] Deng Y, Li XK, Li Q. Effect of Pore Size on the Growth of Hydroxyapatite from Mesoporous CaO-SiO2 Substrate. Industrial & Engineering Chemistry Research 2009;48:8829-36.

[162] Kothapalli C, Wei M, Vasiliev A, Shaw MT. Influence of temperature and concentration on the sintering behavior and mechanical properties of hydroxyapatite. Acta Materialia 2004;52:5655-63.

[163] Landi E, Tampieri A, Celotti G, Sprio S. Densification behaviour and mechanisms of synthetic hydroxyapatites. Journal of the European Ceramic Society 2000;20:2377-87.

[164] Pang YX, Bao X. Influence of temperature, ripening time and calcination on the morphology and crystallinity of hydroxyapatite nanoparticles. Journal of the European Ceramic Society 2003;23:1697-704.

[165] Bouyer E, Gitzhofer F, Boulos MI. Morphological study of hydroxyapatite nanocrystal suspension. Journal of Materials Science: Materials in Medicine 2000;11:523-31.

[166] Gibson IR, Ke S, Best SM, Bonfield W. Effect of powder characteristics on the sinterability of hydroxyapatite powders. Journal of Materials Science: Materials in Medicine 2001;12:163-71.

[167] Yan XX, Huang XH, Yu CZ, Deng HX, Wang Y, Zhang ZD, et al. The in-vitro bioactivity of mesoporous bioactive glasses. Biomaterials 2006;27:3396-403.

[168] Li R, Clark AE, Hench LL. Effect of structure and surface area on bioactive powders made by sol-gel process. In: Hench LL, West JK, editors. Chemical Processing of Advanced Materials. New York: Wiley; 1992. p. 627-33.

[169] Hung IM, Hung D-T, Fung K-Z, Hon M-H. Effect of calcination temperature on morphology of mesoporous YSZ. Journal of the European Ceramic Society 2006;26:2627-32.

[170] Pérez-Pariente J, Balas F, Román J, Salinas AJ, Vallet-Regí M. Influence of composition and surface characteristics on the in vitro bioactivity of $SiO_2-CaO-P_2O_5-MgO$ sol-gel glasses. J Biomed Mater Res 1999;47:170-5.

[171] Saravanapavan P, Hench LL. Mesoporous calcium silicate glasses. I. Synthesis. J Non-Cryst Solids 2003;318:1-13.

[172] Shih CJ, Chen HT, Huang LF, Lu PS, Chang HF, Chang IL. Synthesis and in vitro bioactivity of mesoporous bioactive glass scaffolds. Materials Science and Engineering: C 2010;30:657-63.

[173] Choi SH, Park TG. G-CSF loaded biodegradable PLGA nanoparticles prepared by a single oil-in-water emulsion method. International Journal of Pharmaceutics 2006;311:223-8.

[174] Qi C, Chen Y, Jing Q-Z, Wang X-G. Preparation and Characterization of Catalase-Loaded Solid Lipid Nanoparticles Protecting Enzyme against Proteolysis. International Journal of Molecular Sciences 2011;12:4282-93.

[175] Adams S, Higgins AM, Jones RAL. Surface-Mediated Folding and Misfolding of Proteins at Lipid/Water Interfaces. Langmuir 2002;18:4854-61.

[176] Abdelmoez W, Yoshida H. Mechanical and Thermal Properties of a Novel Protein-Based Plastic Synthesized Using Subcritical Water Technology. Macromolecules 2007;40:9371-7.

[177] Colilla M, Manzano M, Vallet-Regi M. Recent advances in ceramic implants as drug delivery systems for biomedical applications. International Journal of Nanomedicine 2008;3:403-14.

[178] Lu W, Park TG. Protein Release from Poly(lactic-co-glycolic acid) Microspheres: Protein Stability Problems. PDA Journal of Pharmaceutical Science and Technology 1995;49:13-9.

[179] Park TG, Lu W, Crotts G. Importance of in vitro experimental conditions on protein release kinetics, stability and polymer degradation in protein encapsulated poly (-lactic acid-co-glycolic acid) microspheres. Journal of Controlled Release 1995;33:211-22.

[180] Igartua M, Hernández RM, Esquisabel A, Gascón AR, Calvo MB, Pedraz JL. Stability of BSA encapsulated into PLGA microspheres using PAGE and capillary electrophoresis. International Journal of Pharmaceutics 1998;169:45-54.

[181] Norde W, Giacomelli CE. BSA structural changes during homomolecular exchange between the adsorbed and the dissolved states. Journal of Biotechnology 2000;79:259-68.

[182] Ara M, Watanabe M, Imai Y. Effect of blending calcium compounds on hydrolytic degradation of poly(-lactic acid-co-glycolic acid). Biomaterials 2002;23:2479-83.

[183] Loher S, Reboul V, Brunner TJ, Simonet M, Dora C, Neuenschwander P, et al. Improved degradation and bioactivity of amorphous aerosol derived tricalcium phosphate nanoparticles in poly(lactide-co-glycolide). Nanotechnology 2006;17:2054.

[184] Ehrenfried L, Patel M, Cameron R. The effect of tri-calcium phosphate (TCP) addition on the degradation of polylactide-co-glycolide (PLGA). Journal of Materials Science: Materials in Medicine 2008;19:459-66.

[185] Wagh PB, Ingale SV. Comparison of some physico-chemical properties of hydrophilic and hydrophobic silica aerogels. Ceramics International 2002;28:43-50.

[186] Niwa T, Takeuchi H, Hino T, Kunou N, Kawashima Y. Preparations of biodegradable nanospheres of water-soluble and insoluble drugs with D,L-lactide/glycolide copolymer by a novel spontaneous emulsification solvent diffusion method, and the drug release behavior. Journal of Controlled Release 1993;25:89-98.

[187] Hu F-Q, Ren G-F, Yuan H, Du Y-Z, Zeng S. Shell cross-linked stearic acid grafted chitosan oligosaccharide self-aggregated micelles for controlled release of paclitaxel. Colloids and Surfaces B: Biointerfaces 2006;50:97-103.

[188] Albinsson B, Norden B. Excited-state properties of the indole chromophore: electronic transition moment directions from linear dichroism measurements: effect of methyl and methoxy substituents. The Journal of Physical Chemistry 1992;96:6204-12.

[189] McLaughlin RW, De Stigter JK, Sikkink LA, Baden EM, Ramirez-Alvarado M. The effects of sodium sulfate, glycosaminoglycans, and Congo red on the structure, stability, and amyloid formation of an immunoglobulin light-chain protein. Protein Science 2006;15:1710-22.

[190] Sundd M, Kundu S, Jagannadham MV. Alcohol-Induced Conformational Transitions in Ervatamin C. An α-Helix to β-Sheet Switchover. Journal of Protein Chemistry 2000;19:169-76.

[191] Byrne N, Angell CA. Formation and dissolution of hen egg white lysozyme amyloid fibrils in protic ionic liquids. Chemical Communications 2009:1046-8.

[192] Bergström K, Holmberg K. Microemulsions as reaction media for immobilization of proteins to hydrophilized surfaces. Colloids and Surfaces 1992;63:273-80.

[193] Hammady T, Nadeau V, Hildgen P. Microemulsion and diafiltration approaches: An attempt to maximize the global yield of DNA-loaded nanospheres. European Journal of Pharmaceutics and Biopharmaceutics 2006;62:143-54.